Chapter 1. Optics and Quantum Electronics

Academic and Research Staff

Professor Hermann A. Haus, Professor Erich P. Ippen, Professor James G. Fujimoto, Professor Peter L. Hagelstein, Dr. Wolfgang Drexler, Dr. Franz X. Kärtner, Dr. Xingde Li, Dr. Brent E. Little

Visiting Scientists and Research Affiliates

Dr. Mark E. Brezinski,[1] Dr. Yijiang Chen, Dr. Katherine L. Hall, Dr. Jürgen Herrmann, Dr. Markus Joschko, Dr. Patrick Langlois, Dr. Moti Margalit, Dr. Masayuki Matsumoto, Dr. Victor P. Mikhailov,[2] Leo J. Missaggia,[3] Dr. Uwe Morgner, Dr. Joel Schuman,[4] Dr. Debra L. Stamper,[5] Dr. Günter Steinmeyer, Dr. James N. Walpole,[3] Christine A. Jesser, Juha-Pekka J.V. Laine, Thomas R. Schibli, Gaston E. Tudury

Graduate Students

Igor P. Bilinsky, Stephen A. Boppart, Seong-Ho Cho, Patrick C. Chou, Douglas R. Denison, John M. Fini, Ravi K. Ghanta, Boris Golubovic, Juliet T. Gopinath, Matthew E. Grein, Pei-Lin Hsiung, Leaf A. Jiang, David J. Jones, Mohammed J. Khan, Christina Manolatou, Parth Patwai, Costantinos Pitris, Rohit P. Prasankumar, Daniel J. Ripin, Guillermo J. Tearney, Erik R. Thoen, William S. Wong, Charles X. Yu

Undergraduate Students

Christopher Lin, Jessica Tan

Technical and Support Staff

Mary C. Aldridge, Donna L. Gale, Cynthia Y. Kopf

1.1 Ultrashort Pulse Kerr-Lens Modelocked Ti:Sapphire Laser Producing Sub-Two-Cycle Optical Pulses

Sponsor

U.S. Air Force - Office of Scientific Research
Grant F49620-98-1-0139

Project Staff

Dr. Franz X. Kärtner, Professor Hermann A. Haus, Professor Erich P. Ippen, Professor James G. Fujimoto, Dr. Uwe Morgner, Dr. Yijiang Chen, John M. Fini, Seong-Ho Cho

Currently, high-energy pulses as short as 4 to 5 fs at a center wavelength of 800 nm are generated by external compression at kHz and 1 MHz repetition rates, respectively.[6] These pulse widths correspond to less than two optical cycles. The shortest pulses generated at the higher repetition rate of 100 MHz have been 6.5 fs[7] and 7 fs.[8] For high-resolution opti-

1 Massachusetts General Hospital, Boston, Massachusetts.

2 Professor, International Laser Center, Polytechnical Academy, Minsk, Belarus.

3 MIT Lincoln Laboratories, Lexington, Massachusetts.

4 New England Eye Center and Tufts University School of Medicine, Boston, Massachusetts.

5 Department of Biology, Kings College, Wilkes-Barre, Pennsylvania.

6 A. Baltuska, Z. Wei, M.S. Pshenichnikov, and D.A. Wiersma, "Optical Pulse Compression to 5 fs at 1 MHz Repetition Rate," *Opt. Lett.* 22: 102 (1997); M. Nisoli, S. De Silvestri, O. Svelto, R. Szipöcs, K. Ferenz, C. Spielmann, S. Sartania, and F. Krausz, "Compression of High Energy Laser Pulses Below 5 fs," *Opt. Lett.* 22: 522 (1997).

7 I.D. Jung, F.X. Kärtner, N. Matuschek, D.H. Sutter, F. Morier-Genoud, G. Zhang, U. Keller, V. Scheuer, M. Tilsch, and T. Tschudi, "Self-Starting 6.5 fs from a Ti:Sapphire Laser," *Opt. Lett.* 22: 1009 (1997).

8 L. Xu, G. Tempea, C. Spielmann, F. Krausz, A. Stingl, K. Ferencz, and S. Takano, "Continuous-Wave Mode-locked Ti:Sapphire Laser Focusable to $5x10^{13}$ W/cm^2," *Opt. Lett.* 23: 789 (1998).

cal coherence tomography and time-resolved laser spectroscopy, ultrashort pulse laser sources at these high repetition rates are desired. In this project, pulses as short as 5 fs have been obtained directly from a Kerr-Lens modelocked Ti:sapphire laser[9] at 100 MHz repetition rate with an average output power of up to 200 mW. This has been made possible by the design and fabrication of improved double-chirped mirrors (DCMs) as described below. In combination with low dispersive CaF_2 prisms, these mirrors can control intracavity dispersion more precisely than has been possible previously.

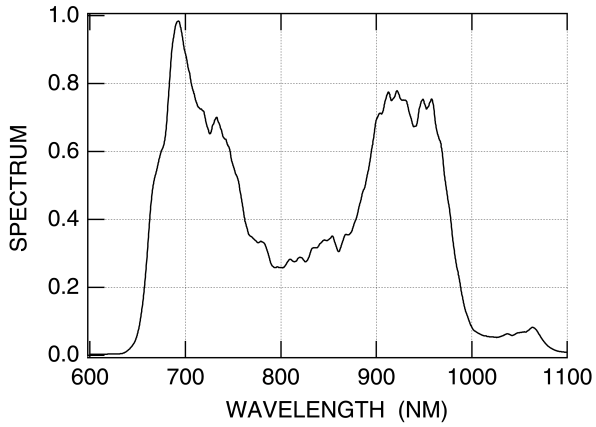

Figure 1. Spectrum measured with a calibrated spectrum analyzer.

Figure 1 shows the measured spectrum of the generated pulse that extends from 650 nm to almost 1100 nm. This spectrum is more than 150 nm broader than the spectrum reported previously for the 6.5 fs pulse.[10] A measurement of the interferometric autocorrelation (IAC) has been recorded simultaneously with the spectrum and is shown in Figure 2. Direct Fourier transformation of the pulse spectrum assuming no phase distortions over the whole spectrum results in a pulse width of the intensity envelope of only 4.9 fs, as illustrated by the solid curve in Figure 2. A fit of the measured (IAC) to that of a sinc-pulse would give 5.4 fs corresponding to only two optical cycles at a center wavelength of 800 nm. The good agreement of the measured IAC with the IAC derived from the spectrum as well as with the very conservative fit with a sinc suggests a pulse width close to 5 fs. The laser setup is a standard Z-fold cavity with a 100-MHz repetition rate. The modelocking mechanism is soft-aperture Kerr-Lens modelocking facilitated by the gain crystal. Displacement of one of the intracavity translation stages starts the modelocking.

The spectrum obtained from this source at high repetition rates enables many applications including broadband and multi-wavelength femtosecond spectroscopy, spread spectrum and WDM systems applications, as well as optical coherence tomography with sub-2 micron resolution.[11]

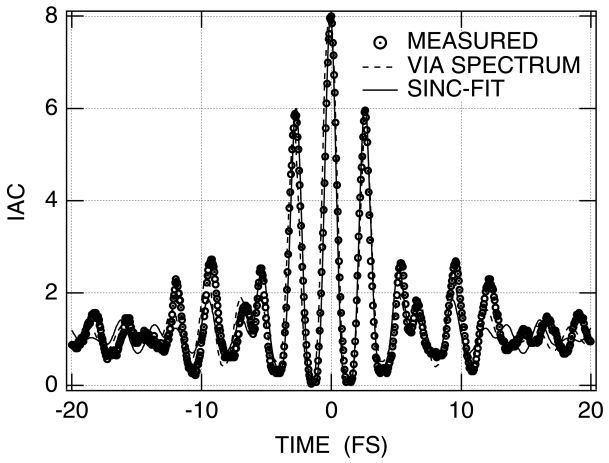

Figure 2. Measured interferometric autocorrelation of the Ti:sapphire laser. The solid line is the computed interferometric autocorrelation assuming zero phase over the measured spectrum in Figure 1 resulting in a 4.9 fs pulse.

1.1.1 Publications

Kärtner, F.X., U. Morgner, S.H. Cho, J. Fini, J.G. Fujimoto, and E.P. Ippen. "Advances in Short Pulse Generation." Invited talk presented at the Annual Meeting of the IEEE Laser and Electro-Optics Society, Orlando, Florida, December 1-4, 1998.

Kärtner, F.X., U. Morgner, S.H. Cho, Y. Chen, H.A. Haus, J.G. Fujimoto, and E.P. Ippen. "Ultrashort Pulse Generation with the Ti:Sapphire Laser."

9 U. Morgner, F.X. Kärtner, S.H. Cho, H.A. Haus, J.G. Fujimoto, E.P. Ippen, V. Scheuer, G. Angelov, and T. Tschudi, "Sub-Two Cycle Pulses from a Kerr-Lens Modelocked Ti:Sapphire Laser," *Opt. Lett.* 24: 411 (1999).

10 I.D. Jung, F.X. Kärtner, N. Matuschek, D.H. Sutter, F. Morier-Genoud, G. Zhang, U. Keller, V. Scheuer, M. Tilsch, and T. Tschudi, "Self-starting 6.5 fs from a Ti:Sapphire Laser," *Opt. Lett.* 22: 1009 (1997).

11 W. Drexler, U. Morgner, X. Li, S.A. Boppart, C. Pitris, F.X. Kärtner, S.H. Cho, E.P. Ippen, M.E. Brezinski, and J.G. Fujimoto, International Biomedical Optics Symposium, San Jose, California.

Paper presented at the International Conference on Lasers and Electro-Optics (CLEO 99), Baltimore, Maryland, May 23-28, 1999.

Morgner, U., S.H. Cho, J. Fini, F.X. Kärtner, H.A. Haus, J.G. Fujimoto, and E.P. Ippen. "5.5 fs Pulses from a Kerr-Lens Modelocked Ti:Sapphire Laser." Paper presented at the Advanced Solid-State Laser Conference (ASSL 99), Boston, Massachusetts, February 1-5, 1999.

Morgner, U., F.X. Kärtner, S.H. Cho, Y. Chen, H.A. Haus, J.G. Fujimoto, E.P. Ippen, E.P. Ippen, V. Scheuer, G. Angelov, and T. Tschudi. "Sub-two Cycle Pulses from a Kerr-Lens Modelocked Ti:Sapphire Laser." *Opt. Lett*. 24: 411 (1999).

1.2 Double-Chirped Mirror Technology

Sponsor

U.S. Air Force - Office of Scientific Research
Grant F49620-98-1-0139

Project Staff

Dr. Franz X. Kärtner, Professor Hermann A. Haus, Professor Erich P. Ippen, Professor James G. Fujimoto, Dr. Uwe Morgner

Standard laser mirrors are composed of quarter wave dielectric coatings and show a high-reflectivity bandwidth of about 200 nm for the wavelength range of Ti:sapphire around 800 nm. Such mirrors have considerable higher order dispersion outside the central high reflectivity range of only 100 nm bandwidth. This prohibits the generation of pulses shorter than 10 fs using such mirrors. Robert Szipöcs and Ferenz Krausz invented so called chirped mirrors,[12] in which longer wavelengths penetrate deeper into the mirror than shorter wavelengths since the Bragg wavelength is varied linearly during layer growth.

This technique automatically leads to a broader high reflectivity range, and it generates negative dispersion that can be used to compensate the positive dispersion and higher order dispersion of the laser crystal. Use of this technology led to the generation of 7.5 fs pulses directly from the laser oscillator[13] and fs pulses tunable over 300 nm from a commercial laser equipped with a single set of broadband chirped mirrors.[14]

Recently, the main problem in the design of chirped mirrors has been identified as a matching problem for the long wavelengths which penetrate deeply into the mirror before being reflected. Small reflections in the front section of the mirror lead to large oscillations in the group delay and group delay dispersion, which prevent locking of the complete spectrum over the full high reflectivity range of the mirror. These Gire-Tournois like interference effects can be consistently avoided by chirping not only the Bragg wavelength of the mirror but also the coupling coefficient of the Bragg mirror by increasing the thickness of the high index layer gradually which results in double-chirped mirrors.[15] For the fabrication of these mirrors, high accuracy in the layer growth is indispensable.[16] With double-chirped mirrors in a Ti:sapphire laser to correct for the higher order dispersion of the prism pair, laser crystal pulses as short as 6.5 fs have been generated.

Recently, a new set of double chirped mirrors has been designed and fabricated which shows about three times lower oscillations in the group delay dispersion. Figure 3 shows the reflectivity, and the desired and designed group delay of the new double-chirped mirrors. The mirrors show a high reflectivity of more than 99.8% over a wavelength range of 350 nm and a good transmission for the Argon pump light around 500 nm. The designed group delay follows the desired group delay within a deviation of only 0.3 fs over the full high reflectivity range of 350 nm. These mirrors led to the generation of pulses shorter than two optical cycles directly from a Kerr-Lens modelocked Ti:sapphire laser.

12 R. Szipöcs, K. Ferencz, C. Spielmann, and F. Krausz, "Chirped Multilayer Coatings for Broadband Dispersion Control in Femtosecond Lasers," *Opt. Lett.* 19: 201 (1994); R. Szipöcs and A. Kohazi-Kis, "Theory and Design of Chirped Dielectric Laser Mirrors," *Appl. Phys. B* 65: 115 (1997).

13 A. Stingl, M. Lenzner, C. Spielmann, F. Krausz, and R. Szipöcs, "Sub-10-fs Mirror-Dispersion-Controlled Ti:Sapphire Laser," *Opt. Lett*. 20: 602 (1995).

14 E.J. Mayer, J. Möbius, A. Euteneuer, W.W. Rühle, and R. Szipöcs, "Ultrabroadband Chirped Mirrors for Femtosecond Lasers," *Opt. Lett.* 22: 528 (1997).

15 N. Matuschek, F.X. Kärtner, and U. Keller, "Theory of Double-Chirped Mirrors," *IEEE J. Sel. Topics Quantum Electron.* 4: 197 (1998).

16 M. Tilsch, V. Scheuer, J. Staub, and T. Tschudi, "Direct Optical Monitoring Instrument with a Double Detection System for the Control of Multilayer Systems from the Visible to the Near Infrared," *SPIE Proc.* 2253: 414 (1994).

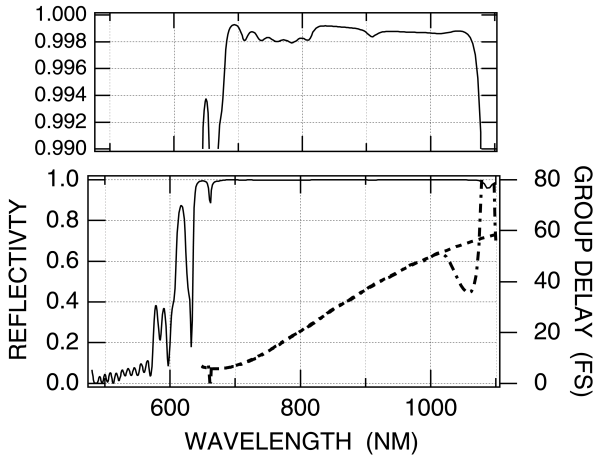

Figure 3. Reflectivity (____), desired (- - -) and designed (-.-.-.-) group delay of broadband double-chirped mirrors.

1.3 Dispersion Managed Modelocking

Sponsors

Defense Advanced Research Projects Agency
Grant F49620-96-1-0126
Joint Services Electronics Program
Grant DAAH04-95-1-0038
National Science Foundation
Grant ECS 94-23737
U.S. Air Force - Office of Scientific Research
Grant F49620-98-1-0139

Project Staff

Dr. Franz X. Kärtner, Professor Hermann A. Haus, Professor Erich P. Ippen, Professor James G. Fujimoto, Dr. Yijiang Chen, Dr. Uwe Morgner, Seong-Ho Cho

In addition to achieving record-short pulse durations from a Kerr-lens-modelocked (KLM) Ti:sapphire laser, we have also obtained a better understanding of the modelocking operation by extensive computer simulations. The computer simulations use only a few essential ingredients. In contrast to the work of Christov et. al.,[17] our simulations are one-dimensional. The simulations include the dispersion of the laser optics, the finite gain bandwidth and self-phase modulation of Ti:sapphire.

The KLM was modeled by a fast saturable absorber. The resulting model is in one-to-one correspondence with the model of dispersion-managed pulse propagation, now a topic of intense interest, since it promises to improve the bit-rates for long distance fiber communications. The computer simulations show that the major pulse shaping under steady state operation is due to the formation of a dispersion-managed soliton. Therefore, we have dubbed this model of modelocking dispersion managed modelocking (DMM) in analogy to soliton modelocking of fiber lasers.

The soliton modelocking model of fiber lasers attributes the pulse shaping to the soliton formation process in the fiber. Filtering and the artificial saturable absorber (APM action) are only small perturbations in the final pulse shaping process. Their main function is to initiate the pulse forming process and suppress build-up of cw radiation. An analogous picture emerges for the DMM process. Thus, we have demonstrated that three-dimensional effects of the dynamics of the self-focusing are mostly important for explaining the creation of the artificial saturable absorber effect and not the major pulse shaping dynamics. Because strong self-focusing in the gain medium can only occur when the pulse is compressed during propagation through the gain medium, the temporal dynamics of dispersion managed solitons suggest that a symmetric distribution of the negative dispersion in the two arms of a linear resonator leads to improved modelocking. It is only then that the pulse utilizes the self-focusing in the gain medium in each path.

Fine structures in the spectrum was also successfully reproduced by the computer simulation by refinements of the model. If we included the reflectivity and phase of the mirrors and an additional model for saturated Kerr-lens-modelocking that enhances the peaks of lower intensity relative to the peak intensity, then the magnitude of the spectral modulation observed in the experimental spectrum has been also reproduced, see Figure 4. These extensive studies suggest that we have not yet reached the ultimate pulse limit. Improvement in the mirror design and symmetrization of the dispersion distribution within one roundtrip could lead to further pulse shortening of the generated pulses down to the single cycle regime.

17 P. Christov and V.D. Stoev, "Kerr-Lens Modelocked Laser Model: Role of Space-Time Effects," *J. Opt. Soc. Am. B.* 15: 1960 (1998).

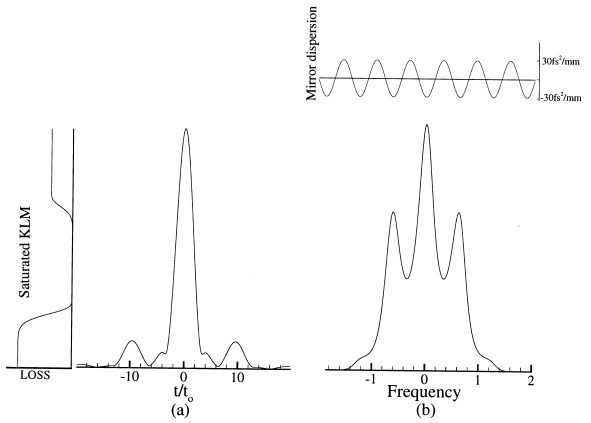

Figure 4. Simulated steady-state pulse spectrum and intensity of a sub-10 fs laser including saturated Kerr-lens modelocking and group delay dispersion oscillations due to the dispersion compensating mirrors.

1.3.1 Journal Articles

Chen, Y., F.X. Kärtner, U. Morgner, S.H. Cho, H.A. Haus, J.G. Fujimoto, and E.P. Ippen. "Dispersion Managed Mode-locking." *Opt. Soc. Am. B*. Forthcoming.

Kärtner, F.X., D. Zumbühl, and N. Matuschek. "Turbulence in Modelocked Lasers." *Phy. Rev. Lett.* Forthcoming.

1.4 Stretched Pulse Propagation

Sponsors

Defense Advanced Research Projects Agency
Grant F49620-96-0126

MIT Lincoln Laboratory
Contract BX-6888

Project Staff

Professor Hermann A. Haus, Dr. Yijiang Chen

Long-distance propagation over dispersion managed fibers using linear methods of propagation has met with resounding success. The cables laid in 1995 between the United States and Europe and the United States and Japan are performing flawlessly at 5 Gb/s. Extensive wavelength division multiplexing (WDM) giving bit rates up to one Terabit/s have been demonstrated in the laboratory. Elegant proposals for soliton propagation have remained just proposals, since the "conventional" form of transmission is performing so well.

Soliton propagation offers the advantage of higher signal-to-noise ratios since the nonlinearity of the fiber is co-opted in the formation of solitons. Dispersion managed nonlinear pulse propagation is feasible at zero net dispersion. This eliminates the Gordon-Haus effect. The dispersion managed nonlinear propagation will win out when it has been demonstrated that the following aspects are realizable (1) larger amplifier spacings; (2) higher bit-rates per channel, up to 40Gb/s; and (3) extensive WDM'ing.

We have been pursuing computer simulations and analytic studies of nonlinear pulse propagation. As mentioned, the Gordon-Haus effect is eliminated at zero net dispersion. What remains is the effect of pulse jitter due to position shifts per amplifier, but these effects are much smaller than the Gordon-Haus effect. We have studied collision processes which indeed pose a challenge to the cable designer. Collision effects can be greatly reduced by the introduction of periodic filters. Analytic expressions of the collision effect have been confirmed by computer simulation.

We have also developed a model for dispersion managed pulse propagation that helps to interpret the nonlinear pulse formation. We have dubbed it "nonlinear Bloch" waves in the periodic dispersion managed structure. The nonlinearity produces a self-consistent periodic scattering potential that makes possible the periodic regeneration of the pulse, except for a phase shift from period to period.

1.5 Modelocking Er/Yb Waveguide Lasers with Semiconductor Saturable Absorber Mirrors

Sponsors

Defense Advanced Research Projects Agency
Grant F49620-96-0126

U.S. Air Force - Office of Scientific Research
Grant F49620-98-1-0139

Project Staff

Erik R. Thoen, Elisabeth M. Koontz, Dr. David J. Jones, Dr. Patrick Langlois, Dr. Markus Joschko, Dr. Franz X. Kärtner, Professor Erich P. Ippen, Professor Leslie A. Kolodziejski

Fiber lasers typically operate at low fundamental repetition rates because the maximum Er-doping density in silica fiber requires long-gain sections for fiber lasers. In a co-doped Erbium/Ytterbium (Er/Yb) phos-

phate glass waveguide the density of Erbium is significantly larger, providing much higher gain per length than Erbium-doped fiber and making short cavity fiber lasers possible. A modelocked fiber laser based on an Er/Yb codoped waveguide amplifier has been demonstrated using the P-APM modelocking mechanism.[18] Using a semiconductor saturable absorber mirror instead of P-APM for the modelocking mechanism permits shortening the cavity still further. We have used a semiconductor saturable absorber mirror to produce pulses as short as 1 ps at repetition rates of 25-100 MHz from a modelocked Er/Yb waveguide laser. We have also used a linear cavity configuration that is scalable to higher repetition rates.

The semiconductor saturable absorber mirror consists of an anti reflection coated half-wave InP-based absorber structure deposited by gas source molecular beam epitaxy on a distributed Bragg reflector (DBR). The DBR contains 22 pairs of quarter-wave AlAs/GaAs and produces >99% reflectivity over ~100 nm, centered at 1550 nm. The absorber layer consists of six InGaAs quantum wells (exhibiting photoluminescence at $\lambda \sim 1580$ nm) centered within the half-wave layer for maximum interaction with the standing wave formed by the mirror.

Saturation fluence measurements of the structure reveal ~10% saturable absorption and ~5% non-saturable loss and indicate that two photon absorption provides an optical-limiting effect that suppresses Q-switching instabilities. The time response of the absorber was characterized via reflection pump-probe measurements, using 130 fs pulses at 1530 nm and an incident fluence (~100 $\mu J/cm^2$) similar to that within the modelocked laser cavity. The pump-probe response reveals a fast recovery time of 350 fs and a slow time constant of 32 ps.

Modelocked operation was obtained in the cavity configuration shown in Figure 5, using 150-250 mW of pump power at 980 nm. The strong Er/Yb gain peak of the waveguide at 1534 nm necessitates the use of filtering within the cavity in order to obtain a broad modelocked spectrum. In the free space portion of the cavity, a dielectric normal-incidence high reflector at 1550 nm is angled to produce a tunable edge filter and a quarter-wave plate controls the polarization-dependent loss. Using this filtering technique, the shortest pulses of 1-ps in duration were generated with a 2 nm spectral width at an output power of 0.63 mW (see Figure 6). More generally, 3 ps pulses could be produced over the wavelength range 1542-1553 nm with 1.2 mW of output power for both 50 and 100 MHz repetition rates. Without gain filtering, a modelocked state occurred only at 1534 nm with an Er/Yb gain profile-limited pulsewidth of ~8 ps. In summary, for the first time, 1 ps pulses have been produced in a scalable, gain-filtered, modelocked Er/Yb waveguide laser using a semiconductor saturable absorber mirror.

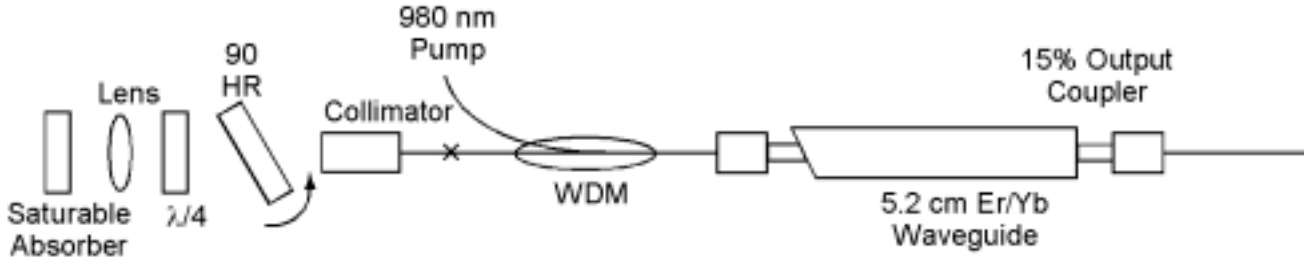

Figure 5. Schematic of the modelocked Er/Yb waveguide laser cavity. The 15% output coupler is a coated fiber end, butt-coupled with index matching fluid to the waveguide. The 5.2 cm Er/Yb waveguide is angle-polished on the intra-cavity side and is butt-coupled with index matching fluid to an angle-polished fiber. A wavelength division multiplexer (WDM) is used to couple the laser diode pump to the waveguide. The high reflector (HR) and polarization controller act as the gain-filtering mechanism, and a 6 mm focal length aspheric lens is used to focus on the saturable absorber mirror.

18 D.J. Jones, S. Namiki, D. Barbier, E.P. Ippen, and H.A. Haus, *IEEE Photon. Technol. Lett.* 10: 666 (1998).

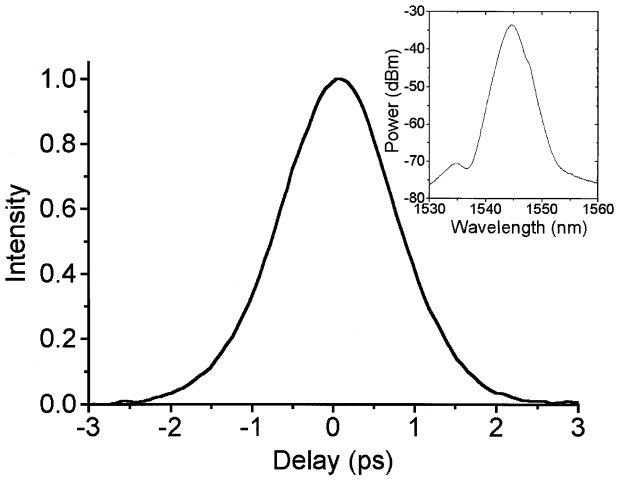

Figure 6. Second harmonic generation autocorrelation of the 1 ps sech-shaped pulse. The inset shows the corresponding optical spectrum with a full-width-half-maximum of 2.5 nm.

1.5.1 Meeting Paper

Thoen, E.R., E.M. Koontz, D.J. Jones, P. Langlois, F.X. Kärtner, E.P. Ippen, L.A. Kolodziejski, and D. Barbier. "Picosecond Pulses from an Er/Yb Waveguide Laser Passively Mode-locked with a Semiconductor Saturable Absorber Mirror." Paper to be presented at the Conference on Lasers and Electro-Optics (CLEO 99), Baltimore, Maryland, May 23-28, 1999.

1.6 Laser Dynamics Using Two-Photon Absorbing Semiconductor Saturable Absorber Mirrors

Sponsors

Defense Advanced Research Projects Agency
Grant F49620-96-0126

U.S. Air Force - Office of Scientific Research
Grant F49620-98-1-0139

Project Staff

Erik R. Thoen, Elisabeth M. Koontz, Dr. David J. Jones, Thomas R. Schibli, Dr. Markus Joschko, Dr. Patrick Langlois, Dr. Franz X. Kärtner, Professor Erich P. Ippen, Professor Leslie A. Kolodziejski

The importance of modelocking lasers using semiconductor saturable absorbers necessitates a more thorough investigation of the saturable absorber nonlinearities. For this reason, we have recently performed femtosecond pulse saturation measurements of a resonantly-coated InGaAs/InP semiconductor saturable absorber mirror. Our studies reveal the presence of two-photon absorption at energy densities obtainable in modelocked fiber and waveguide lasers. We have also made observations of the dynamics of an Er/Yb waveguide laser modelocked by this absorber that indicate that two-photon absorption is responsible for both restricting the minimum pulsewidth and suppressing Q-switched-modelocking.

Figure 7 depicts the semiconductor saturable absorber mirror deposited by gas source molecular beam epitaxy. The absorber structure consists of four InGaAs quantum wells centered within an InP half-wave layer, providing maximum overlap with the standing wave field formed by the distributed Bragg reflector. A five layer dielectric top reflector resonantly enhances the device absorption at 1530 nm, the wavelength at which the Er/Yb waveguide provides maximum gain.

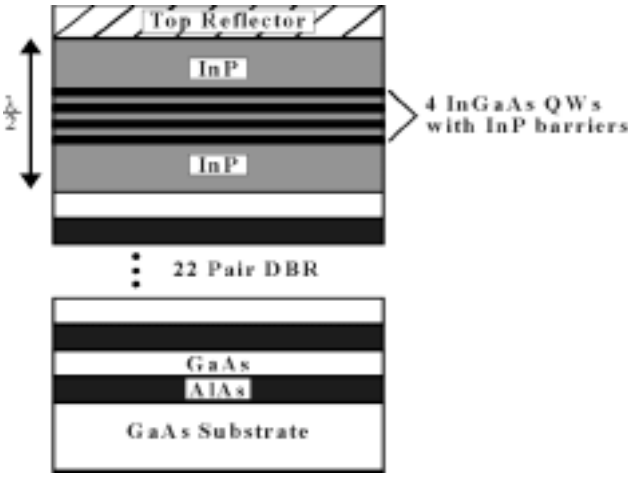

Figure 7. InGaAs/InP semiconductor saturable absorber structure on an AlAs/GaAs distributed Bragg reflector (DBR). The 4 quantum wells exhibit photoluminescence at I ~ 1.53 m.

Reflectivity measurements to characterize the semiconductor saturable absorber mirror as a function of incident energy fluence, with 150 fs pulses at 1530 nm, are shown in Figure 8. Saturation of the absorption at low energy densities and a decrease in reflectivity resulting from two-photon absorption at high energy densities is observed. The solid line is a theoretical fit to the data assuming a simple saturable absorption model for the quantum wells and using the known InP two-photon absorption coefficient (ß = 90 GW/cm^2), the measured spot size of the beam,

and a pulsewidth of 150 fs. Utilizing the same parameters, saturation curves for 1 and 8 ps pulses are calculated (see Figure 8).

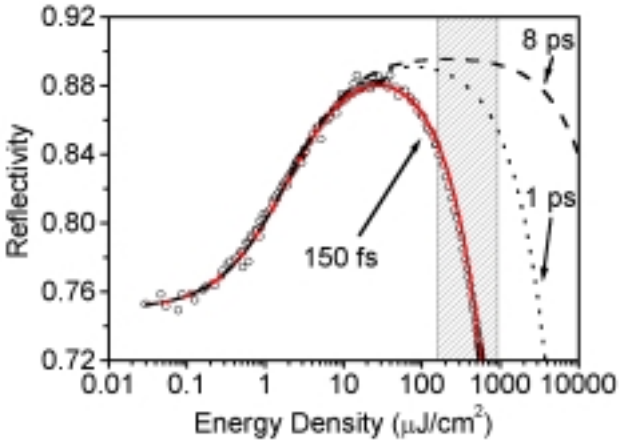

Figure 8. Measurement of the semiconductor absorber mirror reflectivity as a function of incident energy fluence using 150 fs pulses at 1530 nm (circles). The solid line is a fit to the data using a simple absorber model incorporating two-photon absorption in the InP layers. Utilizing the fitting parameters from the measurement, similar curves are calculated for 1 ps (dot) and 8 ps (dash) pulses.

When the InGaAs/InP semiconductor saturable absorber mirror is used to modelock the Er/Yb-waveguide laser similar to that shown in Figure 5, stable cw-modelocking is observed within a limited power range. The shaded region in Figure 8 corresponds to the energy densities incident on the absorber during stable cw-modelocking. A long absorber recovery time and the long Er/Yb gain lifetime contribute to the difficulty of suppressing Q-switched-modelocking. The observed range of cw-modelocking is consistent with the predicted saturation energy response for 8 ps pulses (see Figure 8), suggesting Q-switched modelocking is suppressed by two-photon absorption. Simultaneously, however, the strong dependence of two-photon absorption on peak intensity limits the minimum possible pulsewidth for a given power level. For example, the generation of femtosecond pulses, with this InGaAs/InP resonant saturable absorber and the energy densities in the current laser cavity, is unfavorable due to the predicted onset of two-photon absorption (see Figure 8). Further experiments with picosecond and femtosecond fiber lasers will provide a more in-depth understanding of the two-photon absorption effects.

1.6.1 Meeting Paper

Thoen, E.R., E.M. Koontz, D.J. Jones, F.X. Kärtner, E.P. Ippen, L.A. Kolodziejski, and D. Barbier. "Suppression of Instabilities and Pulsewidth Limitation by Two-photon Absorption in a Mode-locked Laser." Paper to be presented at the Conference on Lasers and Electro-Optics (CLEO 99), Baltimore, Maryland, May 23-28, 1999.

1.7 Soliton Squeezing in Optical Fiber

Sponsor

U.S. Navy - Office of Naval Research
Grant N00014-92-J-1302

Project Staff

Charles X. Yu, Dr. Moti Margalit, Professor Hermann A. Haus, Professor Erich P. Ippen

Squeezed quantum states of the electromagnetic field are states that have reduced fluctuations in one phase of the field at the expense of increased fluctuations in the quadrature phase. If employed in the measurement of either phase or amplitude of an electromagnetic field, they lead to detection at sub-shot noise level. We have pursued the generation of squeezed states in fibers. Since their use in measurements has to be accomplished with minimum loss. Single-mode fibers and their interconnections can be made with very small insertion losses. The squeezed radiation can be applied conveniently to a fiber interferometer for reduced-noise phase measurements.

Past efforts to observe soliton squeezing have largely been frustrated by guided acoustic-wave Brillouin scattering (GAWBS).[19] GAWBS is a phase noise generated in fiber due to the fiber's acoustic modes that can not be cancelled through balanced detection. GAWBS usually has frequency content from 20 MHz to 1 GHz. We are currently pursuing two approaches to combat the effects of GAWBS. The first one is to use a short piece of fiber, which will make the amount of GAWBS negligible. To achieve the required nonlinearity, we use short pulses with high peak power (~100 fs). A short pulse implies a broad spectrum. The optical beam splitter necessary for this experiment must have flat splitting ratios

19 R. Shelby, M. Levenson, and P. Bayer, "Guided Acoustic-wave Brillouin Scattering," *Phys. Rev. B.* 31: 5244-52 (1985).

across the entire spectrum. We are currently working with colleagues at MIT Lincoln Laboratory to fabricate a broadband beamsplitter.

The second approach is to use a pulsed source whose repetition rate is greater than 1 GHz. Squeezing can then be observed between GAWBS spikes. We have achieved a 1 GHz fiber laser source using harmonic modelocking.[20] To reach the soliton condition we need ~150 mW in one single polarization. Such power is difficult to achieve directly from the laser or even from a conventional fiber amplifier. We are currently working on a double-clad fiber amplifier with Lucent Technologies. The goal is to achieve 1 watt saturated power from this amplifier.

1.8 Modelocking of Er:Yb:glass

Sponsors

Charles S. Draper Laboratory
Contract DL-H-513222
U.S. Air Force - Office of Scientific Research
Grant F49620-98-1-0139
U.S. Navy - Office of Naval Research
Grant N00014-92-J-1302

Project Staff

Charles X. Yu, Seong-Ho Cho, Professor Hermann A. Haus, Professor James G. Fujimoto, Professor Erich P. Ippen, Dr. Franz X. Kärtner

The communication window at 1550 nm is a very important one for low loss applications. Modelocked sources at this wavelength are mainly Er-doped fiber lasers[21] and semiconductor lasers.[22] The Er-doped fiber lasers have lower noise levels than semiconductor lasers and provide pulses as short as 50 fs. However, due to the long length of the Er fiber (>1 meter), its fundamental repetition rate is on the order of 50 MHz. While these lasers can be harmonically modelocked to provide up to 10 GHz repetition rates, the electronics necessary for such operations make the laser system large and cumbersome. On the other hand, semiconductor lasers can be made high repetition rate because of their small size. However, it is difficult to generate pulses shorter than 1 psec. Furthermore, these semiconductor lasers are susceptible to higher spontaneous emission noise because of their nanosecond upperstate lifetime.

We use a short piece (~1.5 mm) of Er-doped phosphate glass[23] as the gain medium. By using phosphate glass as the host material, the erbium concentration can be made much higher than in fibers. By avoiding the fiber format, we also avoid the coupling loss when the light is launched into the fiber. Both allow us to use a very short piece of glass. We are currently working on a 1 GHz laser cavity using Kerr-lens modelocking (KLM) to produce short pulses.

Figure 9 shows the laser cavity layout. The gain medium is the Er:glass, the back side of which is HR coated to form one of the end mirrors. The other side is wedged by 10 degrees and AR coated to minimize the reflection. A concave mirror (R = 5 cm) is placed approximately one focal length away so the mode is focused in the gain medium. The cavity is completed by a 1% output coupler. The pump light is at 977 nm. So far, we have achieved CW lasing. The lasing threshold is 150 mW pump power at 977 nm. The maximum output is 80 mW at an incidence pump power of 450 mW. The intracavity power is thus 8 watts, which is close to the modelocking threshold. We are currently optimizing the pump-signal overlap and cavity dispersion to attempt modelocking.

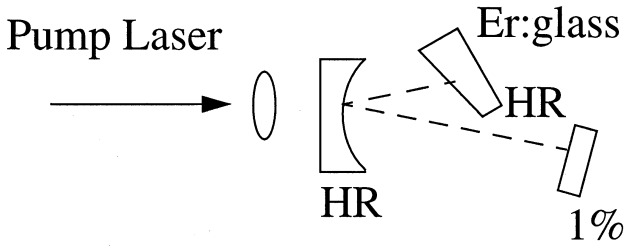

Figure 9. Laser cavity.

20 M. Margalit, C. Yu, E.P. Ippen and H.A. Haus, "Harmonic Mode-locking using Regenerative Phase Modulation," *IEEE Photon. Tech. Lett.* 10: 337-9 (1998).

21 K. Tamura, E.P. Ippen, H.A. Haus, and L. Nelson, "77-fs Pulse Generation from a Stretched-Pulse Modelocked All-Fiber Ring Laser," *Opt. Lett.* 18: 1080-82 (1993).

22 E. Zielinski, E. Lach, J. Bouayad-Amine, H. Haisch, E Kuhn, M. Schilling, and J. Weber, "Monolithic Multisegment Mode-locked DBR Laser for Wavelegnth Tunable Picosecond Pulse Generation," *J. Quan. Electron.* 3: 230-33 (1997).

23 S. Jiang, J. Myers, D. Rhonehouse, M. Myers, R. Belford, and S. Hamlin, "Laser and Thermal Performance of a New Erbium Doped Phosphate Laser Glass," *SPIE Proc.* 2138 (1994).

1.9 Passively Modelocked Fiber Laser Source for Gyroscopes and Other Applications

Sponsor

Charles S. Draper Laboratory
Contract DL-H-513222

Project Staff

Patrick C. Chou, Professor Hermann A. Haus

The interferometric fiberoptic gyroscope (IFOG) is a lower cost alternative to the ring laser gyro for inertial navigation. IFOG performance has been improving steadily in the past three decades, now competing with ring laser gyroscope. The ideal optical source for an IFOG must provide adequate power and a broad Gaussian optical spectrum, which is essential for a short coherence function with low sidelobes. The low coherence is important for reducing error due to coherent backscattering in the gyro. We propose a passively modelocked erbium doped fiber laser as a gyro source.

The standard optical source for an IFOG is the superluminescent diode, which is traditionally difficult to couple to an optical fiber mode and has limited spectral width. Also under development now are erbium doped fiber fluorescence sources whose mean wavelengths are difficult to stabilize. The modelocked fiber laser provides the best of both worlds. It is inherently fiber compatible and can generate power and spectral widths several times larger, and the spectrum can be externally processed for stability and smoothness via simple time domain techniques.

One key difference is that the modelocked source generates ultrashort pulses while a fluorescence source generates continuous-wave radiation. An initial concern with the modelocked source is that the high peak intensities of the pulses would cause errors due to optical nonlinearity in the fiber of the gyro. We tested this and found that indeed there is a Kerr induced bias offset in the gyro signal. However, we have shown that by simply stretching the pulses with a highly dispersive medium before they enter the gyro coil, the peak intensity is reduced and the bias disappears.[24] This bias reduction is illustrated in Figure 10.

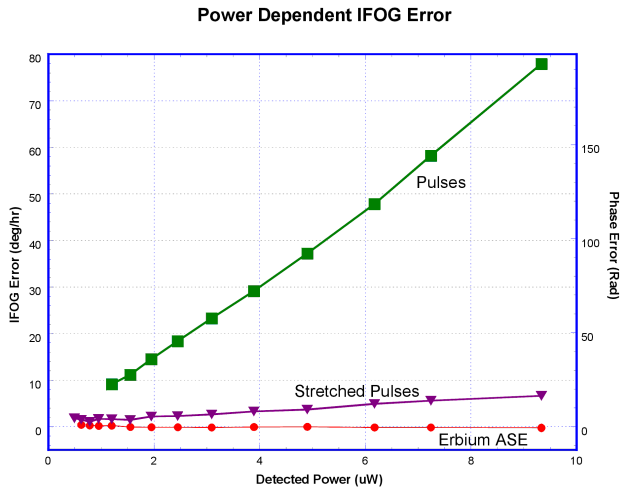

Figure 10. Power dependent IFOG error. When erbium amplified spontaneous emission (fluorescence) is used as a source, there is no observable error.

One clear advantage of using pulses is that time domain processing techniques are available as mentioned above. The technique is the following: the pulses are stretched with the same dispersive medium used to reduce peak intensity; the pulses are now so highly chirped that their optical frequency components are separated temporally. Therefore, by applying amplitude modulation during different time windows within a pulse, one can effectively create arbitrarily shaped optical filters. Any spectral spikes, which would normally cause sidelobes in the coherence function, can then be suppressed, regardless of their locations and heights. Figure 11 shows the response of an effective notch filter implemented this way, demonstrating a less than 5 nm resolution and a greater than 9 dB suppression.

24 P.C. Chou, H.A. Haus, and O.M. Laznicka, “Pulse Excited Interferometric Fiber-Optic Gyroscope," *Proceedings of the Conference on Lasers and Electro-Optics 1998 Technical Digest Series,* paper CWR5, pp. 313-14.

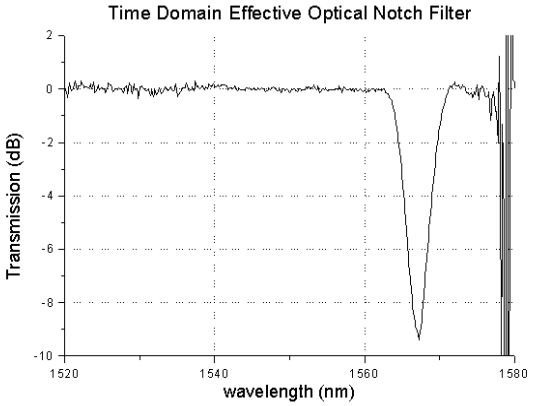

Figure 11. Effective optical notch filter. This effective filter is implemented by applying appropriately timed amplitude to highly chirped pulses. No real optical filter is involved.

This work also benefits areas other than gyroscopes. A broad spectrum source is useful for optical coherence tomography and other coherence based imaging systems. The ultrashort pulses generated by a compact fiber laser can also be applied toward two photon microscopy and optical sampling.

1.10 Photon Statistics of Non-Return-to-Zero (NRZ) Signals in a High-bit-rate Optically Pre-amplified Direct Detection Receiver

Sponsor

Defense Advanced Research Projects Agency
Grant F49620-96-0126

Project Staff

William S. Wong, Professor Hermann A. Haus, Leaf A. Jiang, Jeffrey Korn

The determination of receiver sensitivity and bit-error rate (BER) is important in the design of high bit rate optical digital communication systems. Amplified spontaneous emission (ASE) from optical amplifiers degrades the SNR and thus impairs BER. A typical eye-diagram of a 10 Gb/s NRZ transmission is shown in Figure 12, where the horizontal axis is time (20 ps/div). On the same plot, a histogram of photocurrent counts is overlaid where the counts are drawn on a logarithmic scale (20 dB/div). From the eye diagram, one can collect histogram counts, which ultimately lead to the determination of the BER.

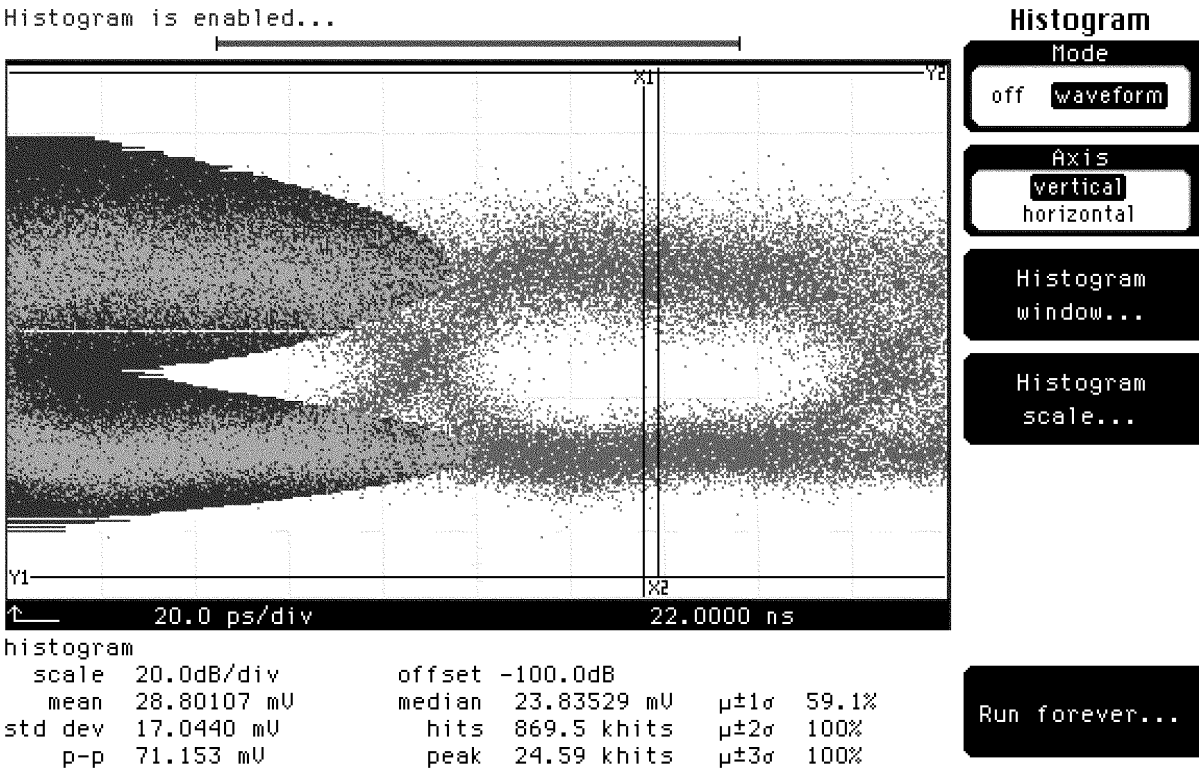

Figure 12. A typical eye-diagram of a 10 Gb/s NRZ transmission.

There exist two classes of models for the analysis of the (noisy) signal distributions in a pre-amplified OOK (on-off keying) receiver. The first class uses the semiclassical square-law model for detection, resulting in a Gaussian distribution for the photocurrent.[25] The second class uses a quantum treatment of spontaneous and stimulated processes in the optical amplifier.[26] The advantages of the semiclassical models are simplicity and the fact that they yield approximate yet analytical expressions for the BER. The advantage of the quantum mechanical models is correctness and accuracy in describing the physical processes.

In collaboration with Lucent Technologies, Bell Laboratories, and MIT Lincoln Laboratory, we confirmed experimentally the non-Gaussian nature of the ASE photon distribution by showing that it was degenerate Bose-Einstein, a quantum-mechanical prediction.[27] We further demonstrate experimentally that the photon distribution of the ONE state in an OOK pre-amplified receiver is non-Gaussian and can be described quantum mechanically by a noncentral-negative-binomial distribution.[28] Our findings are the first direct demonstration of the accuracy of the quantum mechanical receiver models describing both the ZEROs and ONEs.

The experimental setup is as follows. The receiver consists of an optical attenuator to adjust the received power, an EDFA pre-amplifier pumped at 980 nm, an optical bandpass filter with center wavelength 1550 nm and 3 dB bandwidth of 1.0 nm to provide rejection of out-of-band noise, a 30 GHz pin detector with a conversion gain of 24.83 V/W, and a 30 GHz dc-coupled digital sampling oscilloscope. A second attenuator is used to prevent the pin detector from saturating. For calibration, we measure the detection circuit's thermal noise by blocking the detector input and obtaining the distribution of voltages on the oscilloscope. The voltage levels are then converted to a noise equivalent optical power, whose histogram is shown in Figure 13. The circuit noise distribution is found to be Gaussian with a standard deviation of 12.5 mW, or a noise equivalent power of 72 pW$\sqrt{\text{Hz}}$.

The photon distribution of ASE noise of the pre-amplifier on the oscilloscope is obtained by blocking the incident light at the pre-amplifier and unblocking the pin detector. Using the measured circuit noise distribution, the theoretical distribution of the ASE noise is computed by convolving the degenerate Bose-Einstein distribution with the Gaussian distribution. The ASE histogram data, collected with 10^7 hits, are then fitted with this composite distribution, shown in Figure 13 in a logarithmic scale. The two degrees of freedom used in fitting are the mean photon number per mode $\bar{n}$ and the degeneracy factor g. The parameter $\bar{n}$ is found to be 2040, and g is 8.5, which is very close to the expected value of the optical bandwidth divided by the electrical bandwidth while accounting for the two degrees of polarization (125 GHz / 30 GHz $\times$ 2 = 8.3).

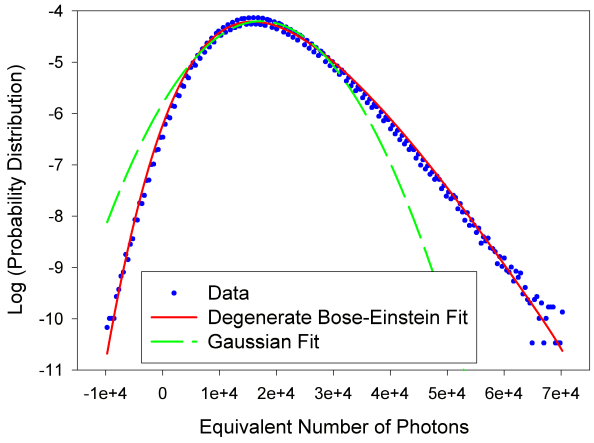

Figure 13. Probability distribution of the ASE/ZEROs (circles), a degenerate Bose-Einstein fit (solid line), and a Gaussian fit (dotted line).

Next, the photon distribution of the amplified ONEs is obtained by injecting –34 dBm of coherent light ($\bar{n}_s = 60$) from a DFB laser at 1550 nm into the receiver. The histogram data are shown in Figure 14, from which one can see clearly the non-Gaussian nature of the distribution. The NNB fit, agreeing very well with the experimental data over a dynamic range of 58 dB, yields $\bar{n}$ = 2110, g = 8.5, and $\bar{n}_s$ = 60. One can see that the Gaussian fit to the data is not satis-

25 S.D. Personick, *Bell Syst. Tech. J.* 52: 117 (1973); L.G. Kazovsky and O.K. Tonguz, *IEEE Photonics Technol. Lett.* 3: 53 (1991); R.C. Steele, G.R. Walker, and N.G. Walker, *IEEE Photon. Technol. Lett.* 3: 545 (1991).

26 T. Li and M.C. Teich, *Electron. Lett.* 27: 698 (1991); P. Diament and M.C. Teich, *IEEE J. Quan. Elec.* 28: 1325 (1992); T. Li and M.C. Teich, *IEEE J. Quan. Elec.* 29: 2568 (1993).

27 W.S. Wong, H.A. Haus, L.A. Jiang, P.B. Hansen, and M. Margalit, *Opt. Lett.* 23: 1832 (1998); K. Shimoda, G. Takahashi, and C.H. Townes, *Phys. Soc. Jpn.* 12: 686 (1957); L. Mandel, *Proc. Phys. Soc.* (London) 74: 233 (1959).

28 J. Pervina, *Phys. Lett.* 24A: 333 (1967).

factory. As pointed out theoretically in,[29] around the optimal decision threshold, the Gaussian model tends to underestimate the tails of the probability distributions of the ZEROs while overestimating those of the ONEs.

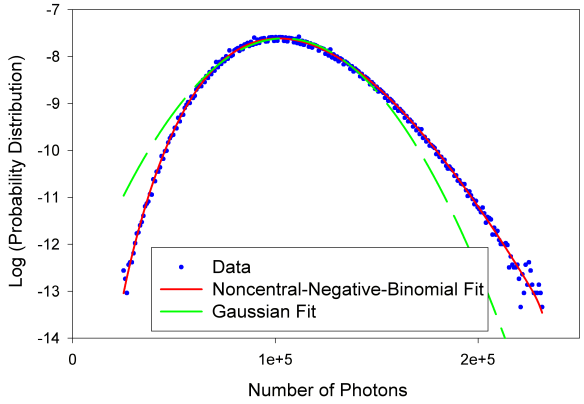

Figure 14. Probability distribution of the ONEs (circles), a noncentral-negative-binomial fit (solid), and a Gaussian fit (dotted line).

1.11 High-Density Optical Integration

Sponsors

Charles S. Draper Laboratory
Contract DL-H-513222
U.S. Air Force - Office of Scientific Research
Grant F49620-98-1-0139
University of Maryland - Laboratory for Physical Sciences
Contract MDA 90497C0476

Project Staff

Dr. Brent E. Little, Christina Manolatou, Mohammed J. Khan, Professor Hermann A. Haus, Dr. Pierre R. Villeneuve, Professor John D. Joannopoulos, Professor Erich P. Ippen, Dr. Shanhui Fan, J.S. Foresi, Günter Steinmeyer, Erik R. Thoen, Dr. S.T. Chu, Professor Lionel C. Kimerling, W. Greene

We are investigating the possibility of large-scale optical integration of high index contrast structures. In the preceding year, we worked on the theory and design of resonant channel dropping filters that perform the same function as a ring resonator filter but using standing wave modes instead of traveling waves. This type of filter was first analyzed theoretically using group theory arguments and demonstrated with FDTD simulations of photonic crystal microcavities.[30] Our theoretical approach is based on coupled mode theory which provides an intuitive understanding of the operating principle and reveals analogies with standard filter design. It has been shown that a symmetric system consisting of a pair of standing resonant modes between two waveguides functions as a channel dropping filter if the two modes are degenerate.

This can be achieved by proper design; the mutual coupling between the two modes is counteracted by the indirect coupling via the waveguides. We investigated the possibility of implementing such a filter using high index contrast standing wave resonators. Performing extensive FDTD simulations mostly in two dimensions, we calculated parameters such as radiation and coupling Q's for resonators of different shapes and sizes. The simplest structure, a square resonator, was found to support high Q modes with the nodal lines of the electric field along the diagonals.

When two identical such resonators were placed between two waveguides with the appropriate spacings, the numerical simulations showed agreement with the theoretical predictions but also revealed the sensitivity of the response to geometrical design parameters.[31] The small size of these resonators may allow combining many of them together to produce responses with flatter tops and faster roll off since the single pole Lorentzian cannot meet the low crosstalk requirements of dense WDM. The use of coupled mode theory simplifies the task by providing an analogy with standard handbook filter design.[32]

29 T. Li and M.C. Teich, *Electron. Lett.* 27: 698 (1991); P. Diament and M.C. Teich, *IEEE J. Quan. Elec.* 28: 1325 (1992); T. Li and M.C. Teich, *IEEE J. Quan. Electron*. 29: 2568 (1993)

30 S. Fan, P.R. Villeneuve, J.D. Joannopoulos, and H.A. Haus, “Channel Drop Tunneling through Localized States,” 80(5): 960-63 (1998); S. Fan, P.R. Villeneuve, J.D. Joannopoulos, M.J. Khan, C. Manolatou, and H.A. Haus, “Theoretical Analysis of Channel Drop Tunneling Processes,” *Phys. Rev B.,* forthcoming.

31 C. Manolatou, M.J. Khan, S. Fan, P.R. Villeneuve, H.A. Haus, and J.D. Joannopoulos, “Coupling of Modes Analysis of Resonant Channel Add/Drop Filters,” *IEEE J. Quant. Electron.,* forthcoming.

32 M.J. Khan, C. Manolatou, S. Fan, P.R. Villeneuve, H.A. Haus, and J.D. Joannopoulos, “Coupling of Modes Analysis of Multipole Symmetric Resonant Channel Add/Drop Filters,” submitted to *IEEE J.Quant. Electron*.

The design of composite structures of a few microns in dimension allows a large scale integration of optical components. To accomplish such integration, it is necessary that complex interconnections of the different optical components be performed with low loss and negligible reflection and crosstalk. Waveguide bends and crossings with excellent performance characteristics have been demonstrated numerically using photonic crystals[33] and more recently using high-index contrast waveguides and resonators.[34] The idea is based on the fact that a lossless resonator with two ports and appropriate symmetry allows complete reflectionless transmission on resonance. In practice there is always some radiation loss from the resonator which must be counteracted by strong coupling to the waveguide mode. This lowers the external Q of the resonator leading to a very broad bandwidth.

We applied this concept in 2-D FDTD simulations of high-index contrast waveguide components (contrast of 3.2:1). By modifying the corner of a right angle bend into a resonant structure with symmetry, we were able to achieve over 98% transmission with negligible reflection over a bandwidth of more than 100 nm. Figure 15a shows the electric field pattern in the modified bend. A strongly coupled pair of similar structures was used in a T-splitter to achieve transmission over 49% in each arm. Finally, we looked at planar waveguide crossings. The waveguide intersection region was designed as a cavity supporting two orthogonal modes with a nodal plane along one of the two waveguide axes. Excitation of one mode from the input waveguide results in full transmission with no crosstalk into the intersecting waveguide. In Figure 15b we show the electric field amplitude calculated by 2-D FDTD in a planar waveguide crossing where the cavity is formed at the intersection by making cuts at the waveguides. It turns out that these cuts affect the performance in the same way as matching stubs in microwave resonator design.

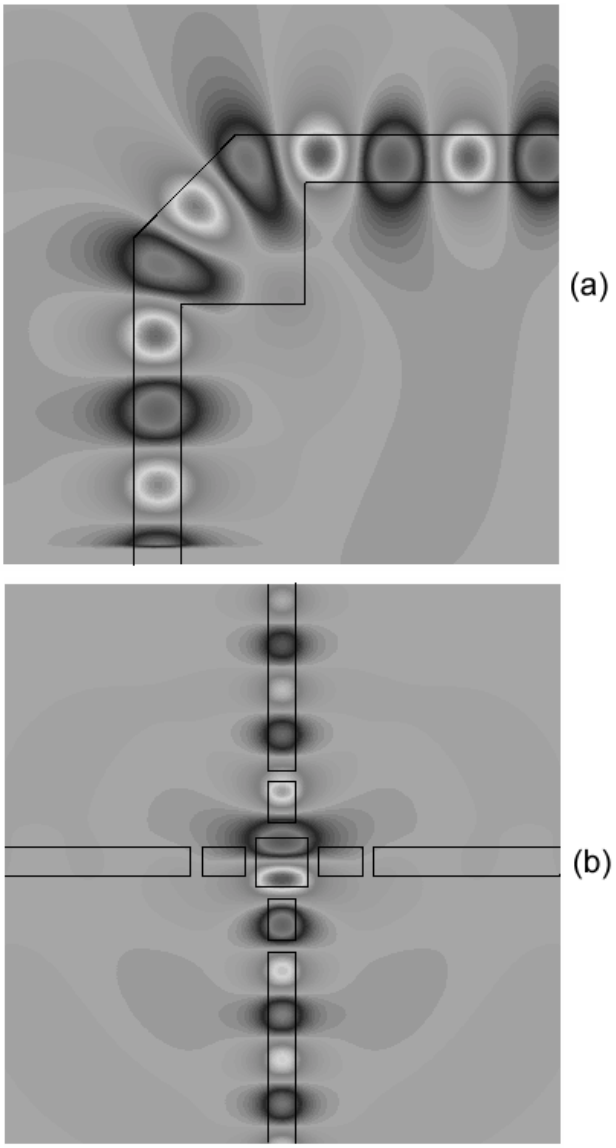

Figure 15. (a) Numerical simulation of the instantaneous electric field pattern in a low loss right angle dielectric waveguide bend. (b) Two dielectric waveguides which cross through one another with low scattering loss.

33 A. Mekkis, J.C. Chen, I. Kurland, S. Fan, P.R. Villeneuve, and J.D. Joannopoulos, "High Transmission through Sharp Bends in Photonic Crystal Waveguides," *Phys. Rev. Lett*. 77(18): 3787-90, (1996); S.G. Johnson, C. Manolatou, S. Fan, P.R. Villeneuve, J.D. Joannopoulos, and H.A. Haus, "Elimination of Crosstalk in Waveguide Intersections," *Opt. Lett*., forthcoming.

34 C. Manolatou, S.G. Johnson, S. Fan, P.R. Villeneuve, H.A. Haus, and J.D. Joannopoulos, "High Density Integrated Optics," *J. Lightwave Tech*., forthcoming.

1.12 Ring Resonators

Sponsors

Kanagawa (Japan) Academy of Science and Technology

U.S. Air Force - Office of Scientific Research
Grant F49620-98-1-0139

University of Maryland - Laboratory for Physical Sciences
Contract MDA 90497C0476

Project Staff

Dr. Brent E. Little, Professor Hermann A. Haus, Juha-Pekka J.V. Laine, Dr. S.T. Chu, Professor Lionel C. Kimerling, Professor Erich P. Ippen, Daniel J. Ripin

Ring resonators are the building blocks for very large-scale-integrated photonic circuits (VLSI-PC). The objective of VLSI-PC technology is analogous to that of microelectronics: to provide general optical signal processing functionality with high-density integration. Resonators provide the basis for general signal processing functionality by serving as channel dropping filters,[35] notch filters,[36] phase filters, switches and modulators,[37] polarization rotators, and optical taps, to name a few uses. Ring resonators that are either air-clad or fabricated using other high-index contrast dielectrics suffer negligible bending loss when made as small as a few wavelengths in radius. Rings with radii of 10 μm, for instance, can have integration densities larger than 10^5 devices/cm^2.

Micro-ring resonator channel dropping filters have been investigated experimentally. In one implementation, the ring and bus waveguides were coupled laterally.[38] Lateral coupling requires etching narrow gaps, 0.1 μm to 0.2 μm wide, to separate the bus and ring waveguides. The performance of ring resonator filters depends critically on the dimensions and quality of these gaps, features that can deviate significantly in the fabrication process. Coupling between the ring and bus can be controlled to greater accuracy by fabricating them on top of each other. The thickness of the dielectric buffer layer vertically separating the bus and ring is determined by material deposition. Deposition is a process that can achieve nearly monolayer resolution. An additional benefit of vertical coupling is that, with the waveguides positioned directly below the ring, the coupling strength is stationary and therefore insensitive to lateral misalignments. Figure 16a shows a glass ring integrated vertically over a pair of crossing waveguides.[39] The response at the drop port (labeled) is depicted in Figure 16b. Note that the shapes of the resonances correspond to ideal Lorentzians.

1.12.1 Journal Articles

Little, B.E., H.A. Haus, J.S. Foresi, L.C. Kimerling, E.P. Ippen, and R.J. Ripin. “Wavelength Switching and Routing using Absorption and Resonance.” *IEEE Phot. Tech. Lett.* 10: 816-18 (1998).

Little, B.E., S.T. Chu, and H.A. Haus. “Second Order Filtering and Sensing using Partially Coupled Travelling Waves in a Single Resonator.” *Optics Lett.* 23: 1570-72 (1998).

Little, B.E., J. Foresi, H.A. Haus, E.P. Ippen, W. Greene, and S.T. Chu. “Ultra-compact Si/SiO_2 Micro-ring Resonator Channel Dropping Filter.” *IEEE Phot. Tech. Lett.* 10: 549-51 (1998).

35 B.E. Little, S.T. Chu, H.A. Haus, J. Foresi, and J.P. Laine, “Micro-ring Resonator Channel Dropping Filters,” *IEEE J. Lightwave Tech*. 15: 998-1005 (1997).

36 B.E. Little, H.A. Haus, J.S. Foresi, L.C. Kimerling, E.P. Ippen, and R.J. Ripin, “Wavelength Switching and Routing using Absorption and Resonance,” *IEEE Phot. Tech. Lett.* 10: 816-18 (1998).

37 B.E. Little, S.T. Chu, and H.A. Haus, “Second Order Filtering and Sensing using Partially Coupled Travelling Waves in a Single Resonator,” *Opt. Lett.* 23: 1570-72 (1998).

38 B.E. Little, J. Foresi, H.A. Haus, E.P. Ippen, W. Greene, and S.T. Chu, “Ultra-compact Si/SiO_2 Micro-ring Resonator Channel Dropping Filter,” *IEEE Phot. Tech. Lett.* 10: 549-51 (1998).

39 B.E. Little, S.T. Chu, W. Pan, D. Ripin, T. Kaneko, Y. Kokubun, and E.P. Ippen, “Vertically Coupled Glass Microring Resonator Channel Dropping Filters,” *IEEE Phot. Tech. Lett.* 11: 215-17 (1999).

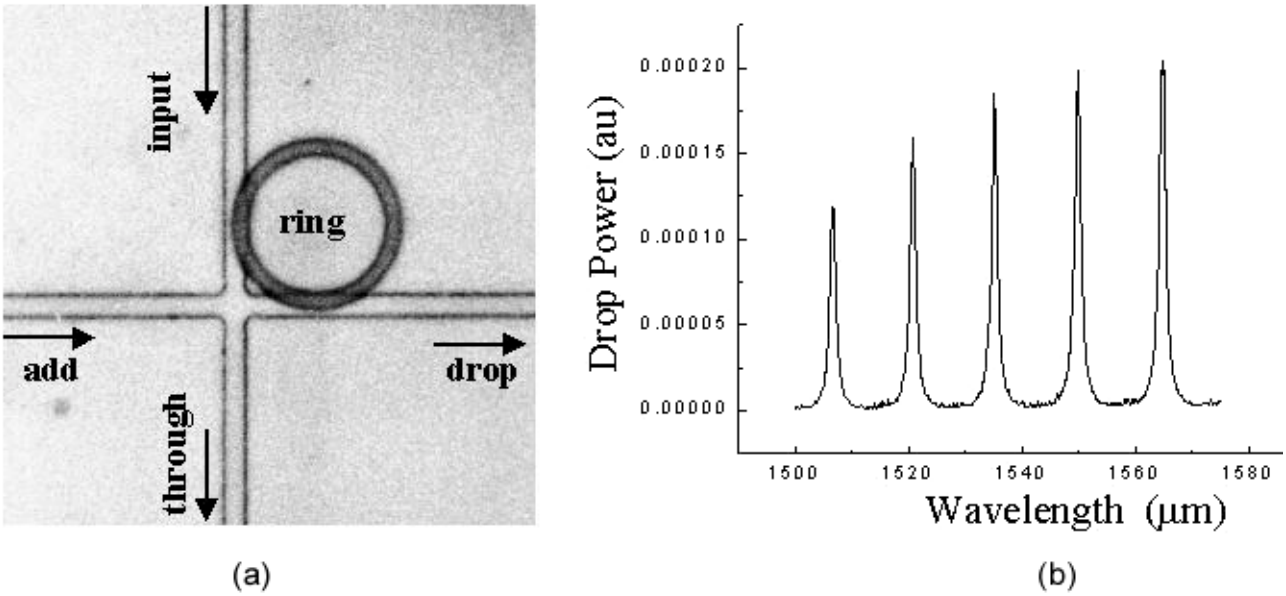

Figure 16. (a) A high quality glass microring resonator channel dropping filter for optical communications. The ring radius is 10 μm in radius. (b) Wavelength response at the drop port.

1.13 Microsphere Resonators

Sponsor

Charles S. Draper Laboratory
Contract DL-H-513222

Project Staff

Dr. Brent E. Little, Juha-Pekka J.V. Laine, Professor Hermann A. Haus

Microsphere resonators made of glass possess extremely high Q values. These Q's make them ideal candidates for high-resolution sensors: changes in their environment change their Q or their resonant frequency with a resolving power proportional to Q. These changes are monitored by an optical signal probe in a waveguide side-coupled to the resonator. A signal interacting with a sphere is delayed. The delay results in a phase shift that can be sensed in an interferometer.[40] In a different application, the clockwise circulating wave in a sphere can be coupled to the degenerate counter-clockwise component by a metallic probe placed near the sphere surface. A signal in the sphere makes a large number of revolutions, and the net external reflectivity is therefore a cumulative sum of all the naturally phase-matched individual reflections that are due to the metallic probe. Changes in distance between the reflecting probe and sphere, which might arise due changes in velocity, acceleration, or perhaps gravity waves, can be significantly amplified by this process.[41] Part of this work is supported by a grant from Draper Laboratory.

Microspheres with Q values of up to 10^7 are fabricated in our laboratory by melting the tip of an optical fiber using a fiber fusion splicer. Energy is coupled into the sphere by means of a side-coupled fiber. In order to access the evanescent field of the guided mode, the fiber is tapered to a narrow waist of approximately 5 m in diameter. Figure 17 shows a microsphere 500 m in diameter next to a tapered fiber. Note that the microsphere remains attached to the stem of the fiber used in its fabrication. Transmission dips are observed at the output of the tapered fiber, as depicted in the inset of Figure 17, when the wavelength passes through the resonance of the sphere.

40 B.E. Little, S.T. Chu, and H.A. Haus, "Track Changing by use of the Phase Response of Microspheres and Resonators," *Opt. Lett.* 23: 894-96 (1998).

41 B.E. Little, S.T. Chu, and H.A. Haus, "Second Order Filtering and Sensing using Partially Coupled Travelling Waves in a Single Resonator," *Opt. Lett*. 23: 1570-72 (1998).

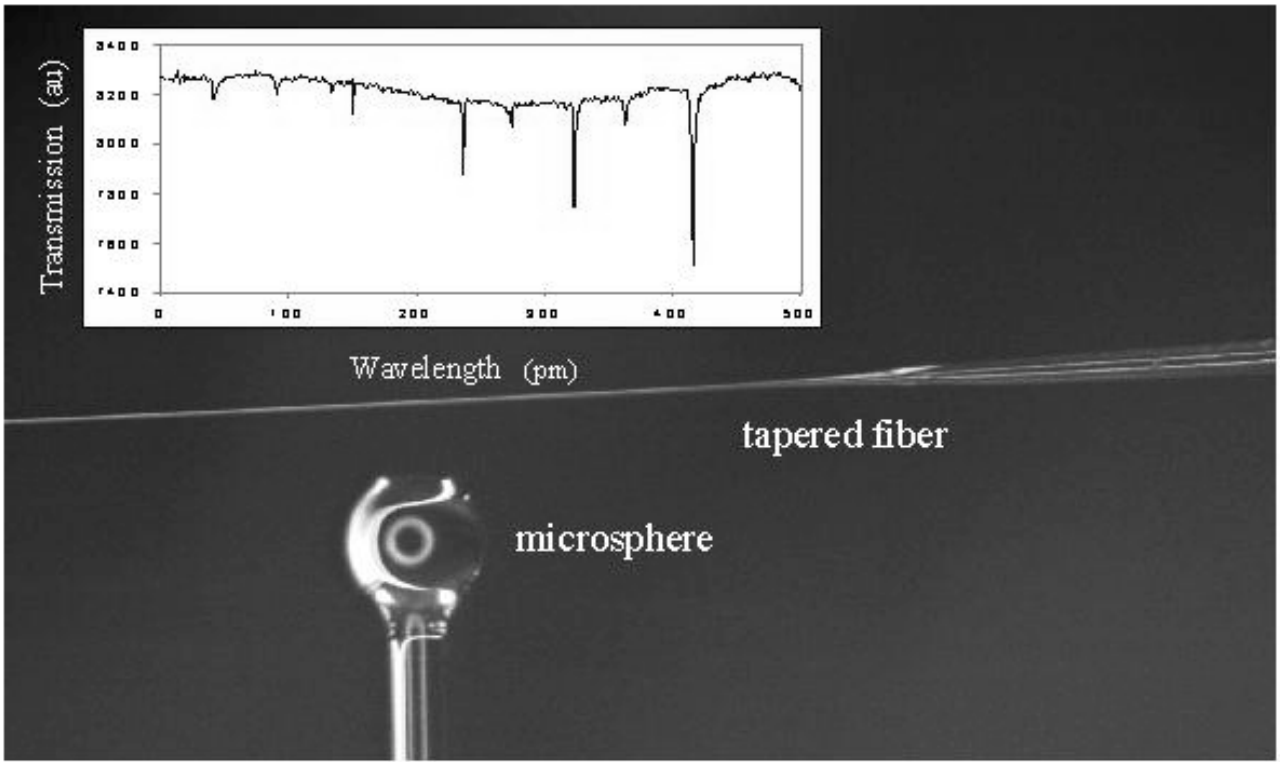

Figure 17. Ultra high Q microsphere resonator side coupled to a tapered fiber. The sphere radius is approximately 100 mm and has a Q of about 10^6. The inset shows the transmission response at the nd of the fiber.

1.13.1 Journal Article

Little, B.E., J.P. Laine, and H.A. Haus. “Analytic Theory of Coupling from Tapered Fibers and Half-blocks into Microsphere Resonators.” *IEEE J. Lightwave Tech.* Forthcoming.

1.14 Optical Measurements of Photonic Bandgap Resonators in the Near Infrared

Sponsors

Kanagawa (Japan) Academy of Science and Technology
National Science Foundation - Materials Research Science and Engineering Centers
Grant DMR-9808941
University of Maryland - Laboratory for Physical Sciences
Contract MDA 90497C047
U.S. Air Force - Office of Scientific Research
Grant F49620-98-1-0139

Project Staff

Daniel J. Ripin, Dr. Kuo-Yi Lim, Dr. Brent E. Little, Professor Erich P. Ippen, Professor John D. Joannopoulos, Professor Lionel C. Kimerling, Professor Leslie A. Kolodziejski, Dr. S.T. Chu

Photonic bandgap crystals (PBGs) are periodic lattices comprised of materials with very different dielectric constants. These crystals can be used for the basic manipulation and control of light, similar to the ways that electronic crystals manipulate electrons. With the addition of defects, photonic crystals can confine light to dimensions on the order of its wavelength. One-dimensional dielectric structures utilizing these unique properties have been designed to serve as optical microcavities. The basic design is an optical ridge waveguide with evenly spaced air holes. A defect in the spacing between two of the holes is introduced to create the high-Q cavity. Light on resonance with the cavity is transmitted, while all other wavelengths are reflected. Structures with this design have recently been fabricated in the GaAs/Al_xO_y material system,[42] building on work previously done in the Si/SiO_2 semiconductor material system.[43] Microcavities with resonances in the proper wave-

length range have the potential to be applied as channel dropping filters for WDM, components of integrated photonic chip devices, or as the cavities for a micron scale lasers.

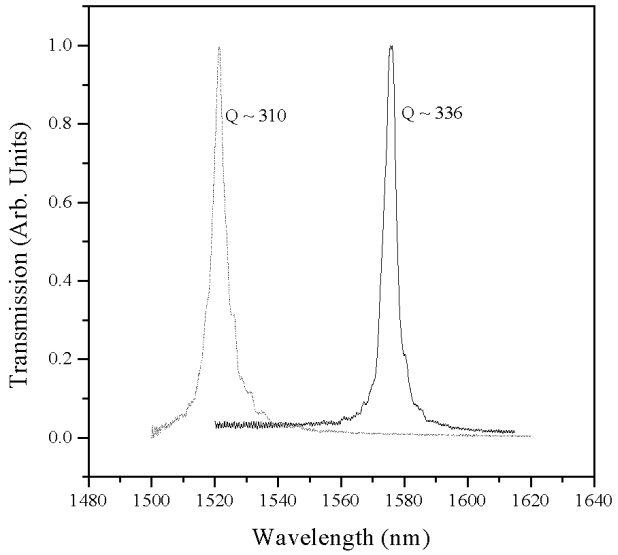

Figure 18. Measured transmission through two airbridge PBG waveguide microcavities. The long and short wavelength resonances correspond to microcavities with defect center-to-center lengths of 632 nm and 703 nm respectively.

We have characterized waveguide devices in two geometries: monorail and air-bridge. In the air-bridge geometry, the waveguide microcavity is suspended over air in order to achieve high optical confinement. In the monorail configuration, the waveguide is left resting on a lower index of refraction oxide layer. Optical resonances have been observed for the first time in an airbridge microcavity in the near IR, as well as in the monorail geometry. A cw tunable NaCl F-center laser was used for the transmission measurements. This laser is tunable from 1,510 nm to 1,680 nm, with an average output power of 250 mW. The light is coupled into small ridge waveguides with dimensions 0.2 x 0.5 μm using an optical fiber with a lensed output tip. Figure 18 shows the transmission measured through the PBG airbridge devices. The resonances from two different devices are shown. The resonance is observed to shift to longer wavelength with larger cavity dimensions. Resonances with Q's as high as 360 have been studied, and modal volumes as small as 0.025 m^3 have been calculated. By using structures with scaled hole dimensions, we were able to observe the band edges of the gap.

Using the same experimental setup, we have also continued our studies of ring resonators, a promising alternative to PBG devices for channel dropping filters. The ring resonator filter consists of two buried waveguides vertically-coupled to a high-index contrast circular ring waveguide. The resonators were manufactured in the silica compound-glass material system and measured.[44] The fabricated rings have radii ranging from 10 to 20 μm. Several resonances were observed near 1,550 nm with a quality factors up to 500 and free spectral ranges (FSR) approximately 25 nm.

New PBG based devices are now being studied in higher dimensional systems. In addition, experiments are being planned that will combine PBG technology with active semiconductor structures.

1.15 Femtosecond Studies of THz Acoustic Phonons in PbTe Quantum Dots

Sponsors

Joint Services Electronics Program
Grant DAAH04-95-1-0038
U.S. Air Force - Office of Scientific Research
Grant F49620-98-1-0139

Project Staff

Erik R. Thoen, Dr. Patrick Langlois, Dr. Günter Steinmeyer, Gaston E. Tudury, Juliet T. Gopinath, Dr. Markus Joschko, Professor Erich P. Ippen, Dr. C.L. Cesar[45]

Because of their strong quantum confinement, semiconductor quantum dots offer the potential of application as efficient nonlinear optical elements. Recently,

42 K.Y. Lim, D.J. Ripin, G.S. Petrich, L.A. Kolodziejski, E.P. Ippen, M. Mondol, H.I. Smith, P.R. Villeneuve, S. Fan, and J.D. Joannopoulos, *J. Vac. Sci. Technol. B*, forthcoming.

43 J.S. Foresi, P.R. Villeneuve, J. Ferrera, E.R. Thoen, G. Steinmeyer, S. Fan, J.D. Joannopoulos, L.C. Kimerling, H.I. Smith, and E.P. Ippen, "Photonic-Bandgap Microcavities in Optical Waveguides," *Nature* 390: 143 (1997).

44 B.E. Little, S.T. Chu, W. Pan, D.J. Ripin, T. Kaneko, Y. Kokubun, and E.P. Ippen, "Vertically Coupled Glass Microring Resonator Channel Dropping filters," *P. T. L.* 215: 11 (1999).

45 Instituto de Física, Universidade Estadual de Campinas, Campinas-SP, Brazil.

their use for saturable absorber modelocking has been successfully demonstrated. Previous work on the nonlinear response of quantum dots has been mainly concentrated on Cadmium-compound nanocrystals, which exhibit strong nonlinearities in the visible spectrum. The lower bandgap of lead compounds provides the opportunity to produce quantum dots absorbing in the wavelength range from 1 to 2 μm, so they can be tailored to the gain spectra of virtually all solid state lasers in that range. Also, with their large bulk exciton Bohr radius, they allow strong quantum confinement with relatively large nanocrystals.

We are investigating the nonlinear transmission characteristics of PbTe quantum dot glasses with a high-sensitivity heterodyne pump-probe experiment. A femtosecond optical parametric oscillator system producing pulses of 130 fs, tunable from 1.4 to 1.6 μm, was used in these experiments. The nonlinear response of a quantum dot sample with an exciton peak at 1365 nm excited with 1580 nm pump beam is shown in Figure 19. It exhibits three components, a slow exponential decay with a response time of 175 ps, a fast response with a time constant in the range of 100 fs, and an oscillatory component with a frequency of 0.5 THz and damping time of about 2.0 ps. The frequency of these oscillations is clearly a signature of acoustic vibrations. To our knowledge, this is the first time that coherent acoustic phonons have been observed from quantum dots in a glass matrix.

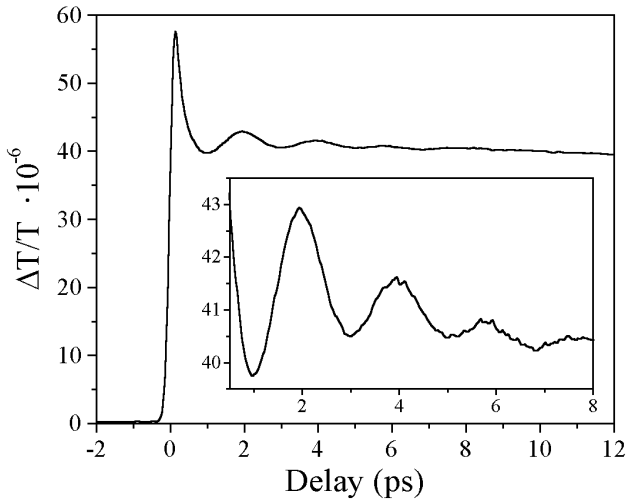

Figure 19. Transmission of the probe at 1580 nm as a function of time through PbTe quantum dots in a glass matrix. The oscillations result from excitation of the spheroidal acoustic mode of the quantum dots.

When acoustic modes are excited, the radius of the quantum dot oscillates at the sphere's eigenfrequencies altering the quantum confinement and shifting the exciton peak of the absorption. For a probe pulse at a wavelength on the slope of the excitonic peak, this shifting changes the probe transmission. We have developed an acoustic continuum model to calculate the resonant frequencies and damping times of the quantum dot acoustic modes as a function of radius. Using the bulk velocity of sound in PbTe, we calculate a resonance frequency of 0.53 THz for the fundamental breathing mode of a 6 nm diameter unstrained quantum dot. This frequency agrees with what is observed experimentally.

We have measured the frequency and damping time of these oscillations as a function of the pump-probe wavelength, which determines size-selection. This allows for the characterization of the size distribution, dephasing, and other loss mechanisms in these quantum dot glasses. The oscillation frequencies were accurately modeled. The damping of the oscillation as a function of wavelength was compared to the result of the acoustic continuum model. The model accounts for the radiative loss at the interface of the dots and yields values for the damping time near 2 ps. This suggests that the dominant damping mechanism is radiative transfer of energy out of the dots to the surrounding glass matrix.

1.15.1 Publication

Thoen, E.R., G. Steinmeyer, P. Langlois, E.P. Ippen, G.E. Tudury, C.H. Brito Cruz, L.C. Barbosa, and C.L. Cesar. "Coherent Acoustic Phonons in PbTe Quantum Dots." *Appl. Phys. Lett.* 73: 2149 (1998).

1.16 Nonlinear Optical Autocorrelation Based on Three-Photon Absorption in a GaAsP Photodiode

Sponsors

Joint Services Electronics Program
Grant DAAH04-95-1-0038

U.S. Air Force - Office of Scientific Research
Grant F49620-98-1-0139

Project Staff

Dr. Patrick Langlois, Professor Erich P. Ippen

We have demonstrated three-photon-absorption (3PA) conductivity in a GaAsP photodiode and its use to achieve nonlinear optical autocorrelation of short pulses.[46] We have shown that this method is a reliable and valuable measure of pulse duration and allows for an estimate of the ratio of the two- and three-photon absorption coefficients.

The pulses are generated by an optical parametric oscillator (OPO) and have a typical pulsewidth of 150 fs, tunable from 1.4 to 1.6 μm. A standard Michelson-type setup with a speaker allows for real-time autocorrelation. The delayed optical pulses are focused to a 4 μm spot size on the photodiode. The GaAsP photodiode has a bandgap at ~680 nm. This defines a wavelength range from 1.38 μm to 2.07 μm where 2PA is not allowed and for which three-photon-absorption is expected to be the dominant absorption mechanism.

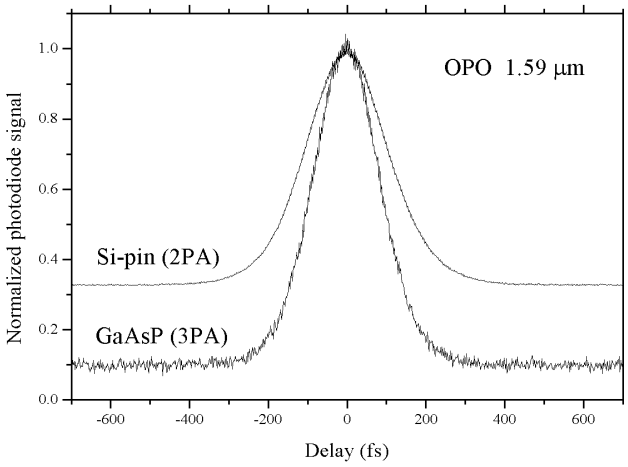

Figure 20. Transmission of the probe at 1580 nm as a function of time through PbTe quantum dots in a glass matrix. The oscillations result from excitation of the spheroidal acoustic mode of the quantum dots.

The 3PA intensity autocorrelation trace measured in a non-collinear geometry is shown in Figure 20. The 2PA trace obtained with a Si-pin photodiode in the same conditions is also plotted for comparison. For 3PA we achieve the theoretical peak to background ratio of 10 to 1. Intensity dependence measurements have also revealed that the photocurrent signal increases as the third power of the intensity, as expected from three-photon absorption. This conclusion is further supported by the value of the peak to background ratio of ~32 measured in the interferometric autocorrelation traces. In all cases the measured values are in excellent agreement with theoretical predictions. These results indicate that three-photon absorption is the dominant absorption mechanism in the GaAsP photodiode at this wavelength. Similar results were obtained from 1.4 to 1.6μm.

One extension to the 3PA autocorrelation measurement is to allow an estimate of the 3PA coefficient β_3 of the photodiode semiconductor material, provided that its 2PA coefficient β_2 is known. This can be done by comparing the measured photocurrent signals S generated by 2PA and 3PA in the same experimental conditions. For an n-photon absorption process, S is given by,

$$S_{nPA} \sim C\int (B_n I^n / n\hbar w) 2\pi r dr dt$$

where I is the optical intensity on the photodiode and C is a geometry factor assumed to be the same for both 2PA and 3PA. For the GaAsP photodiode used in our experiments, the ratio β^3/β^2 is measured to be ~5×10^{-3} cm^2/GW. This value is consistent with estimates based on scaling rules for multiphoton absorption in semiconductors.

1.17 Wavelength and Intensity Sampling of Optical Signals using Semiconductor Optical Amplifiers

Sponsor

Deutscher Akademischer Austauschdienst

Project Staff

Leaf A. Jiang, Professor Erich P. Ippen, Stefan Diez,[47] Carsten Schmidt,[47] Enno Hilliger,[47] Hans-Georg Weber[47]

We demonstrated and compared three measurement techniques using SOAs to directly obtain the intensity and wavelength profiles (chirp) of an unknown optical pulse with resolution of about 1 ps and without extensive computation. All three techniques used a synchronized short probe pulse to sample a broader signal pulse. The interaction between these pulses

46 P. Langlois and E.P. Ippen, "Three-Photon-Absorption Autocorrelation in a GaAsP Photodiode," Paper to be presented at the Conference On Lasers and Electro-Optics CLEO '99, Baltimore, Maryland, May 23-28, 1999, paper CFG5.

47 Heinrich-Hertz-Institut für Nachrichtentechnik, Einsteinufer 37, 10587 Berlin, Germany.

was mediated through different mechanisms, namely four-wave-mixing (FWM-technique), gain saturation (GS-technique), and interferometric switching (SLALOM-technique[48]). For a brief explanation of operation principles of the sampling techniques, refer to Figure 21. The techniques investigated here are similar in concept to a variety of other all-optical cross-correlation techniques using nonlinear crystals.[49] Signal and probe pulses were derived from different lasers and cross-correlation is based on nonlinear effects in an SOA. The output signals were observed in the 1.55 μm wavelength range by an optical spectrum analyzer (OSA). Wavelength and intensity of the cross-correlated signal can be accessed simultaneously as a function of the signal-probe delay. Due to amplification in the SOA, it was possible to investigate signal pulses with peak powers as low as 9 mW.

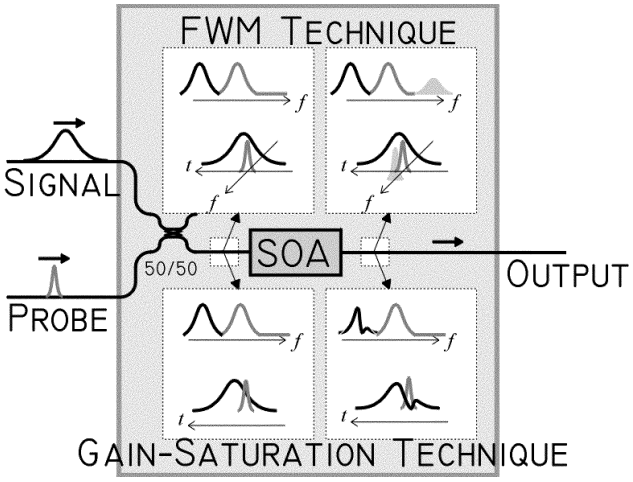

Figure 21. Experimental setup for FWM- and GS-techniques. The intensity and spectral profiles for the signal and probe pulses are shown (for one particular signal-probe delay) before and after the SOA. In the FWM-technique, an optical wave (related to the instantaneous signal amplitude and wavelength) is generated at a new optical frequency when a probe pulse temporally overlaps with parts of the signal. In the GS-technique the gain of the SOA is bleached by the short probe pulse. The part of the signal which falls into that instant is then missing at the SOA output, creating a spectral dip which is then tracked in wavelength and amplitude.

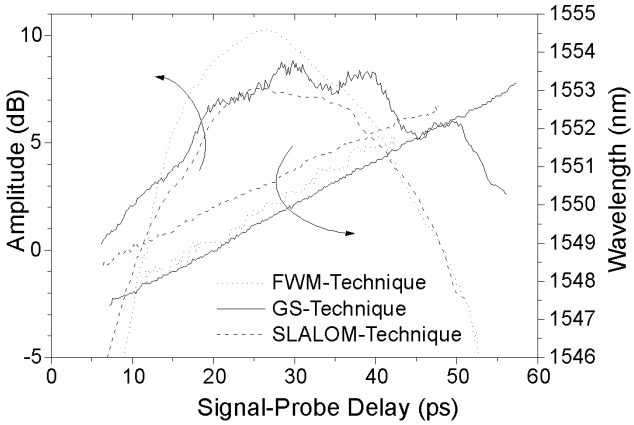

Figure 22. Comparison of the three techniques measuring a 21-ps linearly-chirped pulse.

The aforementioned techniques were used to sample the wavelength and intensity of 21-ps chirped pulses, which were created by propagating transform-limited 1-ps pulses at a 10 GHz repetition rate through 500 m of standard fiber (dispersion value of 17 ps/km nm). Figure 22 shows the resulting intensity and wavelength profiles. The dispersion of the fiber was calculated to be 17.15, 17.95, and 20.20 ps/nm/km (FWHM), and the 3-dB pulse-widths measured at 21.5, 26, and 23 ps, for the FWM-, GS-, and SLALOM-techniques, respectively. The GS technique produces the least reliable amplitude profile, because of its reliance on spectral saturation; but it provides an excellent measure of chirp. The SLALOM results are limited by the relatively large width of the SLALOM switching window (about 10 ps in our experiment).

Comparing the three methods, we find that the FWM-technique yields the most reliable data. The GS-technique offers the advantage of polarization independence and convenient setup. The lower limit of the time resolution of the presented measurement techniques is determined mainly by low frequency (<3 Hz) timing jitter. The standard deviations of the relative temporal displacement of probe and signal pulses for the FWM-, GS-, and SLALOM-techniques were estimated at 1.5, 0.72, and 0.5 ps, respectively.

48 M. Eiselt, W. Pieper, and H.G. Weber, "SLALOM: Semiconductor Laser Amplifier in a Loop Mirror," *J. Lightwave Tech*. 13: 2099-112 (1995).

49 E.P. Ippen and C.V. Shank, "Dynamic Spectroscopy and Subpicosecond Pulse Compression," *Appl. Phys. Lett.* 27: 488-90 (1975); K.W. DeLong, D.N. Fittinghoff, and R. Trebino, "Practical Issues in Ultrashort-Laser-Pulse Measurement Using Frequency-Resolved Optical Gating," IEEE Jour. Quan. Elec. 32: 1253-64 (1996); D.N. Fittinghoff, J.L. Bowie, J.N. Sweetser, R.T. Jennings, M.A. Krumbügel, K.W. DeLong, and R. Trebino, "Measurement of the Intensity and Phase of Ultraweak, Ultrashort Laser Pulses," Opt. Lett. 21: 884-6 (1996).

1.17.1 Publications

Diez, S., C. Schmidt, D. Hoffmann, C. Bornholdt, B. Satorius, H.G. Weber, L.A. Jiang, and A. Krotkus. "Simultaneous Sampling of Optical Pulse Intensities and Wavelengths by Four-Wave Mixing in a Semiconductor Optical Amplifier." *Appl. Phys. Lett*. 73(26): 382 (1998).

Jiang, L.A., E.P. Ippen, S. Diez, C. Schmidt, and H.G. Weber. "Wavelength and Intensity Sampling of Optical Signals using Semiconductor Optical Amplifiers." Paper to be presented at the Conference On Lasers and Electronic Optics CLEO '99, Baltimore, Maryland, May 23 - 28, 1999.

1.18 High-Repetition Rate Fiber Lasers with Low-Timing Jitter

Sponsors

Defense Advanced Research Projects Agency
Grant F49620-96-0126

MIT Lincoln Laboratory
Contract BX-6881

U.S. Air Force - Office of Scientific Research
Grant F49620-98-1-0139

Project Staff

Matthew E. Grein, Professor Erich P. Ippen, Professor Hermann A. Haus, Leaf A. Jiang

Low-noise lasers with minimum pulse-to-pulse timing jitter are of interest for numerous applications, including high-speed optical communications and precision optical sampling. Timing jitter smears out the certainty in the arrival time of the pulse and can lead to degradation of bit-error-rate in the former case and to loss of fidelity and dynamic range of the sampled data in the latter. Both applications require synchronization to an external, electronic clock, thus requiring that an active modelocker be employed via either amplitude (AM) or phase (PM) modulation. Building an actively modelocked laser with minimal timing jitter, in principle and in practice, requires an understanding of its dependence on the laser parameters, including group-velocity dispersion (GVD), effects of amplitude and phase modulation depth, and strength of filtering.

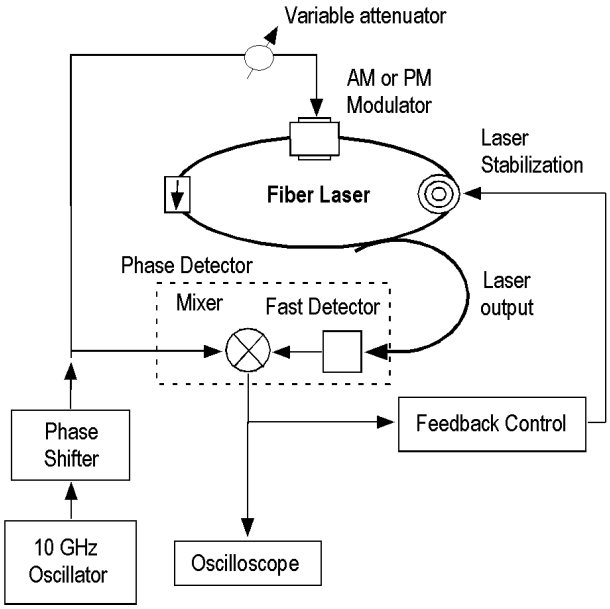

Figure 23. Setup for measuring pulse timing relaxation rates.

We have carried out experiments on the pulse retiming restoration dynamics of an actively modelocked fiber laser[50] for both AM and PM and compared the results with the predictions of the soliton perturbation theory. The setup in Figure 23 shows a fiber ring laser harmonically modelocked at 10 GHz and producing soliton pulses as short as 750 fs. The modelocker is a traveling wave $LiNbO_3$ modulator that can be set to operate in either AM or PM mode, depending on the external electronic biasing scheme. A laser stabilization scheme employing a fiber-wound piezoelectric drum corrects for laser cavity drift from the modelocking frequency. The measurement of the laser recovery time is achieved by electronically mixing the detected output of the laser with the modulation signal in an RF phase detector, whose output is a voltage proportional to the phase difference between the laser pulses and the modulation signal. Switching the phase shifter from one phase state to the next displaces the timing of the pulses with respect to the modulation signal. A typical trace, for the PM case, with a phase displacement of $\pi/2$, is shown in Figure 24. Note that the 50 ns switching speed of the phase shifter is undetectable in the figure. For AM, theory predicts that τ_{relax} as a function of modulation depth, M, goes as $(M\tau^2)^{-1/2}$. For PM, the

50 M.E. Grein, L.A. Jiang, H.A. Haus, and E.P. Ippen, "A Study of Timing Restoration Dynamics in an Actively Modelocked Soliton Laser," Conference on Lasers and Electrooptics, Baltimore, Maryland (1999).

dependence of τ_{relax} is more complicated. An important feature of the case for PM is a much weaker dependence of τ_{relax} on pulsewidth, compared with AM.

While we have found that the pulse restoration time for PM is decreased by the presence of GVD, it does not necessarily follow that the timing jitter can be made smaller just by increasing the GVD. This is because the Gordon-Haus effect—in which the ASE in the optical amplifier imposes a random walk on the carrier frequency, which translates to a random walk in the pulse timing—scales with GVD as well. We are currently studying whether there exists an optimum GVD leading to the minimum timing jitter for PM and comparing it to the minimum jitter for AM.

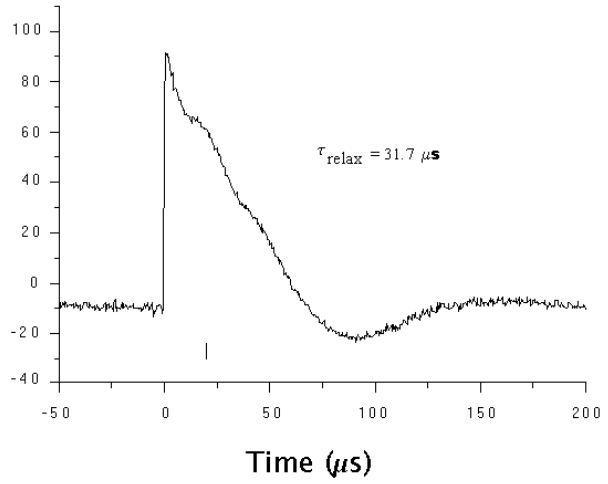

Figure 24. Example trace of pulse timing relaxation, shown here for phase modulation.

1.19 Ultrashort-Pulse Generation and Ultrafast Phenomena

Sponsors

Joint Services Electronics Program
Grant DAAH04-95-1-0038
U.S. Air Force - Office of Scientific Research
Contract F49620-95-1-0221
U.S. Navy - Office of Naval Research/MFEL
Contract N00014-94-1-0717

Project Staff

Igor P. Bilinsky, Seong-Ho Cho, Rohit P. Prasankumar, Dr. Franz X. Kärtner, Dr. Uwe Morgner, Dr. James N. Walpole,[51] Leo J. Missaggia,[51] Professor Erich P. Ippen, Professor Victor P. Mikhailov,[52] Professor James G. Fujimoto

1.19.1 Novel Modelocked Laser Cavity Designs for High Peak Intensities

Ultrashort-pulse laser sources are a critical technology for advances in signal processing, high speed communications, and the investigation of ultrafast nonlinear process in semiconductor materials and devices. Generally, these laser sources must be technologically simple, robust, and cost effective. In the last several years, significant advances have been made in the development of Kerr lens modelocking (KLM) utilizing electronic Kerr effect fast saturable absorber action. KLM has allowed generation of pulses of less than two optics cycles, the shortest ever produced directly from a laser oscillator.[53] Working in collaboration with Professors Erich P. Ippen and Hermann A. Haus, we have developed a theoretical model which provides a foundation for understanding and optimizing short-pulse KLM lasers.[54] Our program investigates several areas of ultrafast laser technology, with the objective of developing broadly applicable new technologies which can be applied across a range of laser materials and systems.

KLM lasers can generate short pulses and high output powers; however, they have the disadvantage that the pulse repetition rates are extremely high, and therefore average powers for a given pulse intensity or energy are quite high. The reduction of pulse repetition rate from the hundred MHz range to the range of a few MHz is a significant advantage for nonlinear and ultrafast studies because it reduces thermal parasitics, sample damage problems, and recovery time artifacts. Generation of femtosecond pulses with high

51 MIT Lincoln Laboratories, Lexington, Massachusetts.

52 Professor, International Laser Center, Polytechnical Academy, Minsk, Belarus.

53 U. Morgner, F.X. Kärtner, S.H. Cho, Y. Chen, H.A. Haus, J.G. Fujimoto, E.P. Ippen, V. Scheurer, G. Angelow, and T. Tschudi, "Sub-Two Cycle Pulses from a Kerr-Lens Modelocked Ti:sapphire Laser," *Opt. Lett.* 24: 411-13 (1999).

54 H.A. Haus, J.C. Fujimoto, and E.P. Ippen, "Structures for Additive Pulse Modelocking," *J. Opt. Soc. Am. B* 8:2068 (1991); H.A. Haus, J.G. Fujimoto, and E.P. Ippen, "Analytic Theory of Additive Pulse and Kerr Lens Mode Locking," *IEEE J. Quant. Electron.* 28: 2086 (1992).

intensities in the MW range is essential for a number of applications including optical harmonic generation and investigation of ultrafast nonlinear optical phenomena. The peak power directly generated by modelocked Ti:Al_2O_3 laser sources is in the range of hundreds of kW which is often insufficient for studies of nonlinear phenomena. Our group has recently demonstrated the use of cavity dumping to increase output pulse peak power from a KLM Ti:Al_2O_3 laser.[55] Other investigators have also examined techniques to design standard repetition rate KLM lasers to operate at high power and achieve high-intensity pulses.[56] The development of low-cost, high-intensity laser sources will enable a wider range of femtosecond measurement applications, making this technology more available to both the research and development communities.

Our approach was to decrease the laser repetition rate and increase the laser output pulse energy by increasing cavity length. The pulse energy can also be increased by reducing the laser repetition rate while keeping the laser average output power constant. The development of long-cavity femtosecond lasers requires careful design because KLM depends on operation in a particular subset of the stability region for optimum modelocking performance. As an approach for obtaining low repetition rates and high peak power directly from a KLM Ti:Al_2O_3 laser, a Herriott style multiple-pass cavity (MPC)[57] was used as an optical delay line designed to produce a unity q parameter transformation. The unity q transformation of the delay line leaves the laser resonator mode and KLM behavior nearly invariant. Thus, if this device is inserted into the KLM laser, it increases the cavity length but leaves the laser cavity mode and nonlinear focusing behavior invariant.

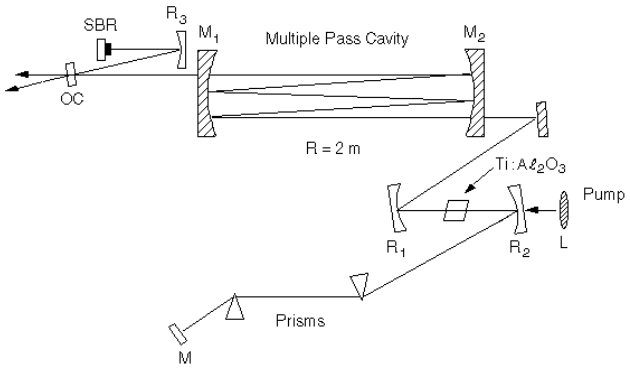

Figure 25. Schematic of low repetition rate Ti:Al_2O_3 laser. The long cavity is implemented using a pair of multiple pass cavity mirrors: M_1, M_2, 2 inch diameter MPC mirrors with R=2 m ROC; R_1, R_2, 10 cm ROC mirrors; R_3, 20 cm ROC mirror; L, 12.5 cm focal length pump beam focusing lens; OC, 3.5% ½ inch thick, flat output coupler; prisms, Brewster-cut fused-silica prisms.

Following this approach, we designed a high-peak power laser using a standard, dispersion compensated KLM Ti:Al_2O_3 resonator with an MPC incorporated into one of the arms. Operation at 15 MHz repetition rate was achieved using a design in which the beam made 20 round trips between the MPC mirrors separated by 82.4 cm.[58] Stable KLM modelocking was achieved resulting in 0.7 MW peak power and 16.5 fs nearly transform limited pulses. The interpulse arrival time was 68 ns. Lower repetition rates of 7.2 MHz laser were achieved using 24 round trips between the MPC mirrors separated by 148 cm (Figure 25).[59] We obtained 150 mW average output power in the two output beams and 23.5 fs nearly transform limited pulses centered at 823 nm (Figure 26). Alternately, the output coupler can be placed at the other end of the cavity to extract a single beam. The peak power in this case would be 0.9 MW.

55 M. Ramaswamy, M. Ulman, J. Paye, and J.G. Fujimoto, "Cavity-dumped Femtosecond Kerr-lens Mode-locked Ti:Al_2O_3 Laser," *Opt. Lett.* 18: 1822-24 (1993).

56 L. Xu, G. Tempea, A. Poppe, M. Lenzner, C. Spielmann, F. Krausz, A. Stingl, and K. Ferencz, "High-power Sub-10-fs Ti:sapphire Oscillators," *Appl. Phys. B* 65: 151-59 (1997).

57 D. Herriott, H. Kogelnik, and R. Kompfner, "Off-Axis Paths in Spherical Mirror Interferometers," *Appl. Opt.* 3: 523-26 (1964); B. Perry. R.O. Brickman, A. Stein, E.B. Treacy, and P. Rabinowitz, "Controllable Pulse Compression in a Multiple-pass Raman Laser," *Opt. Lett.* 5: 288 (1980).

58 S.H. Cho, B.E. Bouma, E.P. Ippen, and J.G. Fujimoto, "A 15 MHz High Peak Power KLM Ti:Al_2O_3 Laser using Multiple Pass Long Cavity," paper presented at the Conference on Lasers and Electro-Optics, San Francisco, California, May 22-28, 1998; S.H. Cho, B.E. Bouma, E.P. Ippen, and J.G. Fujimoto, "Low-Repetition Rate and High-Peak-Power Kerr-Lens Modelocked Ti:Al_2O_3 Laser with a Multiple-Pass Cavity," *Opt. Lett.* 24: 417-19 (1999).

59 S.H. Cho, U. Morgner, F.X. Kärtner, E.P. Ippen, J.G. Fujimoto, J.E. Cunningham and W.H. Knox, "A 7.2 MHz High Power KLM Ti:Al_2O_3 Laser using a Multiple Pass Long Cavity and Saturable Bragg Reflector," paper to be presented at the 1999 Conference on Lasers and Electro-Optics, Baltimore, Maryland, May 22-28, 1999.

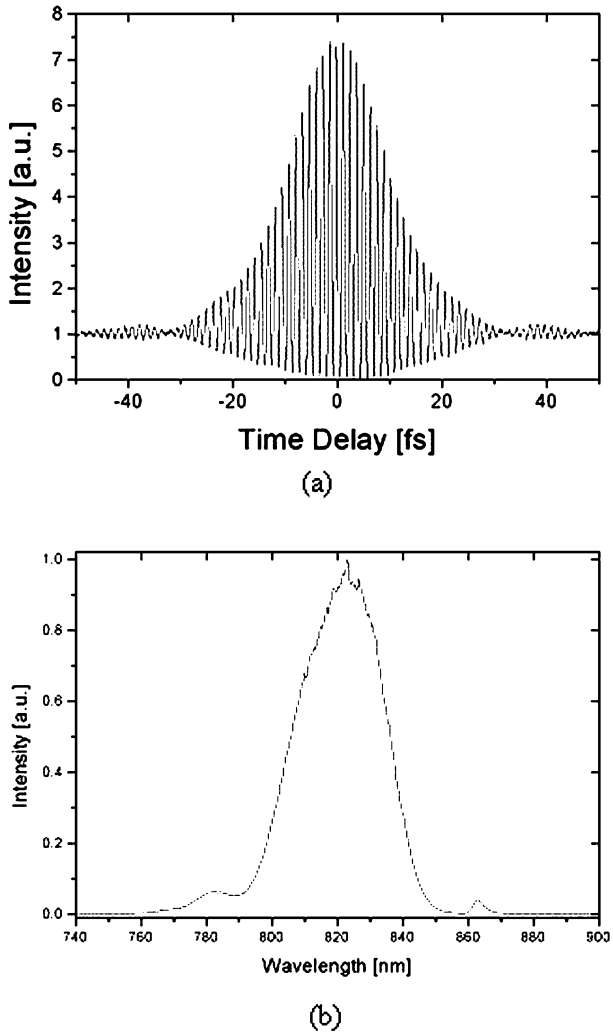

Figure 26. (a) Collinear interference autocorrelation trace of 23.5 fs pulse and (b) associated spectrum of 31 nm FWHM bandwidth from a KLM Ti:Al_2O_3 laser pulse.

The starting behavior of KLM and the stable KLM region of the long resonator laser changes slightly from the standard 100 MHz laser even though a unity q transformation is achieved by changing the separation d (Figure 25). This can be explained by the strong self-phase modulation (SPM) and self-focusing effects resulting from high intensity pulses. To increase peak power or reduce pulse duration without generating multiple pulse instabilities, we adjusted the cavity alignment to reduce the saturation of self-amplitude modulation (SAM) by optimizing the position of gain medium. This necessitates laser operation in a regime with a lower KLM, making the modelocking difficult to start. To stabilize the laser against multipulse formation and assist starting, a saturable Bragg reflector (SBR) is incorporated in the cavity at 7.2 MHz laser (Figure 25). The structure of a SBR consists of an AlAs/$Al_{0.85}Ga_{0.15}As$ quarter-wave dielectric stack grown by molecular beam epitaxy and a single GaAs quantum well.[60] Modelocking is initiated by slightly moving the focal point of the curved mirror R_3 onto the SBR. These studies are being performed in collaboration with Dr. Wayne Knox from Lucent Technologies.

1.19.2 Novel Saturable Absorber Devices Using Semiconductor Doped Glasses

The most common method of short-pulse generation is Kerr lens modelocking (KLM). Although KLM is a powerful technique which has been applied to a wide range of solid-state lasers, it has the disadvantages that it is hard to align, not self-starting, and sensitive to external perturbations. Recently, semiconductor saturable absorbers devices have been developed and demonstrated to address these problems.[61]

Semiconductor saturable absorbers are devices which produce saturable absorber behavior and passive modelocking. They can be used either independently or together with KLM and provide several advantages over KLM, including self-starting operation, simplicity in laser cavity design, and decoupling of the gain and modelocking mechanisms.

The most common saturable absorber technologies are semiconductor saturable absorber mirrors SESAM[62] and saturable Bragg reflectors SBR,[63] which have been used for both saturable absorber modelocking and initiation of KLM. However, these devices require epitaxial growth, which imposes lat-

60 S. Tsuda, W.H. Knox, S.T. Cundiff, W.Y. Jan, and J.E. Cunningham, "Mode-Locking of Ultrafast Solid-State Lasers with Saturable Bragg Reflectors," *IEEE J. Select. Top. Quantum Electron*. 2: 454-64 (1996).

61 U. Keller, D.A.B. Miller, G.D. Boyd, T.H. Chiu, J.F. Ferguson, and M.T. Asom, "Solid-State Low-Loss Intracavity Saturable Absorber for Nd:YLF lasers: An Antiresonant Semiconductor Fabry-Perot Saturable Absorber," *Opt. Lett.* 17: 505-07 (1992).

62 U. Keller, K.J. Weingarten, F.X. Kärtner, D. Kopf, B. Braun, I.D. Jung, R. Fluck, C. Hönninger, N. Matuschek, and J.Aus der Au, "Semiconductor Saturable Absorber Mirrors (SESAM's) for Femtosecond to Nanosecond Pulse Generation in Solid-State Lasers," *IEEE J. Select. Top. Quantum Electron.* 2: 435-53 (1996).

63 S. Tsuda, W.H. Knox, S.T. Cundiff, W.Y. Jan, and J.E. Cunningham, "Mode-Locking of Ultrafast Solid-State Lasers with Saturable Bragg Reflectors," *IEEE J. Select. Top. Quantum Electron.* 2: 454-64 (1996).

tice-matching constraints on the absorber materials and also requires complex and expensive systems for sample fabrication.

We have recently demonstrated the use of semiconductor doped glasses, some of which are available as commercial colored glass filters, as saturable absorbers for short-pulse generation.[64] We designed and fabricated a wedge-shaped structure allowing a thin, variable glass thickness to be inserted into the laser cavity. Using this device, we obtained self-starting saturable absorber modelocked operation with pulse durations of 1.9 ps from a Ti:Al_2O_3 laser. We also optimized the resonator for KLM and obtained saturable absorber assisted KLM, with self starting 52 fs pulses.

In the past year, we have investigated the absorption saturation dynamics of these devices with a series of pump-probe experiments. We observed photodarkening effects where the carrier relaxation times became faster with increasing exposure to laser radiation. This effect is usually attributed to photoexcited electrons trapped in the glass matrix and to modification of traps and recombination centers of the surface of nanoparticles due to impurities in the host glass matrix.

We performed a series of pump-probe experiments to characterize the influence of photodarkening on the absorption saturation dynamics. This was done by acquiring a pump-probe trace and then exposing the samples to a pump beam of higher power than that used during the measurement, with exposure times of 1, 2, 4, 8, 16, and sometimes 32 minutes. The pump power was then reduced and another pump-probe trace was acquired. This process was repeated until the changes in relaxation dynamics became negligible.

We noticed significant decreases in the carrier relaxation times with increased exposure (Figure 27). The magnitude of absorption saturation did not change in the photodarkened samples, indicating that the absorption cross section remained the same. The average intensity absorbed during these experiments is comparable with the average intensity absorbed on the saturable absorber intracavity, which indicates that the photodarkening effect is important for understanding the saturable absorber performance of the semiconductor-doped glasses.

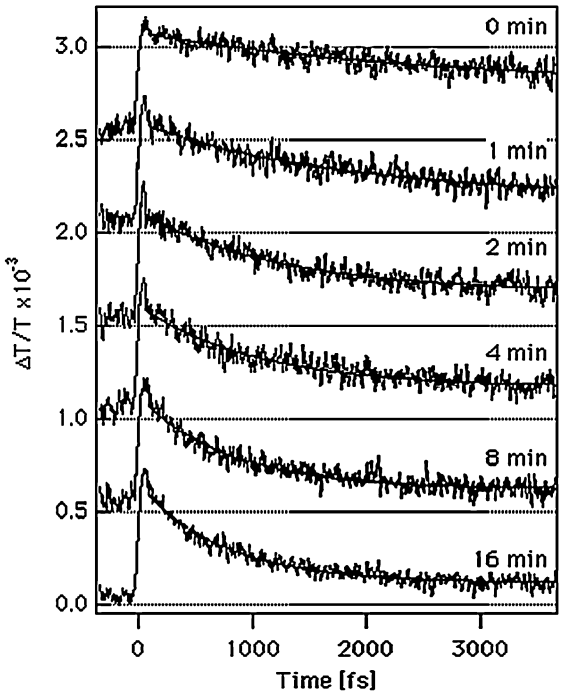

Figure 27. Pump-probe traces for semiconductor glass films exposed to 80 mW pump power for durations of 1, 2, 4, 8, and 16 minutes, demonstrating the photodarkening effect.

1.19.3 Development of Nonepitaxial Saturable Absorber Materials for Laser Modelocking Materials Growth and Characterization Laser Operation

Another attractive alternative to epitaxially grown saturable absorbers is the use of non-epitaxially grown semiconductor doped thin films as saturable absorber devices. One approach to fabricating these devices is by doping semiconductor nanocrystallites into silica films using RF sputtering.[65] RF sputtering is a simple and inexpensive technique; it also gives the user a great deal of control in fabricating saturable absorber devices.

64 I.P. Bilinsky, R.P. Prasankumar, and J.G.Fujimoto, "Self-starting Modelocking and KLM of a Ti:Al_2O_3 Laser Using Semiconductor Doped Glass Structures," *J. Opt. Soc. Am. B* 16: 546-49 (1999).

65 K. Tsunetomo, H. Nasu, H. Kitayama, A. Kawabuchi, Y. Osaka, and K. Takiyama, "Quantum Size Effect of Semiconductor Microcrystallites Doped in SiO_2-Glass Thin Films Prepared by RF-Sputtering," *Jap. J. Appl. Phys*. 28: 1928-33 (1989).

Semiconductor doped silica films have several attractive features. They can be deposited on virtually any substrate, including oxides such as glass and dielectric coatings as well as metal mirrors. By varying the doping density of the semiconductor quantum dots, one can adjust the absorption coefficient of the device. A wide range of semiconductor materials can be doped into the silica films. Therefore, appropriate choice of the semiconductor and knowledge of quantum confinement effects allow one to control the operating wavelength and absorption edge of the device.

Working in collaboration with Drs. James N. Walpole and Leo J. Missaggia at MIT Lincoln Laboratory, we are exploring approaches for fabricating, characterizing, and applying semiconductor films for ultrashort pulse laser generation. The films used in our experiments were fabricated using RF sputtering and consisted of InAs nanocrystallites doped into an SiO_2 matrix. The structural and optical properties of these films were comprehensively characterized with several techniques including transmission electron microscopy (TEM), x-ray photoemission spectroscopy (XPS), and energy dispersive x-ray spectroscopy (EDX). We found the films to contain a broad size distribution of InAs nanocrystallites up to ~80 Å, resulting in a smooth absorption edge at ~1.2 μm compared to 3.5 μm for bulk InAs. We used rapid thermal annealing (RTA) in nitrogen to modify the absorption saturation dynamics of the films; the results of pump-probe experiments at 800 nm are shown (Figure 28). Annealed films exhibited faster relaxation times and smaller saturation fluences than unannealed films, making them more suitable for laser modelocking.

The films used for Ti:Al_2O_3 laser modelocking were 300 Å thick, with absorption of ~2% per pass, and were deposited onto 3 mm thick sapphire substrates. The substrates were single crystal and 0-degree-oriented to avoid birefringence effects. The films were annealed at either 600 or 750° C for 60 seconds. The devices were used in a standard argon-pumped z-cavity Ti:Al_2O_3 laser (Figure 29) with an additional fold for focusing onto the absorber. The saturable absorber or a blank sapphire substrate (for KLM alignment) was positioned at the focus of the additional fold and oriented at Brewster angle. The laser spot size on the saturable absorber was estimated to be ~25 μm.

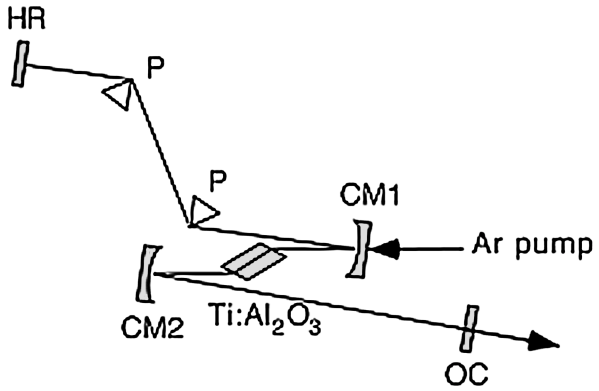

Figure 28. Pump-probe traces for annealed and as-grown InAs-doped silica films. The laser wavelength was 800 nm, pulse duration 30 fs, repetition rate 80 MHz. RTA in nitrogen was used to modify absorption saturation dynamics.

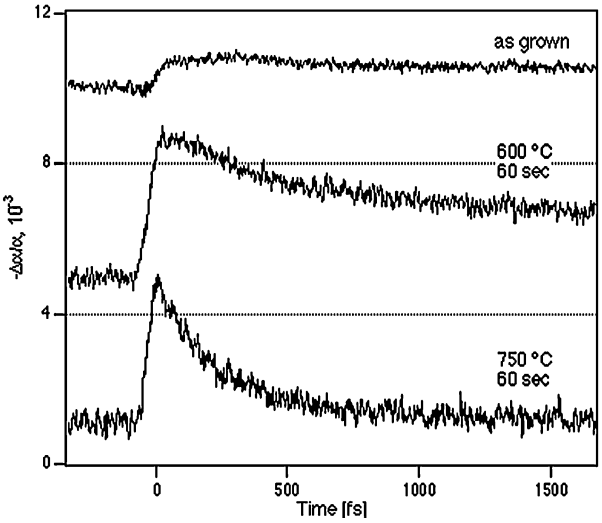

Figure 29. Schematic diagram of Ti:Al_2O_3 laser resonator. OC, 2% output coupler; SA, saturable absorber; M_1, 10 cm radius of curvature (ROC) mirrors; M_2, 7.5 cm ROC mirror; M_3, 5 cm ROC mirror.

With a saturable absorber in the cavity, self-starting saturable absorber assisted KLM was obtained, with pulses as short as 25 fs and a FWHM bandwidth of 53 nm, giving a time-bandwidth product of 0.59. SPM in the sapphire substrate may have prevented the pulses from being transform-limited. The laser wavelength was tunable from 800 to 880 nm while sustaining self-starting operation.

We are currently developing devices that combine the semiconductor doped silica films with metal and dielectric mirrors for use in a reflective geometry, making cavity designs more compact and flexible. We are also investigating extension of this technique to other laser materials, including Cr:forsterite (1.3 μm) and Cr:YAG (1.5 μm). In conclusion, we have developed nonepitaxially grown semiconductor saturable absorbers that, in conjunction with KLM, resulted in self-starting 25 fs pulses and a tuning range of 80 nm. These devices are a versatile and inexpensive alternative technology to epitaxially grown saturable absorbers and could therefore have a significant impact on ultrashort-pulse generation.

1.19.4 Publications

Journal Articles

Bilinsky, I.P., J.G. Fujimoto, J.N. Walpole, and L.J. Missaggia. "InAs-Doped Silica Films for Saturable Absorber Applications." *Opt. Lett.* 23:1766-68 (1998).

Bilinsky, I.P., J.G. Fujimoto, J.N. Walpole, and L.J. Missaggia. "Semiconductor-Doped-Silica Saturable Absorber Films for Solid State Laser Modelocking." *App. Phys. Lett.* 74 (1999).

Bilinsky, I.P., R.P. Prasankumar, and J.G. Fujimoto. "Self Starting Modelocking and KLM of a Ti:Al_2O_3 Laser using Semiconductor Doped Glass Structures." *J. Opt. Soc. Am. B.* 16: 546-49 (1999).

Chen, Y., F.X. Kärtner, U. Morgner, S.H. Cho, H.A. Haus, E.P. Ippen, and J.G. Fujimoto. "Dispersion Managed Mode-Locking." Submitted to *J. Opt. Soc. Am. B.*

Cho, S.H., B.E. Bouma, E.P. Ippen, and J.G. Fujimoto. "A Low-Repetition-Rate High-Peak-Power Kerr-Lens Modelocked Ti:Al_2O_3 Laser with a Multiple Pass Cavity." *Opt. Lett.* 24: 417-19 (1999).

Morgner, U., F.X. Kärtner, S.H. Cho, Y. Chen, H.A. Haus, J.G. Fujimoto, E.P. Ippen, V. Scheuer, G. Angelow, and T. Tschudi. "Sub Two-Cycle Pulses from a Kerr-Lens Modelocked Ti:sapphire Laser." *Opt. Lett*. 24: 411-13 (1999).

Meeting Papers Presented

Bilinsky, I.P., B.E. Bouma, and J.G. Fujimoto. "Self-Starting KLM Ti:Al_2O_3 Laser using Semiconductor Doped Glass Structures." Paper presented at the 1998 Conference on Lasers and Electro-Optics, San Francisco, California, May 2-8, 1998.

Cho, S.H., B.E. Bouma, E.P. Ippen, and J.G. Fujimoto. "A 15 MHz, 0.5 MW KLM Ti:Al_2O_3 Laser using Multiple Pass Cavity." Paper presented at the 1998 Conference on Lasers and Electro-Optics, San Francisco, California, May 2-8, 1998.

Book

Elsaesser, T.J., Fujimoto, D. Wiersma, and W. Zinth, eds. *Ultrafast Phenomena XI.* Springer Series in Chemical Physics. New York: Springer Verlag, 1998.

1.20 Laser Medicine and Medical Imaging

Sponsors

National Institutes of Health
Contract RO1-CA75289-01
Contract RO1-EY11289-13
Contract RO1-AR44812-01
Contract R29-HL55686-01

U.S. Air Force - Office of Scientific Research
Contract F49620-95-1-0221

U.S. Department of Commerce
Contract 70NANB6H0092

U.S. Navy - Office of Naval Research/Medical Free Electron Laser Program
Contract N000014-97-1-1066

Whittaker Foundation
Contract 96-0205

Project Staff

Stephen A. Boppart, Ravi K. Ghanta, Pei-Lin Hsing, Christine A. Jesser, Constantinos Pitris, Dr. Mark E. Brezinski,[66] Dr. Wolfgang Drexler, Dr. Xinge Li, Dr. Uwe Morgner, Dr. Joel Schuman,[67] Dr. Debra L. Stamper,[68] Professor James G. Fujimoto

66 Massachusetts General Hospital, Boston, Massachusetts, and Harvard Medical School, Boston, Massachusetts.

67 New England Eye Center and Tufts University School of Medicine, Boston, Massachusetts.

68 Department of Biology, Kings College, Wilkes-Barre, Pennsylvania.

1.20.1 Optical Coherence Tomography Technology

High-Resolution Cellular Level Optical Coherence Tomography

Optical coherence tomography (OCT) is a new high resolution imaging modality that was developed by our research group and collaborators in 1991.[69] OCT is analogous to ultrasound B-scan. It measures the echo time delay and the magnitude of backscattered light rather than acoustic waves using a technique known as low-coherence interferometry. The heart of an OCT system is a Michelson interferometer. It consists of two arms: one is the sample arm, and the other is the reference arm. The axial distance ranging or backscattering site localization within the sample is accomplished by varying the optical path length in the reference arm. The interferometric signal occurs only when the phase delay of the light collected from the sample is matched with the phase delay in the reference arm to within the coherence length of the source. A two-dimensional OCT image is built up with a series of such adjacent axial scans.

The longitudinal resolution of OCT is currently limited by the optical bandwidth of the light source, typically in a superluminescent diode, to ~10-15 μm. This resolution is insufficient to identify individual cells or to assess subcellular structures such as nuclei or mitotic figures. The ability to perform subcellular imaging with OCT could greatly enhance the detection of early neoplastic changes, thus improving both early cancer diagnosis and the imaging of developing biological morphology. Higher resolution OCT would also improve specificity of diagnosis for several ocular diseases, such as glaucoma, which require precise, detailed imaging and measurement of retinal nerve fiber layer thickness.

The first sub-10-μm-resolution was achieved by using broadband fluorescence from organic dye[70] and Ti:Al_2O_3 lasers.[71] No biological imaging could be performed with these light sources due to their low brightness. Recent development of femtosecond Kerr-lens modelocked solid-state lasers enabled the generation of low-coherence light with a single transverse mode and powers of more than 100 mW. These lasers have been used for in-vitro and in-vivo imaging with 3.7 μm and 6 μm longitudinal resolution.[72]

State-of-the-art KLM Ti:Al_2O_3 lasers using double chirped dispersion compensating mirrors can generate pulse durations of <7 fs and bandwidths of 200 nm or more at 800 nm center wavelength. An ultrahigh, subcellular level resolution, spectroscopic OCT system based on such a modelocked Ti:Al_2O_3 laser has been developed. *In vivo* imaging of developmental biology specimens as well as preliminary *in vivo* spectroscopic OCT could be achieved. It uses a Kerr-lens modelocked Ti:Al_2O_3 laser that emits pulses as short as 5.5 fs with bandwidths up to 350 nm centered at 800 nm with an average power of 150 mW. This high performance is achieved by using specially designed double chirped mirrors which have a high reflectivity bandwidth and controlled dispersion response in combination with low-dispersion prisms for intracavity dispersion compensation.[73] The OCT interferometer has been modified to accommodate the broad bandwidth of the Ti:Al_2O_3 laser. Appropriate single-mode fibers, a special broad bandwidth, wavelength flattened 3 dB fiber coupler, and special achromatic or catadioptric objectives must be used to maintain ultrabroad bandwidth and to achieve subcellular level resolution. Using dual balanced detection, the high-amplitude noise of the Ti:Al_2O_3 laser can be reduced and an S/N of nearly 110 dB can be achieved.

---

69 D. Huang, E.A. Swanson, C.P. Lin, J.S. Schuman, W.G. Stinson, W. Chang, M.R. Hee, T. Flotte, K. Gregory, C.A. Puliafito, and J.G. Fujimoto, *Sci.* 254: 1178-81 (1991).

70 H.H. Liu, P.H. Cheng, and J.Wang, "Spatially Coherent White Light Interferometer Based on a Point Fluorescent Source," *Opt. Lett.* 18: 678 (1993).

71 X. Clivaz, F. Marquis-Weible, and R.P. Salathe, "1.5 μm Resolution Optical Low Coherence Reflectometry in Biological Tissues," *Proc. Soc. Photo-Opt. Instrument. Eng.* 19: 2083 (1994).

72 B.E. Bouma, G.J. Tearney, S.A. Boppart, M.R. Hee, M.E. Brezinski, and J.G. Fujimoto, "High Resolution Optical Coherence Tomographic Imaging Using a Mode-Locked Ti:Al_2O_3 Laser Source," *Opt. Lett.* 20: 1486 (1995); B.E. Bouma, G.J. Tearney, I.P. Bilinsky, B. Glubovic, and J.G. Fujimoto, "Self Phase Modulated Kerr-Lens Mode Locked Cr:forsterite Laser Source for Optical Coherence Tomography," *Opt. Lett.* 21: 1839-41 (1996); S.A. Boppart, B.E. Bouma, C. Pitris, J.F. Southern, M.E. Brezinski, and J.G. Fujimoto, "*In Vivo* Cellular Optical Coherence Tomography," *Nat. Med.* 4 (7): 861-65 (1998).

73 U. Morgner, F.X. Kärtner, S.H. Cho, Y. Chen, H.A. Haus, J.G. Fujimoto, E.P. Ippen, V. Scheurer, G. Angelow, and T. Tschudi, "Sub-Two Cycle fs-Pulses from a Kerr-Lens Modelocked Ti:sapphire Laser," *Opt. Lett.,* forthcoming; F.X. Kärtner, N. Matuschek, T. Schibli, U. Keller, H.A. Haus, C. Heine, R. Morf, V. Scheuer, M. Tilsch, and T. Tschudi, "Design and Fabrication of Double-Chirped Mirrors," *Opt. Lett.* 22: 831-33 (1997).

The optimized OCT system can be connected to a scanning system for *in vitro* or *in vivo* imaging or to an ophthalmic slit-lamp instrument for taking cross-sectional OCT images of retinal microstructures. These pulse durations and bandwidths in combination with the optimized OCT system resulted in longitudinal resolutions of less than 2 μm. This enables *in vivo* tomograms with the highest resolution ever achieved to be obtained (Figure 30).

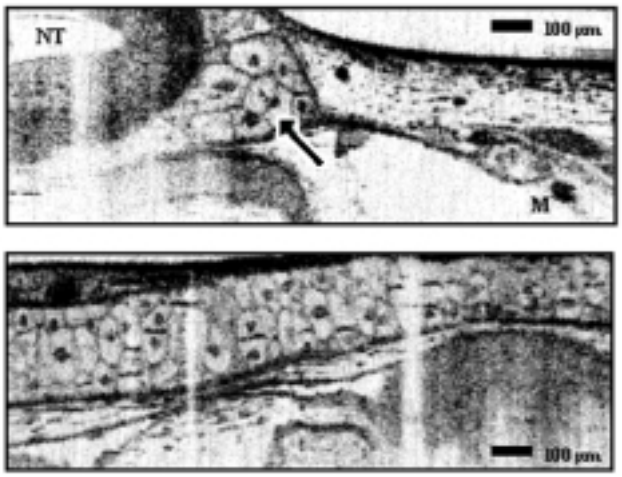

Figure 30. *In vivo* subcellular level resolution (2 x 5 μm, longitudinal x transversal) tomograms of an African tadpole. Multiple mesanchymal cells of various sizes and nuclear-to-cytoplasmic ratios, the mitosis of two cells (arrow), the neural tube (NT), as well as melanocytes (M) are clearly shown.

In addition to the ultrahigh resolution that can be achieved by using the broad bandwidth of the KLM Ti:Al_2O_3 laser, this system could also be applied for spectroscopic studies of biological tissues. Spatially localized, wavelength dependent scattering and absorption can be obtained in addition to the subcellular level resolution tomograms by (1) recording the full interferometric fringe signal, instead of the envelope used for standard OCT imaging, and (2) applying Fourier signal processing. This technique for obtaining spectroscopic information could prove extremely powerful, e.g., in evaluating the oxygenation or wavelength dependent absorption and scattering characteristics of retinal layers, cancerous tissue or other biological systems.

Real-Time Portable OCT System and Hand Held Surgical Probe

The feasibility of OCT for accessing micron-scale pathology of a variety of nontransparent biological tissues has been demonstrated through extensive *in vitro* studies.[74] Another major step toward advancing OCT as a clinically viable and diagnostically useful imaging modality has also been achieved by *in vivo* imaging of the gastrointestinal, urinary, and cardiovascular systems in rabbits.[75] The next challenge is to demonstrate the imaging and diagnostic capability of high-resolution, real-time, OCT imaging on human subjects. To achieve this objective, a portable OCT system is required. The major features that are important for a portable OCT system are speed, compactness, robustness, and clinically viable beam delivery and collection OCT probes.

A modular OCT system addressing the above issues has been developed and is suitable for both clinical and laboratory-based investigations. The system consists of five main modules: (1) low coherence light source, (2) beam delivery and collection probe, (3) scanning optical phase delay line, (4) interferogram detection and envelope demodulation electronics, and (5) display and recording devices (super VHS and computer). The compact low-coherence source, based on a semiconductor amplifier, provides ~30 mW maximum optical power at a central wavelength of ~1310 nm with broad spectral bandwidth. The axial resolution, determined by the coherence length of the source, is ~15 μm in air and ~10 μm in tissue.

The delay line is a crucial module which determines the imaging frame rate of the system. Real-time imaging of ~2000 axial scans per second, corresponding to ~4-8 frames/sec, is achieved by using a novel high-speed optical phase control delay line which we have recently developed.[76] The phase control delay line is similar to that used for femtosecond pulse shaping. In essence, it contains a lens-grating pair to perform a Fourier transform of the temporal profile of the low-coherence light. A mirror, placed at the Fourier plane, maps the angular tilt to the group

74 M.E. Brezinski, G.J. Tearney, B.E. Bouma, S.A. Boppart, M.R. Hee, E.A. Swanson, J.F. Southern, and J.G. Fujimoto, *Circulat.* 92: 103 (1995); G.J. Tearney, M.E. Brezinski, J.F. Southern, B.E. Bouma, S.A. Boppart, and J.G. Fujimoto, *Am. J. Gastroenterol.* 92: 1800-04 (1997); C. Pitris, M.E. Brezinski, B.E. Bouma, G.J. Tearney, J.F. Southern, and J.G. Fujimoto, *Am. J. Respir. Crit. Care Med.* 157: 1640-44 (1998).

75 J.G. Fujimoto, S.A. Boppart, G.J. Tearney, B.E. Bouma, C. Pitris, and M.E. Brezinski, submitted to *Heart*.

76 G.J. Tearney, B.E. Bouma, and J.G. Fujimoto, "High Speed, Phase- and Group-Delay Scanning with a Grating-Based Phase Control Delay Line," *Opt. Lett.* 22: 1811 (1997).

delay and varies the optical path length in the reference arm by scanning the angle. The total optical path length delay or axial scanning depth, determined by the angular scanning range of the galvanometer in the delay line, is ~4 mm.

A second generation, forward hand-held imaging probe which is suitable for intraoperative imaging has been designed and constructed. The previous hand-held probe was based upon a two-lens telescope system.[77] The transverse scanning was accomplished by using a piezoelectric cantilever to move the fiber tip in the focal plane of the first lens. The fiber tip is relay-imaged to the specimen by the second lens. The probe was very compact, simply designed, and easy to build and use. The major disadvantages of this design were limited transverse scanning range, nonlinearity and hysteresis of the piezoelectric cantilever, and potential hazard of the high voltages applied to the cantilever.

For these reasons, we designed a second generation of hand-held OCT surgical probes. The new probe design contains four lenses to relay-image the fiber tip to the object, and a galvanometer to steer the beam. The beam from an optical fiber is collimated by the first lens, expended/shrunk by the second and the third one, and focused to the sample by the last one. The galvanometer, placed between the first and the second lens and driven at very low voltage, enables a wide transverse scanning range without introducing non-linearity or hysteresis. The probe length can be easily changed without affecting the beam characteristics at the focal point on the sample. In addition, the working distance, determined by the focal length of the last lens, can be chosen for specific need. The overall diameter of the probe is about 1.5 cm and the total length is about 15 cm. The working distance is about 2.5 cm from the distal end of the probe and the transverse resolution is ~31 μm. The hand-held probe consists of an inner and an outer shell. The outer shell along with the last lens is detachable from the rest of the probe. This permits the pre-sterilization of the outer shell which is essential to keep the surgical field sterile during intraoperative studies.

1.20.2 Optical Biopsy Using Optical Coherence Tomography

Arterial Imaging

Coronary artery disease remains the leading cause of death in the industrialized world.[78] Most myocardial infarctions result from the rupture of small plaques in the coronary arteries, rather than the large symptomatic plaques seen on angiography. When these plaques rupture, they release thrombogenic lipid, a clot forms, and the vessel occludes. These vulnerable plaques are characterized by a large collection of lipid within the plaque covered by a thin layer of intima (“intimal cap”).

Vulnerable plaques are below the detection limit of currently available imaging technologies. High-frequency intravascular ultrasound (IVUS), the current clinical technology with the highest resolution, has an axial resolution no greater than 110 μm. Since stress analysis studies have demonstrated that the intimal cap over lipid collections are less than 100 μm in vulnerable plaques, no technology in clinical medicine has sufficient resolution to identify these plaques.[79]

With axial resolutions from 2–20 μm, OCT represents a 50× improvement over IVUS and has recently been applied to *in-vitro* nontransparent tissue, including atherosclerotic plaque.[80] Microstructural details such as thin intimal caps, focal lipid deposits, and fissures have been identified at 16 μm resolution. A high-speed catheter-based OCT imaging system has been developed for intravascular imaging. Because the OCT system is composed of

77 S.A. Boppart, B.E. Bouma, C. Pitris, G.J. Tearney, J.G. Fujimoto, and M.E. Brezinski, *Opt. Lett*. 22: 1618 (1997).

78 K.J. Isselbacher, E. Braunwald, J.D. Wilson, J.B. Martin, A.S. Fauci, and D.L. Kasper, eds., *Harrison’s Principles of Internal Medicine*, 13th ed. (New York: McGraw-Hill, 1994).

79 H.M. Loree, R.D. Kamm, R.G. Stringfellow, and R.T. Lee, “Effects of Fibrous Cap Thickness on Peak Circumferential Stress in Model Atherosclerotic Vessels,” *Circulat. Res.* 71(4): 850-58 (1992).

80 M.E. Brezinski, G.J. Tearney, B.E. Bouma, J.A. Izatt, M.R. Hee, E.A. Swanson, J.F. Southern, and J.G. Fujimoto, “Optical Coherence Tomography for Optical Biopsy. Properties and Demonstration of Vascular Pathology,” *Circulat.* 93(6): 1206-13 (1996); M.E. Brezinski, G.J. Tearney, N.J. Weissman, S.A. Boppart, B.E. Bouma, M.R. Hee, A.E. Weyman, E.A. Swanson, J.F. Southern, and J.G. Fujimoto, “Assessing Atherosclerotic Plaque Morphology: Comparison of Optical Coherence Tomography and High Frequency Intravascular Ultrasound,” *Brit. Heart J.* 77: 397-403 (1997); M.E. Brezinski, G.J. Tearney, B.E. Bouma, S.A. Boppart, M.R. Hee, E.A. Swanson, J.F Southern, and J.G. Fujimoto, “Imaging of Coronary Artery Microstructure (in vitro) with Optical Coherence Tomography,” *Am. J. Cardiol.* 77: 92-93 (1996).

fiberoptics, an inexpensive 2.9 French (1 mm) catheter delivery system can be constructed.[81] Transluminal imaging completely through the *in-vitro* normal coronary artery has been achieved. The high-speed OCT system based on a phase control delay line can acquire images at a rate of 4-8 frames/second with an axial resolution of ~10 μm.

Recently, *in vivo* OCT images were acquired from the abdominal aorta of a normal, 12-week-old New Zealand White rabbit (Figure 7). The high-resolution *in vivo* images delineated vascular microstructural detail. High contrast was noted between the media and the surrounding adventitia. Structures within the adventitia, such as a vein, can be distinguished. To acquire these *in-vivo* images, saline injections at relatively low pressure and small volumes were required to compensate for signal attenuation by blood. The presence of particulate matter (such as red blood cells) in blood scatters light and reduces image penetration.[82] If saline injections are required for *in vivo* patient imaging, clinicians will need to weigh the increased resolution and low cost against the likely increase in procedure time. This work, taken together with previous studies examining *in vitro* atherosclerotic plaque, strongly suggests a role for OCT in the high-resolution intra-arterial assessments of coronary atherosclerosis. Future investigations will focus on the examination of a pathologic rabbit model and on technology development to improve penetration through blood, increase acquisition rates and integrate the system with low-cost light sources.

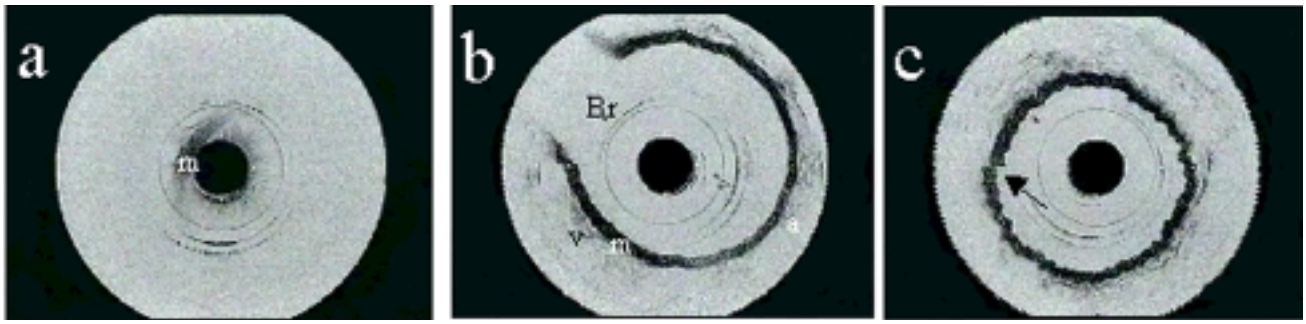

Figure 31. Three *in vivo* intraarterial OCT images. (a) In presence of blood, only arterial segment directly adjacent to the catheter can be visualized. (b) Microstructural detail can be delineated when saline is used to remove scattering effect of blood. The media [m] can be distinguished from the adventitia [a]. Structures within the adventitia, such as a small vein [v] can be distinguished. An arterial branch [Br] off of the aorta is noted. (c) Motion artifacts are present when imaging at 4 frames per second. [arrow]

Early Neoplastic Diagnosis

Techniques for diagnosis and management of neoplasia have advanced considerably, offering patients better care and additional treatment alternatives. Endoscopy, x-ray computed tomography (CT), and magnetic resonance imaging (MRI) provide the clinician with an additional set of indicators and augment the accuracy of excisional biopsies. However, early neoplastic changes remain beyond the detection limits of these modalities. The diagnosis of early cancer is still based mostly on biopsy and identification of structural and cellular changes associated with the disease. However, a large false negative error is associated with the biopsy process, mainly due to sampling errors. That error does not significantly improve even under the guidance of the above imaging modalities.

A technology capable of imaging tissue, at or near the cellular level, could lead to the detection of pathology at earlier stages than currently possible by guiding biopsies effectively to the suspect areas. Small, focal, neoplastic lesions would thus be detected earlier, before they progressed to cancer. This could significantly improve patient outcomes since once cancer becomes invasive and metastatic cure is difficult. The current clinical technology with the greatest resolution is high frequency ultrasound (30 MHz). It has a maximal resolution of 110 μm, but

81 G.J. Tearney, M.E. Brezinski, B.E. Bouma, S.A. Boppart, C. Pitris, J.F. Southern, and J.G. Fujimoto, "*In Vivo* Endoscopic Optical Biopsy with Optical Coherence Tomography," *Sci.* 276: 2037-39 (1997).

82 J.M Steinke, and A.P. Shepherd, "Comparison of Mie Theory and the Light Scattering of Red Blood Cells," *App. Opt.* 27: 4027-33 (1988).

is insufficient to identify changes in epithelial or other microstructure.[83] In contrast, OCT has been shown to achieve resolutions in the cellular and subcellular range (2-20 μm) and could improve the diagnostic sensitivity and specificity of clinical imaging procedures.

Human neoplastic tissues from several sites were imaged *in vitro* to assess the ability of OCT to detect diagnostically useful microstructural information. Neoplastic specimens from the urinary, gastrointestinal, and female reproductive tracts were obtained from surgically excised specimens and imaged fresh. In all cases, OCT was capable of imaging microstructural changes that could be used to differentiate normal from abnormal tissue.

OCT images of invasive transitional cell carcinoma of the bladder illustrated the distraction of the boundaries between the tissue layers which were normally visible. In addition, there was a lack of blood vessels and sections of muscle bundles appeared distorted. In the case of colon cancer, OCT was also able to detect changes in the layer microstructure. The ordered, narrow crypts and villi, which are characteristic of a normal colon, were dilated and disorganized. Epithelial layer changes and mass growth, associated with esophageal carcinoma and Barrett's esophagus, a pathology predisposing patients to cancer, were also observed. Structural changes associated with neoplasia were also detected in samples of the human cervix and uterus, where distortion of the normal layer and crypt structure, as well as necrosis, cysts, and mass growth were present. The structure of these tumors was confirmed by histopathology.

Diagnostic imaging should be able to correctly identify and stage early neoplastic changes. Since OCT imaging yields data in electronic form, it is well suited for a number of image processing techniques. The use of image processing is demonstrated via imaging cervical neoplasias. Neoplastic changes in the human cervix include distortion and/or invasion of the basal membrane and loss of differentiation with highly nucleated cells especially near the basal layers. The ability of OCT to extract the basal layer position and epithelial thickness and quantify changing backscattering properties was evaluated on *in vitro* samples. Distortion of the epithelial thickness and increased backscattering was observed in areas of varying degrees of neoplastic infiltration.

Studies demonstrate the feasibility of OCT for imaging clinically relevant microstructure of neoplastic lesions. Tissue specimens from the gastrointestinal, urinary, and female reproductive tracts were examined because of their clinical implications. Sharp differentiation of structures included the tissue layer boundaries, epithelium, glands, supportive tissue, and intramural cysts. The recent demonstration of fiberoptic endoscope based real time OCT *in vivo* in an animal model suggests the feasibility of ultimately applying this technique *in vivo* in humans. It is improbable that an imaging technology such as OCT would be cost effective for screening the general patient population for early neoplasias. The development of serological tests could significantly reduce the cost of screening for some types of cancer by making such tests available to a broad range of the general public. However, a role for OCT is envisioned in scenarios such as the follow-up management of neoplasia and the evaluation of patient response to radiation or chemotherapy, where it has the potential to reduce biopsies and improve patient outcomes.

Guiding Surgical Intervention

The surgical laser has been effective in the surgical suite because it provides (1) a cutting and coagulation tool with controllable powers, (2) a compact, flexible fiberoptic delivery system, and (3) wavelength- and tissue-specific cutting efficiencies.[84] Lasers are becoming standard instruments for the ablation of endometrial foci of the reproductive tract,[85] interstitial laser ablation of tumors,[86] and for surgical ophthal-

83 A.C. Fleischer, G.C. Kalemeris, J.E. Machin, S.S. Entman, A.E. James, "Sonographic Depiction of Normal and Abnormal Endometrium and Histopathologic Correlation," *J. Ultrasound Med*. 5: 445-52 (1986); F.Y. Chan, M.T. Chau, T.C. Pun, C. Lam, H.Y.S. Ngan, L. Leong, R.L.C. Wong, "Limitations of Transvaginal Sonography and Color Dopler Imaging in the Differentiation of Endometrial Carcinoma from Benign Lesions," *J. Ultrasound Med*. 13: 623-28 (1994).

84 J.P. Minton, "The Laser in Surgery. A 23 Year Perspective," *Am. J. Surg*. 151: 725-29 (1986); J.H. Talamo, *Laser Surgery* (Philadelphia: Lippincott-Raven Publishers, 1996).

85 W.R. Keye, Jr., L.W. Hansen, M. Astin, and A.M. Poulson, Jr., "Argon Laser Therapy of Endometriosis: A Review of 92 Consecutive Patients," *Fertil. Steril.* 47: 208-12 (1987).

86 K. Dowlatshahi, D. Babich, J.D. Bangert, and R. Kluiber, "Histological Evaluation of Rat Mammary Tumor Necrosis by Interstitial Nd:YAG Laser Hyperthermia," *Lasers Surg. Med*. 12: 159-64 (1992).

mologic procedures.[87] While laser use has been widespread, control and dosimetry of the delivery of laser radiation has relied largely on visual feedback of the surface ablation site. This is a limitation which, by not allowing full visualization of the location and extent of subsurface tissue ablation, has the potential to result in iatrogenic injury. Advancements in high-resolution image-guidance technologies coupled with the ability to tightly focus a laser beam would permit precise ablation of tissue, such as a neoplasm, while minimizing collateral injury. Currently, however, no intraoperative imaging technique exists with sufficient resolution to guide the placement and fast acquisition rates to image the dynamics of surgical laser ablation. A compact, high-resolution, high-speed imaging technique capable of monitoring tissue coagulation, cutting, and ablation intraoperatively at a localized site would permit image-guided surgical laser procedures to be monitored for controlled therapy and subsequent reduction in iatrogenic injury.

Studies have shown the feasibility of using OCT as a surgical diagnostic tool,[88] for intraoperative monitoring of microsurgical anastomoses of vessels and nerves,[89] and for guiding surgical laser interventions.[90] OCT had been used to characterize the changes in the retina following laser injury, however, images were acquired at 5 s intervals.[91] No studies have been performed using high-speed OCT to image real-time changes in optical backscatter in highly scattering tissues during laser ablation. We have investigated the feasibility of using high-speed OCT imaging to guide the placement and follow the dynamics of surgical laser ablation. Argon laser ablation at 514 nm, a wavelength frequently used surgically, was performed in different *ex vivo* rat organs to assess OCT imaging performance and variations between tissue types. The use of OCT to monitor ablative therapy in real-time may enable more precise control of laser delivery and a reduction in iatrogenic injury.

Before performing dynamic imaging studies, a single ablation site was imaged and thoroughly investigated to determine what optical changes within tissue, following laser ablation, were detectable with OCT. A 10 s, 3 W argon laser exposure was used to form an ablation crater in rat rectus abdominis muscle. Sixty cross-sectional images were acquired at 100 μm intervals to produce a 3-D data set. One projection from this data set is shown (Figure 32A). The deep crater can be seen in the center of the projection. Surrounding the crater is an elevated region of damage which decreases radially outward from the center. A sequence of cross-sectional images from this data set is shown (Figure 32B). These provide information on the depth- and distance-dependent distribution of the thermal energy. The number in each image refers to the distance from the center of the crater at which the cross-sectional image was acquired.

Surrounding the deep crater lie concentric rings of tissue damage (Figure 32A). These are the result of a radial thermal distribution outward from the site of the incident beam. To optimally assess these radial distributions, the 3-D data set is re-sectioned in the *en face* plane, as would be viewed from the surface and with increasing depth into the tissue. Re-sectioned slices are shown (Figure 32C). The number in each figure refers to the depth of the reconstructed plane from the surface.

87 A. Pollack, A. Milstein, M. Oliver, and M. Zalish, "Circumferential Argon Laser Photocoagulation for Prevention of Retinal Detachment," *Eye* 8: 419-22 (1994); C.P. Lin, Y.K. Weaver, R. Birngruber, J.G. Fujimoto, and C.A. Puliafito, "Intraocular Microsurgery with a Picosecond Nd:YAG Laser," *Lasers Surg. Med*. 15: 44-53 (1994).

88 M.E. Brezinski, G.J. Tearney, S.A. Boppart, E.A. Swanson, J.F. Southern, and J.G. Fujimoto, "Optical Biopsy with Optical Coherence Tomography: Feasibility for Surgical Diagnostics," *J. Surg. Res*. 71: 32-40 (1997).

89 S.A. Boppart, B.E. Bouma, C. Pitris, G.J. Tearney, J.F. Southern, M.E. Brezinski, and J.G. Fujimoto, "Intraoperative Assessment of Microsurgery with Three-Dimensional Optical Coherence Tomography," *Radiol.* 208: 81-86 (1998).

90 S.A. Boppart, *Surgical Diagnostics, Guidance, and Intervention using Optical Coherence Tomography*, Ph.D. diss., Harvard-MIT Division of Health Sciences and Technology, MIT, 1998.

91 C.A. Toth, R. Birngruber, S.A. Boppart, M.R. Hee, J.G. Fujimoto, C.D. DiCarlo, E.A. Swanson, C.P. Cain, D.G. Narayan, G.D. Noojin, and W.P. Roach, "Argon Laser Retinal Lesions Evaluated in Vivo by Optical Coherence Tomography," *Am. J. Ophthalmol*. 123: 188-98 (1997).

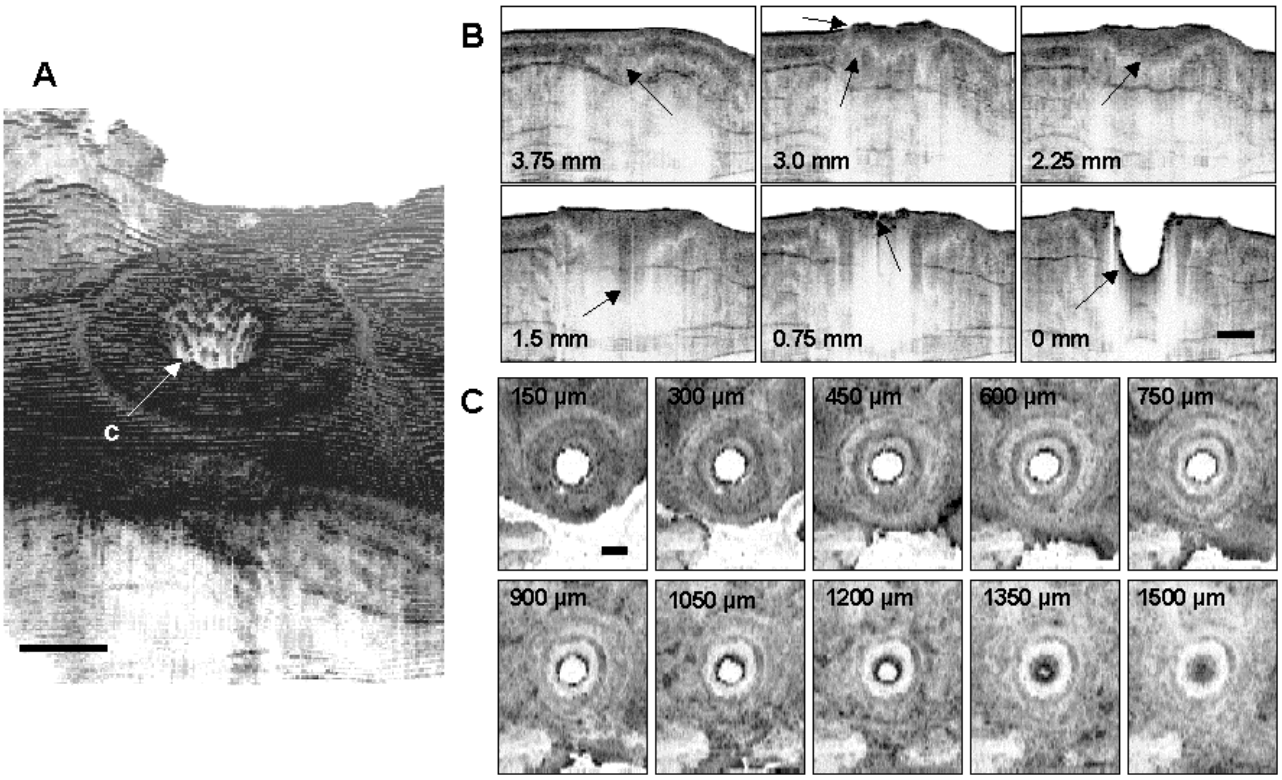

Figure 32. Laser ablation crater. Three-dimensional projection and re-sectioned data sets are shown for a 3 W, 10 s argon exposure of rat rectus abdominis muscle. A) 3-D projection illustrates central ablation crater (c) and concentric zones of thermal injury. B) Cross-sections through crater. Numbers refer to distance from crater center. Arrows indicate features described in text. C) *En face* sections in depth illustrate concentric zones of damage. Numbers refer to depth below surface. Bar represents 1 mm.

Ablation dynamics represented as changes in optical backscatter within the OCT images are shown (Figure 33). The ablation threshold at which tissue is ejected is documented by a sequence of images showing thermal injury in rat liver. A super-threshold ablation sequence with corresponding histology (Figure 33). The exposure is allowed to continue for 6 s, resulting in ejection of tissue and crater formation. The super-threshold histology shows marked tissue ablation and fragmentation within the lesion crater. These results demonstrate the ability of high-resolution, high-speed OCT to guide the placement of laser ablation sites and image the dynamic changes that occur during thermal tissue ablation. These results suggest that OCT may play a role in image-guided surgical procedures. Future *in vivo* studies are necessary to demonstrate the performance of OCT during intraoperative scenarios.

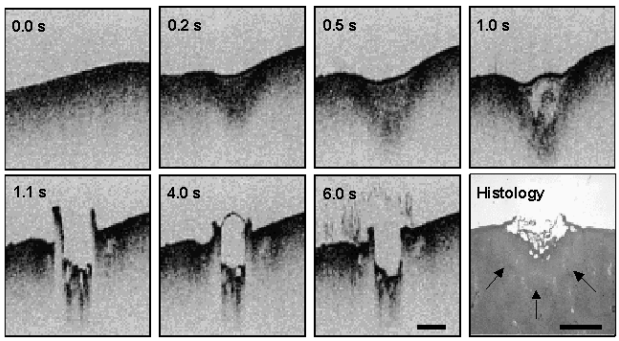

Figure 33. Guiding surgical ablation. Ablation sequence from 1 W, 7 s argon exposure resulting in ejection of tissue. Under OCT image guidance, exposure was continued during submembrane tissue vacuolization, membrane rupture, and crater formation. The corresponding histology confirms that tissue was ejected and that thermal injury surrounds ablation crater (arrows). Bar represents 1 mm.

Real-Time Intraarticular Imaging of Human Subjects with Optical Coherence Tomography

Osteoarthritis (OA) is common degenerative joint disease. It affects an estimated 40 million American along. The resolution of currently available clinical imaging modalities including x-ray, ultrasound, computed tomography (CT), and magnet resonance imaging (MRI), is insufficient to identify mircostructural articular changes, in particular the abnormalities associated with cartilage degeneration at early stage. OCT, which is capable of micron-scale, noninvasive ranging, and a few millimeter penetration, has been demonstrated to fill the void in high resolution rheumatologic diagnostics. In addition, polarization sensitivity has been found to provide clinical useful information in detecting early cartilage degeneration.

Clinical investigations were conducted in collaboration with Dr. Scott Martin at the Veterans Administration Medical Center and Harvard Medical School. The objective of these studies was to demonstrate the feasibility of accessing the internal microstructure of osteoarthritic cartilage during partial knee replacement surgery. When the knee joint was fully exposed, real-time OCT imaging was performed by using the portable OCT system with a hand held forward imaging probe. Images of 512 x 248 pixels, corresponding to a two-dimensional tissue cross section of ~5 mm in width by ~2.4 mm in depth, were generated at 4 frames per second with <4.5 mW incident light power on the articular surface. Figure 34a and Figure 34b illustrate representative cross-sectional OCT images of an osteoarthritic joint. The cartilage corresponding to the left portions of these two images is normal and the right is pathologic (degenerated). The right portion of the cartilage was severely degenerated and much thinner compared to the left.

We found that transition junctions between normal and pathologic cartilage in both images are resolved. The occurrence of layered contours of backscattered intensity as a function of depth, which is sensitive to the polarization state of the incident light, is readily observed in the normal portions of the cartilage. This layered appearance results from birefringent nature of collagen fiber matrices with organized orientation. Note that stronger birefringence exists in patella cartilage than in tibia cartilage since patella cartilage, one of the fibrocartilage, has more thick collagen fiber bundles than tibia cartilage, one of the elastic cartilage. No pronounced layered structures were observed in the pathologic portions (right portions) of the cartilage resulting from the loss of organized orientation of collagen fiber due to the degeneration.

This study demonstrates that real-time, high-resolution *in vivo* imaging of articular tissues can be accomplished with a portable OCT system within clinical settings. The compactness and portability of an OCT system makes it suitable for the tight confines of surgical suites and outpatient offices. Polarization sensitivity to collagen fiber within cartilage, in adjunct to microstructural morphologies, provides a usefully clinical diagnostic tool to detect early joint degeneration and differentiate normal cartilage from pathologic one. With the capability of a few millimeters penetration, OCT reveals the cartilage thinning and the bone-cartilage interface in some cases. Abnormalities such as new bone growth and fibrillation can also be identified.

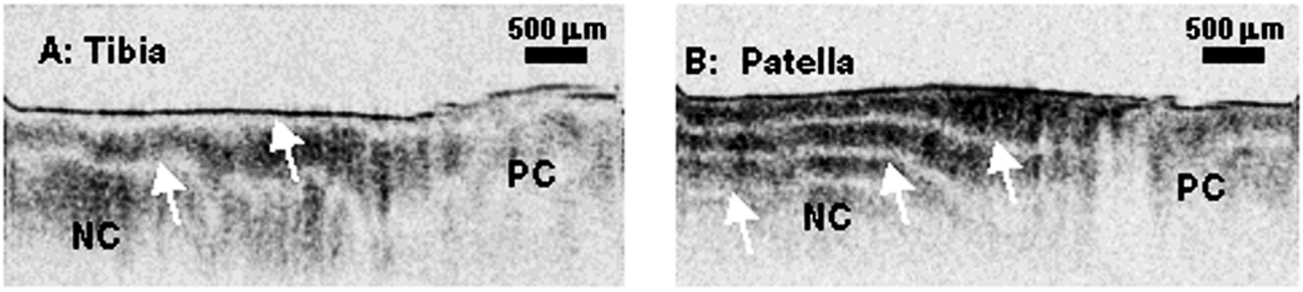

Figure 34. *In vivo* images of a human knee taken with a real time, portable OCT system during a partial knee replacement surgery. The normal and pathologic portions of the cartilage are indicated by NC and PC, respectively. The layered contours indicated with arrows result from the birefringence of the collagen fiber matrices, and this layered appearance is observed only in the normal portion of the cartilage.

1.20.3 Surgical Intervention Studies with Optical Coherence Tomography

Laser Ablation

Surgical lasers are becoming standard instruments in the operating suite. They are effective as a cutting and coagulation tool, which is demonstrated through their ease of control, compact, flexible fiberoptic delivery system, and wavelength and tissue specific cutting efficiencies. Limitations exist, however, with the potential of iatrogenic injury by not allowing full visualization of the location and extent of subsurface tissue ablation.[92]

Presently, there is no intraoperative imaging technique with sufficient resolution to guide the placement and fast acquisition rates to image the dynamics of surgical laser ablation.[93] The ideal imaging system would be compact and capable of producing real-time, high-speed as well as high-resolution images while monitoring tissue coagulation, cutting, and ablation.

We have studied OCT's feasibility as a high resolution, cross-sectional imaging technique which provides information on the optical scattering properties of tissues, thus making it attractive for guiding surgical ablation.[94] OCT can accurately monitor distributions of ablative damage because the thermal injury disrupts the normal optical properties of the tissues. The resolutions of OCT are sufficient to resolve changes in optical backscatter and identify regions of ablated tissue.[95] Consequently, improvements in resolution will improve the ability to identify tissue microstructure and detect more subtle thermal damage in tissues such as brain, liver, and kidney.

Since OCT imaging is fiber-based, it can be integrated with hand-held surgical probes. The imaging is noncontact and thus can be performed through air. The systems are compact and portable, benefiting the operating suite. Lastly, the images are performed at high speeds, allowing data to be acquired over large regions of tissues.

1.20.4 Ophthalmic Imaging and Diagnosis with Optical Coherence Tomography

Glaucoma Studies and Measurement Reproducibility

Glaucoma represents an important cause of blindness worldwide and occurs in approximately 1-2 percent of people over the age of 60.[96] Although a progressive disease, medical and surgical treatments have been developed to slow visual field loss, making early diagnosis clinically important. Primary open-angle glaucoma (POAG), the most common form of adult glaucoma, is often undetected until extensive retinal damage and visual field loss has occurred. POAG results in the destruction of the retinal nerve fiber layer (NFL) and may lead to ocular hypertension. The current clinical techniques of slit-lamp biomicroscopy, stereo fundus photography, and red-free nerve fiber layer photography used to evaluate patients are subjective and variability exists even between experienced observers.[97] The development of a technique that can accurately and objectively quantify NFL thickness will be of great benefit for glaucoma diagnosis and treatment evaluation.

OCT has demonstrated the ability to perform direct, quantitative assessment of NFL and retinal thickness.[98] Image processing is applied to OCT tomograms to identify boundaries of the vitreoretinal

92 J.H. Talamo, *Laser Surgery* (Philadelphia: Lippincott-Raven Publishers, 1996).

93 M.P. Black, T. Moriarty, E. Alexander, P. Stieg, E.J. Woodard, P.L. Gleason, C.H. Martin, R. Kikinis, R.B. Schwartz, and F.A. Jolesz, "Development and Implementation of Intraoperative Magnetic Resonance Imaging and Its Neurosurgical Applications," *Neurosurg.* 41: 831-45 (1997).

94 W.-C. Lin, M. Motamedi, and A.J. Welch, "Dynamics of Tissue Optics During Laser Heating of Turbid Media," *Appl. Opt*. 35: 3413-20 (1996); G.H. Pettit, M.N. Ediger, and R.P. Weiblinger, "Dynamic Optical Properties of Collagen-Based Tissue During ArF Excimer Laser Ablation," *Appl. Opt*. 32: 488-93 (1993).

95 S.A. Boppart, J. Herrmann, C. Pitris, D.L. Stamper, M.E. Brezinski, and J.G. Fujimoto, "High Resolution Optical Coherence Tomography-Guided Laser Ablation of Surgical Tissue," *J. Surg. Res*., forthcoming.

96 K.J. Isselbacher, E. Braunwald, J.D. Wilson, J.B. Martin, A.S. Fauci, and D.L. Kasper, eds., *Harrison's Principles of Internal Medicine*, 13th ed. (New York: McGraw-Hill, 1994).

97 J.M. Tielsch, J. Katz, H.A. Quigley, N.R. Miller, and A. Sommer, "Intraobserver and Interobserver Agreement in Measurement of Optic Disk Characteristics," *Ophthalmol.* 95: 350-56 (1988).

98 J.S. Schuman, M.R. Hee, C.A. Puliafito, C. Wong, T. Pedut-Kloizman, C.P. Lin, E. Hertzmark, J.A. Izatt, E.A. Swanson, and J.G. Fujimoto, "Quantification of Nerve Fiber Layer Thickness in Normal and Glaucomatous Eyes Using Optical Coherence Tomography," *Arch. Ophthalmol.* 113: 586-96 (1995).

interface, the NFL, and the retina pigment epithelium (RPE). From this, thickness measurements can be determined. Recently a study was performed, in collaboration with the New England Eye Center, to determine the reproducibility of OCT NFL and retinal thickness measurements at different transverse resolutions (Table 1). Topographic macular thickness mapping and circumpapillary NFL thickness measurements at four different transverse resolutions (100, 200, 300, and 400 A-scans per OCT image) were performed on 10 normal eyes of 10 healthy subjects over 3 independent scanning sessions on a single day. Repeated measure regression was used to examine the effect of increasing transversal resolution on the reproducibility of NFL and retinal thickness measurements.

Topographic macular maps were obtained by performing 6 consecutive OCT images of 6 mm length and 2 mm depth at equally spaced angular orientations centered on the fovea. The scanned area was divided into 9 regions, including a 1 mm diameter central region and two concentric ring regions (1.5 mm and 3 mm radius), each being divided into four quadrants. In each of these 9 regions a mean retinal thickness ± standard error was determined. Circumpapillary NFL thickness measurements were obtained by acquiring 5 consecutive OCT images around the optic disk. The mean NFL thickness ± standard error was determined.

As shown in Table 1, high reproducibility of NFL and retinal thickness measurements could be achieved, even at low transverse resolution (100, 200 A-scans per OCT image). The square root of variance for within subject thickness measurement is less than 10 μm in all cases. For circumpapillary NFL thickness measurement, increasing transverse resolutions improved reproducibility. For macular thickness mapping, increasing transverse resolution did not improve reproducibility. This slightly decreased reproducibility at 300 and 400 A-scans may be due to the increased data acquisition time and might be improved by increasing scanning speed. Increasing transverse resolution may not significantly improve reproducibility, but it enables more detailed imaging especially in pathologic cases. The ability to quantify NFL and retinal thickness objectively and reproducibly and visualize pathology will be valuable technique in the clinical management of glaucoma. Future work will concentrate on further improving glaucoma assessment with ultrahigh resolution OCT systems and on technology development to increase acquisition speed.

Table 2: Reproducibility data for NFL and retinal thickness. Retinal thickness data from center and foveal region shown. Similar reproducibility was found for the mean retinal thickness of other segments of the topographic macular thickness map. (RT: retinal thickness; *Fovea center; **1 mm central region; ***Mean (± standard error); § Interclass correlation coefficient; §§ Square-root of within subject (between scans) variance).

A-scans	100	200	300	400
RT center* / foveal**[μm] ***	156.7 (6.4) 182.5 (5.1)	152.3 (6.5) 174.8 (5.2)	151.8 (5.9) 176.0 (5.3)	152.5 (6.9) 176.5 (5.9)
ICC§ center / foveal	0.90 / 0.94	0.92 / 0.98	0.82 / 0.95	0.84 / 0.92
SDW center/foveal [μm]§§	6.8 / 4.1	6.1 / 2.5	8.4 / 3.7	9.2 / 5.5
Mean NFL [μm]***	114.8 (3.1)	114.2 (2.8)	114.2 (2.9)	113.9 (3.0)
ICC§	0.65	0.62	0.7	0.69
SDW [μm]§§	7.0	6.8	5.8	6.2

Ultrahigh Resolution Imaging in the Eye

The eye is essentially transparent, transmitting light with only minimal optical attenuation and scattering and also provides easy optical access to the anterior segment as well as the retina. For these reasons, OCT was first investigated in ophthalmology. Ophthalmic diagnosis represents one of the most clinically developed OCT applications. Numerous clinical as well as basic studies demonstrate the potential of OCT for routine clinical ophthalmic examinations.[99] OCT has the potential to detect retinal diseases such as glaucoma and macular edema before physical symptoms and loss of vision occur.

Despite the promising and clinically valuable results of these studies, the resolution and performance of current clinical ophthalmic OCT technology is significantly below that which can be achieved theoretically and that which has been demonstrated in the laboratory. Improved resolution in ophthalmologic OCT would enable even better visualization and quantification of intraretinal structures for more sensitive and earlier diagnosis of ocular pathologies. A more precise quantification of the retinal nerve fiber layer thickness would, for example, be used for more sensitive glaucoma diagnosis and monitoring. Better resolution would improve retinal thickness measurements in macular edema as well as increase sensitivity for imaging epiretinal membranes and choroidal neovascularization in age-related macular degeneration.

The axial resolution of OCT in clinical ophthalmic systems is limited to 10-15 μm by the bandwidth of superluminescent diodes which are used as light sources. The first sub-10 μm-resolution was achieved by using broadband fluorescence from organic dye[100] and from Ti:sapphire. However, biological imaging could not be performed with these light sources due to their low brightness. By using spectrally displaced superluminescent diodes to increase optical bandwidth,[101] improved resolution retinal tomograms with 8 μm free-space resolution or ~6 μm resolution in the retina have recently been demonstrated.[102] State-of-the-art, ultrafast laser technology can be applied to achieve ultrahigh resolution OCT. Femtosecond modelocked, solid-state lasers can generate ultrabroad bandwidth, low-coherence light with a single spatial mode and high power; characteristics that are essential for OCT imaging. These lasers have recently been used to achieve OCT imaging at 4 to 6 μm axial resolution. OCT imaging *in vitro* in nontransparent tissues as well as *in vivo* cellular level OCT imaging in developmental biology specimens has been demonstrated.[103]

With recent advances in technology, including the emergence of state-of-the-art ultrahigh bandwidth femtosecond laser technology, a third generation ophthalmologic OCT technology has now been developed. The ophthalmologic OCT system is based on a fiberoptic interferometer and high speed scanner. Since the interferometer is built using fiberoptic technology that is used in optical communication, it can be engineered into a compact and robust instrument. The distal end of the optical fiber in the measurement arm of the interferometer is integrated with a slit-lamp biomicroscope. Two orthogonally mounted scanning mirrors provide lateral beam positioning to perform arbitrary scanning patterns on the retina. This new ultrahigh-resolution ophthalmic OCT system employs a short-pulse Ti:Al_2O_3 laser light source. This laser generates pulses of 5.5 fs

99 M.R. Hee, J.A. Izatt, E.A. Swanson, J.S. Schuman, C.P. Lin, C.A. Puliafito, and J.G. Fujimoto, "Optical Coherence Tomography of the Human Retina," *Arch. Ophthalmol.* 113: 325-32 (1995); C.A. Puliafito, M.R. Hee, C.P. Lin, E. Reichel, J.S. Schuman, J.S. Duker, J.A. Izatt, E.A. Swanson, and J.G. Fujimoto, "Imaging of Macular Diseases with Optical Checkreins Tomography," *Ophthalmol*. 102: 217-29 (1995); M.R. Hee, C.A. Puliafito, C. Wong, J.S. Duker, B. Rutledge, J.S. Schuman, E.A. Swanson, and J.G. Fujimoto, "Quantitative Assessment of Macular Edema with Optical Coherence Tomography," *Arch. Ophthalmol.* 113: 1019-29 (1995); M.R. Hee, C.A. Puliafito, C. Wong, J.S. Duker, E. Reichel, J.S. Schuman, E.A. Swanson, and J.G. Fujimoto, "Optical Coherence Tomography of Macular Holes," *Ophthalmol*. 102: 748-56 (1995).

100 J.S. Schuman, M.R. Hee, C.A Puliafito, C. Wong, T. Pedut-Kloizman, C.P. Lin, E. Hertzmark, J.A. Izatt, E.A. Swanson, and J.G. Fujimoto, "Quantification of Nerve Fiber Layer Thickness in Normal and Glaucomatous Eyes Using Optical Coherence Tomography," *Arch. Ophthalmol.* 113: 586-96 (1995); X. Clivaz, F. Marquis-Weible, and R.P. Salathe, "1.5 μm Resolution Optical Low Coherence Reflectometry in Biological Tissues," *Proc. Soc. Photo-Opt. Instrument. Eng*. 2083: 19 (1994).

101 W. Drexler, C.K. Hitzenberger, A. Baumgartner, O. Findl, H. Sattmann, and A.F. Fercher, "Multiple Wavelength Partial Coherence Interferometry," *Proc. SPIE*: 2930: 194-201 (1996).

102 A. Baumgartner, C.K. Hitzenberger, H. Sattmann, W. Drexler, and A.F. Fercher, "Signal and Resolution Enhancements in Dual Beam Optical Coherence Tomography of the Human Eye," *J. Biomed. Opt.* 3: 45-54 (1998).

103 B.E. Bouma, G.J. Tearney, I.P. Bilinsky, B. Golubovic, and J.G. Fujimoto, "Self Phase Modulated Kerr-Lens Mode Locked Cr:Forsterite Laser Source for Optical Coherence Tomography," *Opt. Lett.* 21: 1839-41 (1996); S.A. Boppart, B.E. Bouma, C. Pitris, J.F. Southern, M.E. Brezinski, and J.G. Fujimoto, "*In Vivo* Cellular Optical Coherence Tomography," *Nature Med.* 4: 861-65 (1998).

duration and bandwidths of up to 300 nm at 800 nm center wavelength, improving axial resolution of OCT by a factor of ~5 x.

In vivo retinal imaging with ~2-3 μm resolution has been achieved. Figure 11 shows a compression of standard and high-resolution retinal OCT images. This is the highest resolution retinal imaging demonstrated to date. This new OCT technology represents a quantum advance in performance. Hence, fundamental limits of OCT resolution in ophthalmology and its implications for future clinical and research applications can be explored.

The results of this third generation ophthalmic OCT system show the performance of ultrahigh resolution OCT and lay the foundation for future technological improvements and clinical studies using ultrahigh resolution ophthalmologic OCT. They also demonstrate the future potential of OCT in ophthalmology as well as outline the current and fundamental limits of OCT resolution. Retinal imaging with near histological resolution would contribute to a better visualization of intraretinal structures and pathologies and would enable increased reproducibility, sensitivity, and specificity for diagnosis of ocular pathologies.

Ophthalmologic OCT has enabled the visualization of several important retinal structures. Improved axial resolution, as demonstrated with this novel system, would enable a more detailed and specific visualization of other retinal microstructures. Examples of such structures include the RPE, Bruch's membrane, choroidal structures, inner and outer plexiform layer, as well as the photoreceptor layer. Future imaging studies would establish additional objective, quantitative diagnostic information for the practicing ophthalmologist. Increased resolution leading to visualization at near cellular level will have a significant impact on ophthalmologic research and clinical practice.

The ultrahigh ophthalmologic OCT system reported here is based on a clinically viable instrument that has been engineered for clinical use and used to perform OCT imaging in a clinical setting. The ultimate availability of this new technology for clinical research and patient care will depend mainly on the availability of lasers or other sources for ultra-broad bandwidth light. Unfortunately, at present most femtosecond solid-state lasers are relatively expensive, large research instruments. With continuing research in ultrafast laser technology, more compact and less expensive lasers can be expected to be developed in the near future.

The results obtained so far are still preliminary, and with continuing research we anticipate achieving *in vivo* retinal imaging with even higher resolutions. This unprecedented ultrahigh resolution combined with the possibility of obtaining spectroscopic information is a quantum advance in OCT technology. While further studies and clinical investigations are necessary, these preliminary results suggest that ultrahigh resolution OCT will have a powerful impact in ophthalmology.

1.20.5 Nondestructive Evaluation of Composite Materials

Techniques for nondestructive evaluation (NDE), testing, and *in situ* inspection of parts during manufacturing or design are a key technology in the U.S. and worldwide. A wide range of technologies has been developed to address the research, industrial, and government needs for NDE. Ultrasound, computed tomography x-ray imaging, magnetic resonance imaging, and optics have all found important applications for NDE in a wide range of industries including steel, composites, ceramics, polymers, plastics, semiconductor, and fiberoptic industries. Nondestructive evaluation is desirable since damage evolution can be monitored and correlated with microstructural features that can create or control the damage.

For applications in nondestructive evaluation, OCT has the advantage of providing high-resolution cross-sectional imaging of microstructures within scattering media. This imaging can be performed noncontact and in situ permitting the imaging of structure during material processing as well as repeat imaging to assess the effects of material fatigue. Using conventional superluminescent diode light sources, image resolutions of 10 microns can readily be obtained using a compact, portable technology. Higher resolutions of 5 microns and less can be achieved using research systems based on short-pulse, solid-state laser light sources.[104] Finally, imaging can be performed in real time with frame rates of 4 to 8 frames per second. These high-data acquisition rates would

104 B. Bouma, G.J. Tearney, S.A. Boppart, M.R. Hee, M.E. Brezinski, and J.G. Fujimoto, "High Resolution Optical Coherence Tomographic Imaging Using a Modelocked Ti:Al_2O_3 Laser Source," *Opt. Lett*. 20: 1 (1995).

enable possible process line applications as well as applications such as three-dimensional reconstruction.

Studies have been performed in collaboration with Dr. Joy Dunkers and Carl Zimba from National Institute of Standards and Technology (NIST)[105] to demonstrate the capability of OCT to non-destructively image microstructure and fracture in fiber composite materials.[106] Typical samples consisted of fiber bundles embedded in a background resin, running in one direction along the sample. Initial studies focused on determining optimum imaging parameters, including the angle of incidence of the imaging optical beam, the probe beam confocal parameter, the polarization of the imaging beam, and the signal-to-noise ratio of the OCT instrument. OCT images of different composite samples were acquired to show their three-dimensional structure, with a penetration depth of several millimeters. These preliminary studies found that the penetration depth was primarily limited by the index of refraction discontinuity between the resin and the fibers. In general, the axial resolution of the image is determined by scattering effects that broaden the coherence function of the backscattered light, while the transverse resolution of the image is determined by the spot size of the incident light beam. Therefore, index discontinuities can change the resolution of the imaging system.

Special samples with a lower index discontinuity were fabricated by NIST investigators, which increased the image penetration depth. We were able to perform imaging to depths of 2 mm or more, and fiber bundles were clearly visualized. Several three-dimensional images of composites, consisting of two-dimensional images taken at successive transverse planes, were acquired in order to facilitate modeling of resin flow. We also inserted an index matching fluid between a cover slip and the sample to reduce the scattering at the surface of the sample. Images taken with this setup showed improved quality and depth of penetration.

We also imaged samples consisting of fiber bundles woven like a basket, with bundles running the length of the sample in both directions, perpendicular to one another. Three-dimensional scans of these samples revealed a gradual degradation of contrast when scanning in a direction parallel to one set of bundles. To obtain better images, samples with two sets of bundles oriented at 45° to the sample axes and perpendicular to each other were prepared. Three-dimensional images of these samples clearly reveal sample structure, showing fiber bundles embedded in the resin and running in both directions.

OCT was also used for nondestructive evaluation of damage in the composite samples. Samples with unidirectional fiber bundles were subjected to impact damage, and we performed imaging along a surface crack. Three-dimensional images were obtained scanning into the depth of the sample (z direction), taking images of successive transverse planes. The propagation of cracks through the composite in the z direction was clearly visualized through the first two layers of bundles. This damage was consistent with that observed in other composites.

1.20.6 Publications

Boppart, S.A., B.E. Bouma, C. Pitris, G.J. Tearney, J.F. Southern, M.E. Brezinski, and J.G. Fujimoto. “Intraoperative Assessment of Microsurgery with Three-Dimensional Optical Coherence Tomography.” *Radiol.* 208: 81-86 (1998).

Boppart, S.A., B.E. Bouma, C. Pitris, J.F. Southern, M.E. Brezinski, and J.G. Fujimoto. “*In Vivo* Cellular Optical Coherence Tomography Imaging.” *Nat. Med.* 4: 861-65 (1998).

Boppart, S.A., M.E. Brezinski, C. Pitris, and J.G. Fujimoto. “Optical Coherence Tomography for Neurosurgical Imaging of Human Intracortical Melanoma.” *Neurosurg.* 43: 834-41 (1998).

Boppart, S.A., J. Herrmann, C. Pitris, D.L. Stamper, M.E. Brezinski, and J.G. Fujimoto. “High-Resolution Optical Coherence Tomography Guided Laser Ablation of Surgical Tissue.” *J. Surg. Res.* 82: 275-84 (1999).

Bouma, B.E., L.E. Nelson, G.J. Tearney, D.J. Jones, M.E. Brezinski, and J.G. Fujimoto. “Optical Coherence Tomographic Imaging of Human Tissue at 1.55 μm and 1.8 μm using Er- and Tm-Doped Fiber Sources.” *J. Biomed. Opt.* 3: 76-79 (1998).

Brezinski, M.E., and J.G. Fujimoto. “Optical Coherence Tomography: High Resolution Imaging in

105 Material Science and Engineering Laboratory, National Institute of Standards and Technology, Gaithersburg, Maryland.

106 J.P. Dunkers, C.G. Zimba, K.M. Flynn, D.L. Hunston, R.P. Prasankumar, X. Li, and J.G. Fujimoto, “Characterization of Optical Micro structure and Damage Using Optical Coherence Tomography,” *SPIE Symposium on Nondestructive Evaluation of Aging Infrastructure and Manufacturing*, San Antonio, Texas, March 31-April 2, 1998.

Nontransparent Tissue." *IEEE J. Quant. Electron.,* Forthcoming.

Fujimoto, J.G., S.A. Boppart, G.J. Tearney, B.E. Bouma, C. Pitris, and M.E. Brezinski. "High Resolution *In Vivo* Intraarterial Imaging with Optical Coherence Tomography." *Heart.*, Forthcoming.

Hee, M.R., C.A. Puliafito, J.S. Duker, E. Reichel, J.G. Coker, J.R. Wilkins, J.S. Schuman, E.A. Swanson, and J.G. Fujimoto. "Topography of Diabetic Macular Edema with Optical Coherence Tomography." *Ophthalmol.* 105: 360-70 (1998).

Herrmann, J.M., M.E. Brezinski, B.E. Bouma, S.A. Boppart, C. Pitris, and J.G. Fujimoto. "Two and Three Dimensional High Resolution Imaging of the Human Oviduct with Optical Coherence Tomography." *Fertil. Steril.* 70: 155-58 (1998).

Herrmann, J.M., C. Pitris, B.E. Bouma, S.A. Boppart, J.G. Fujimoto, and M.E. Brezinski. "High Resolution Imaging of Normal and Osteoartheritic Cartilage with Optical Coherence Tomography." *J. Rheumatol.* 26: 627-35 (1999).

Jesser, C.A., C. Pitris, D.L. Stamper, S.A. Boppart, G.P. Nielsen, M.E. Brezinski, and J.G. Fujimoto. "High Resolution Endoscopic Evaluation of Transitional Cell Carcinoma with Optical Coherence Tomography." Submitted to *Brit. J. Urol.*

Patwari, P., D. Keane, S.A. Boppart, L. Zhou, J. Herrmann, D.L. Stamper, J. Ruskin, J.G. Fujimoto, and M.E. Brezinski. "Micron Scale, Real-Time Imaging of Cardiac Radiofrequency Catheter Ablation." Submitted to *Circulat. Res.*

Patwari, P., N.J. Weissman, S.A. Boppart, C.A. Jesser, D. Stamper, J.G. Fujimoto, and M.E. Brezinsk. "Assessment of Coronary Plaque with Optical Coherence Tomography and High Frequency Ultrasound." Submitted to *J. Am. Coll. Cardiol*.

Pitris, C., M.E. Brezinski, B.E. Bouma, G.J. Tearney, J.F. Southern, and J.G. Fujimoto. "High Resolution Imaging of the Upper Respiratory Tract with Optical Coherence Tomography." *Am. J. Respiratory Crit. Care Med.* 157: 1640-44 (1998).

Pitris, C., A. Goodman, S.A. Boppart, J.J. Libus, J.G. Fujimoto, M.E. Brezinski. "High Resolution Imaging of Gynecological Neoplasms using Optical Coherence Tomography." *Obstet. Gynocol.* 93: 135-39 (1999).

Tearney, G.J., M.E. Brezinski, J.F. Southern, B.E. Bouma, S.A. Boppart, and J.G. Fujimoto. "Optical Biopsy in Human Pancreatobiliary Tissue using Optical Coherence Tomography." *Digest. Dis. Sci.* 43: 1193-99 (1998).

Meeting Papers

Boppart, S.A., B.E. Bouma, C. Pitris, J.F. Southern, M.E. Brezinski, and J.G. Fujimoto. "Optical Coherence Tomographic Imaging of In Vivo Cellular Dynamics." Paper published in the Technical Digest of the Meeting on Advances in Optical Imaging and Photon Migration, Orlando, Florida, March 8-11, 1998.

Boppart, S.A., J.M. Herrmann, C. Pitris, B.E. Bouma, G.J. Tearney, M.E. Brezinski, and J.G. Fujimoto. "Interventional Optical Coherence Tomography for Surgical Guidance." Paper presented at the Conference on Lasers and Electro-Optics, San Francisco, California, May 3-8, 1998.

Boppart, S.A., C. Pitris, B.E. Bouma, M.E. Brezinski, and J.G. Fujimoto. "Optical Coherence Tomography using Femtosecond Lasers." Paper presented at the Eleventh International Conference on Ultrafast Phenomena, Garmisch-Partenkirchen, Germany, July 12-17, 1998.

Brezinski, M.E., C. Pitris, S.A. Boppart, and J.G. Fujimoto. "Micron Scale Imaging of the Gastrointestinal Tract with Optical Coherence Tomography." Paper presented at the Annual Meetings of American Gastroenterological Association and American Association for the Study of Liver Diseases, New Orleans, Louisiana, May 16-22, 1998.

Fujimoto, J.G. "Optical Coherence Tomography for Biomedical Imaging." Paper presented at The International Topical Workshop on Contemporary Photonic Technologies, Tokyo, Japan, January 11-15, 1998.

Fujimoto, J.G. "Biomedical Imaging using Optical Coherence Tomography." Plenary talk presented at the Conference on Lasers and Electro-Optics, San Francisco, California, May 3-8, 1998.

Fujimoto, J.G. "Optical Coherence Tomography for Medical Imaging and Diagnosis." Paper presented at the Sixteenth International Conference on Coherent and Nonlinear Optics, Moscow, Russia, June 29-July 3, 1998.

Fujimoto, J.G. "Optical Coherence Tomography for Biomedical Imaging." Paper presented at the First International Conference on Ultrasonic Biomedical Microscanning, Eastwood Park, UK, September 1-4, 1998.

Fujimoto, J.G. "Biomedical Imaging using Optical Coherence Tomography." Paper presented at the Fourth Annual Symposium on Frontiers of Engineering, National Academy of Engineering, Irvine, California, September 17-19, 1998.

Fujimoto, J.G. "Biomedical Imaging using Optical Coherence Tomography." Paper presented at the 19th Congress of the Japan Laser Surgery and Medicine Society, Tokyo, Japan, September 24-25, 1998.

Herrmann, J.M., C. Pitris, B.E. Bouma, S.A. Boppart, J.G. Fujimoto, and M.E. Brezinski. "Two and Three Dimensional Imaging of Normal and Osteoarthritic Cartilage Microstructure with Optical Coherence Tomography." Paper published in the Technical Digest of the Meeting on Advances in Optical Imaging and Photon Migration, Orlando, Florida, March 8-11, 1998.

Pakter, H.M., J.S. Schuman, E. Hertzmark, I.D. Peiris, T. Pedut-Kloizman, M.R. Hee, L. Pieroth, J.C. Szwartz, C.A. Puliafito, J.G. Fujimoto, E.A. Swanson, and C. Mattox. "Normative Database of Nerve Fiber Layer Thickness by Age as Measured by Optical Coherence Tomography." Paper presented at the Association for Research in Vision and Ophthalmology Annual Meeting, Fort Lauderdale, Florida, May 10-15, 1998.

Peiris, I.D., J.S. Schuman, H.M. Pakter, E. Hertzmark, T. Pedut-Kloizman, M.R. Hee, L. Pieroth, J.C. Szwartz, C.A. Puliafito, J.G. Fujimoto, E.A. Swanson, and C. Mattox. "Detection of Nerve Fiber Layer Thinning in Glaucomatous Human Eyes using Optical Coherence Tomography." Paper presented at the Association for Research in Vision and Ophthalmology Annual Meeting, Fort Lauderdale, Florida, May 10-15, 1998.

Pitris, C., S.A. Boppart, B.E. Bouma, G.J. Tearney, J.G. Fujimoto, and M.E. Brezinski. "In-Vivo Catheter-Based Imaging with Optical Coherence Tomography." Paper published in the Technical Digest of the Meeting on Advances in Optical Imaging and Photon Migration, Orlando, Florida, March 8-11, 1998.

Pitris, C., S.A. Boppart, B.E. Bouma, J.G. Fujimoto. "Cellular and Neoplastic Tissue Imaging with Optical Coherence Tomography." Conference on Lasers and Electro-Optics, San Francisco, California, May 3-8, 1998.

Pitris, C., A.K. Goodman, C.A. Jesser, M.E. Brezinksi, and J.G. Fujimoto. "High Resolution Imaging of Neoplastic Changes in Gynecological Tissues using Optical Coherence Tomography." Paper presented at the 34th Annual Meeting of the American Society of Clinical Oncology, Los Angeles, California, May 16-19, 1998.

Pitris, C., S.A. Boppart, D. Stamper, M.E. Brezinski, and J.G. Fujimoto. "High Resolution Imaging of Early Neoplastic Lesions using Optical Coherence Tomography." Paper presented at the VII Mediterranean Conference on Medical and Biological Engineering and Computing, Limassol, Cyprus, June 14-17, 1998.

Toth, C.A., D.G. Narayan, K.P. Winter, W.P. Roach, C.P. Cain, G.D. Noojin, C.D. DiCarlo, S.A. Boppart, M.R. Hee, R. Birngruber, J.G. Fujimoto, and B.A. Rockwell. "Location of Picosecond Laser Retinal Injury Varies with Energy and Spot Size." Association for Research in Vision and Ophthalmology Annual Meeting, Fort Lauderdale, Florida, May 10-15, 1998.

Book

Fujimoto, J.G., and M.S. Patterson, eds. "Advances in Optical Imaging and Photon Migration." Trends in Optics and Photonics 21, Washington, DC, Optical Society of America, 1998.

1.21 A Configuration Space Soliton Model Including Loss and Gain

Sponsors

National Science Foundation
Contract ECS 94-23737
U.S. Navy - Office of Naval Research
Contract N00014-95-1-0715

Project Staff

John M. Fini, Professor Peter L. Hagelstein, Professor Hermann A. Haus

Quantum models for soliton propagation in optical fiber allow us to predict uncertainties in observable soliton variables, such as position.[107] Recently, Hagelstein has demonstrated the utility of a configuration space approach to soliton problems,[108] building off of results of Lai and Haus.[109] A configuration space approach represents a quantum system by a

107 H.A. Haus and W.S. Wong, *Rev. Mod. Phys.* 68: 423 (1996).

108 P.L. Hagelstein, *Phys. Rev. A* 54: 2426 (1996); P.L. Hagelstein, unpublished.

109 Y. Lai and H.A. Haus, *Phys. Rev. A* 40: 844 (1989); Y. Lai and H.A. Haus, *Phys. Rev. A* 40: 854 (1989).

wavefunction in the coordinates of individual particles. For example, an n-photon state can be written as (equation 3.4 in Lai and Haus[110])

$$|\Psi_n\rangle = \int dx_1 ... dx_n f_n(x_1,...,x_n)/\sqrt{n!}\hat{\phi}^\dagger(x_1)...\hat{\phi}^\dagger(x_n)\,|\,0\rangle, \quad (1)$$

where $f_n(x_1,...,x_n)$ is essentially a wavefunction of the n photon positions. That a formalism based on single photon positions is possible and useful goes against the usual way of thinking about field theory, but has been demonstrated.[111]

We would like to extend the configuration space theory because it has the flexibility to treat general quantum soliton states[112] which may deviate grossly from coherent field. Linearized or semiclassical theories[113] have been useful, but these apply to limited states. Of particular interest would be a theory predicting interference of a soliton as a single quantum particle.

As a test of the basic approach, we have calculated[114] the momentum noise induced by balanced loss and gain. The result agrees with the Gordon-Haus calculation[115] and suggests interesting new mechanisms for the effect.

1.21.1 The Model: Field and Matter

The model we use is the most straightforward coupling of a soliton field and energy states of the matter system. We combine familiar, well-studied terms in our total Hamiltonian:

$$\hat{H} = \hat{H}_{field} + \hat{H}_{matter} + \hat{H}_I \quad (2)$$

The field has been discussed in Lai and Haus,[116]

$$\hat{H}_{field} = \hbar \int dx \hat{\phi}^\dagger(x)\left[\omega_0 - i\omega'\frac{\partial}{\partial x} - \frac{\omega''}{2}\frac{\partial^2}{\partial x^2}\right]\hat{\phi}(x). \quad (3)$$
$$+c\int dx \hat{\phi}^\dagger(x)\hat{\phi}^\dagger(x)\hat{\phi}^\dagger(x)\hat{\phi}^\dagger(x)$$

It includes second-order dispersion of the medium $(\omega(k) = \omega_0 + \omega'(k-k_0) + \omega''(k-k_0)^2/2)$ and a nonlinear Kerr effect.

The soliton interacts with many loss or gain sites, each labeled by an index l. Each site has electronic two-level transitions (or final radiative states in the case of scattering) with a continuum of lowering (annihilation) operators $\hat{d}_k$,

$$\left[\hat{H}_{matter}\right]_l = \sum_k \hbar\omega_{lk}\hat{d}_k^\dagger\hat{d}_k, \quad (4)$$

The interaction we use is the simplest possible: local linear coupling.

$$\left[\hat{H}_I\right]_l = -\int \hat{j}\cdot\hat{A}d^3\vec{r} \approx V(\hat{b}^\dagger + \hat{b})[\hat{\phi}^\dagger(x_l) + \hat{\phi}(x_l)], \quad (5)$$

where V is an appropriate atomic matrix element. The interaction acts on matter through the operator $\hat{b}$, a superposition of the mode operators of matter transitions. The superposition is directly related to the spectrum of the loss or gain; for example, a Lorentzian loss spectrum corresponds to[117]

$$\hat{b} = \lim_{\Delta\omega\to 0}\sum_k\left[\frac{\Gamma\Delta\omega/2\pi}{(\Gamma/2)^2 + (\omega'_{lk})^2}\right]^{1/2}\hat{d}_k. \quad (6)$$

1.21.2 Perturbative Evolution

The effects of interest can be derived using elementary quantum techniques for evolution of coupled systems. In fact, all interesting effects follow from a first-order perturbative state evolution, which assumes weak interaction with matter

$$|\Psi_f\rangle \approx |\Psi_i\rangle + \frac{1}{i\hbar}\int_{t_i}^{t_f} d\tau \tilde{H}_I |\Psi_i\rangle. \quad (7)$$

An initial state evolves into an unperturbed component and a perturbed component with one photon exchanged,

110 Y. Lai and H.A. Haus, *Phys. Rev. A* 40: 844 (1989).

111 P.L. Hagelstein, *Phys. Rev. A* 54: 2426 (1996); P.L. Hagelstein, unpublished.

112 P.L. Hagelstein, *Phys. Rev. A* 54: 2426 (1996); P.L. Hagelstein, unpublished; F.X. Kärtner, L. Boivin, *Phys. Rev. A* 53: 454 (1996).

113 H.A. Haus and Y. Lai, *J. Opt. Soc. Am. B* 7: 386 (1990).

114 J.M. Fini, P.L. Hagelstein, and H.A. Haus, "A Configuration Space Model for Soliton Propagation Including Loss and Gain," submitted to *Phys. Rev. A*.

115 J.P. Gordon and H.A. Haus, *Opt. Lett.* 11: 665 (1986).

116 Y. Lai and H.A. Haus, *Phys. Rev. A* 40: 844 (1989).

117 C. Cohen-Tannoudji, *Atom-Photon Interactions* (New York: Wiley, 1992).

$$|\Psi_i\rangle \Rightarrow |\Psi_f\rangle = \cos(\theta)|\Psi_0\rangle + \sin(\theta)|\Psi_1\rangle \cdot \quad (8)$$

The perturbed state component is

$$\sin(\theta)|\Psi_1\rangle = \frac{1}{i\hbar}\int_{t_i}^{t_f} d\tau e^{-i\hat{H}_0(t_i-\tau)/\hbar}\hat{H}_I e^{-i\hat{H}_0(\tau-t_i)/\hbar}|\Psi_i\rangle. \quad (9)$$

As usual with this sort of calculation, the time integral enforces energy conservation. The simplest transformation involves a initial state of definite soliton energy E_{Ai} and matter energy E_{Bi} (gain case has $\varepsilon \to -\varepsilon$),

$$\begin{aligned} |\Psi_i\rangle &= |E_{Ai}, E_{Bi}\rangle \\ &\Rightarrow \sin(\theta)|\Psi_1\rangle = \int d\varepsilon T(\varepsilon)|E_{Ai}-\varepsilon, E_{Bi}+\varepsilon\rangle, \end{aligned} \quad (10)$$

where $T(\varepsilon)$ is a transmission spectrum. The final state then has a simple interpretation: If no interaction occurs (probability $\cos(\theta) \approx 1$), we are left with an unperturbed state

$$|\Psi_0\rangle = |\Psi_i\rangle \quad (11)$$

If an interaction *does* take place, the soliton acquires a spread in energy according to the transition amplitude of exchanging a photon with energy ε.

Naturally, it is essential to calculate $T(\varepsilon)$. This involves the spectrum of each subsystem instantaneously perturbed by $\hat{H}_I$. The perturbed field spectrum has been calculated in configuration space for large photon number, and has a simple form:[118] it is simply the density of optical photons, or a classical-soliton sech about E_{Ai}/n. This approximation can be argued for both loss and gain, although the processes are fundamentally different. The classical sech-spectrum of the soliton emerges without linearizing or using a semiclassical approach.

The basic transformation Eq. 10 can be easily extended to initial superpositions of energy states,

$$|\Psi_i\rangle = \int dh_i a(h_i)|E_{Ai} = nh_i, E_{Bi}\rangle \quad (12)$$

leading to

$$\begin{aligned} &\sin(\theta)|\Psi_1(t_f)\rangle = \\ &\int dh_i a(h_i)\int d\varepsilon T(\varepsilon; h_i)|nh_i - \varepsilon, E_{Bi}+\varepsilon\rangle. \end{aligned} \quad (13)$$

At a fixed n, this is in fact the most general soliton state. The applicability of this formalism to soliton states with general position wavefunctions is a key motivation for this work.

1.21.3 Group Velocity Noise

A nontrivial result which should emerge from the theory is a group velocity noise induced by loss and gain. This noise induces accumulating uncertainties in soliton positions which can be limiting for soliton communication systems via the Gordon-Haus effect.[119] From our model, we have calculated noise in quantitative agreement with the previous Gordon-Haus result, demonstrating the correctness of the model.

It is well-known that the group velocity is proportional to the soliton frequency, or energy per-photon $\hat{h} \equiv \hat{H}_{field}\hat{N}^{-1}$. We can then write for a single interaction site,

$$\delta\langle\Delta\hat{v}_g^2\rangle \propto \langle\Delta\hat{h}^2\rangle_{final} - \langle\Delta\hat{h}^2\rangle_{initial}. \quad (14)$$

Our model allows us to calculate energy uncertainties directly,

$$\frac{\langle\Delta\hat{h}^2\rangle_f - \langle\Delta\hat{h}^2\rangle_i}{\sin^2(\theta)} \approx \frac{\langle\Delta\in^2\rangle}{n^2}. \quad (15)$$

We now assume a loss rate γ, compensating gain, and a broad loss and gain spectra (compared to classical soliton spectrum), obtaining

$$\delta\langle\Delta\hat{h}^2\rangle = \frac{2\hbar^2\Delta\omega^2_{clas}}{n}\gamma\delta z \cdot \quad (16)$$

When we convert to normalized units, this agrees exactly with the result of Gordon and Haus,

$$\delta\langle\Delta\hat{\Omega}^2\rangle = \frac{\gamma\delta z}{3n}. \quad (17)$$

1.21.4 Results: Intuitive Pictures and Interpretation

The above result gives us confidence that the formalism can be applied to general quantum soliton states, for example for analyzing interference effects. However, by focusing on the particle nature of photons,

118 J.M. Fini, P.L. Hagelstein, and H.A. Haus, "A Configuration Space Model for Soliton Propagation Including Loss and Gain," submitted to *Phys. Rev. A*.

119 J.P. Gordon and H.A. Haus, *Opt. Lett.* 11: 665 (1986).

we have uncovered new interpretations of the momentum noise itself. Two intuitive and interesting interpretations arise: First, that energy uncertainty, or noise, added to the soliton results from the graininess of the energy exchange with matter. Second, that uncertainty in soliton velocity, or momentum, is induced by measurement of the position of a photon. Each interpretation connects the Gordon-Haus effect to a fundamental quantum principle.

The soliton cannot exchange energy with matter in infinitesimal amounts: only whole photons can be exchanged. In Figure 35, we show that at the heart of the quantum expression (equation 15) lies a classical effect: if a classical particle vanishes from a collection of n particles, the average energy (or position) is shifted by the offset of that particle, divided by n-1. That is $\Delta h \approx \Delta\varepsilon/n$. Quantum mechanics simply dictates the statistics of $\Delta\varepsilon$.

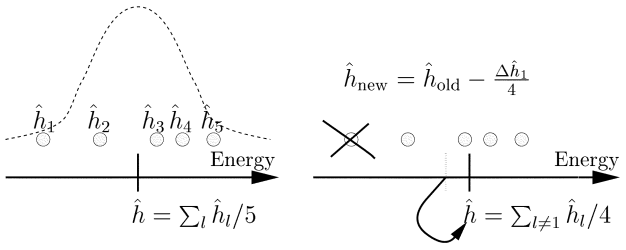

Figure 35. The configuration space approach describes a soliton as a collection of local photon particles. In the above particle picture of loss, individual photon energies are initially in a Hartree (energy-domain) wavefunction. The effect of a photon annihilation on the average energy $\hat{h}$ is a simple matter of algebra.

The measurement effect allows us to quantitatively predict group velocity noise as well. Local interaction with a broadband absorber effectively "measures" the position of the absorbed photon (this measurement is not generally accessible to an observer). This constitutes a measurement of the soliton position to limited precision—namely the classical soliton width. The quantum measurement disturbance is thus proportional to the classical soliton spectral width divided by n, as outlined in Fini, Hagelstein and Haus.[120]

1.21.5 Conclusions

Loss and gain in optical fibers transform compact soliton states into statistical mixtures with large spreads in position. Loss is then a potentially limiting effect in exploiting any coherent soliton effect, such as squeezing or whole-soliton interference. We have extended the configuration-space theory of Hagelstein[121] to allow for loss and gain. The extended theory has been validated on a test problem: we have not only confirmed the Gordon-Haus calculation of momentum noise, but shown that the configuration-space approach gives new understanding of this well-known effect.

1.22 Interference of Many-photon Quantum Particles

Sponsors

National Science Foundation
Contract ECS 94-23737
U.S. Navy - Office of Naval Research
Contract N00014-95-1-0715

Project Staff

John M. Fini, Professor Peter L. Hagelstein

Optical solitons are interesting many-photon bound quantum objects. It is well known that observable soliton variables are subject to quantum uncertainty. For example, soliton position and momentum behave exactly as those of a 1-D free quantum particle. Interestingly, the internal degrees of freedom of the field can be separated from the center-of-mass dynamics. The wavefunction for an n-photon soliton state:

$$\Psi(x_1,...,x_n) = \varphi(X)\Psi_n(x_1 - X,...,x_{n-1} - X) \qquad (18)$$

generally has an arbitrary $\psi(X)$, or center-position wavefunction, but has a fixed ground-state wavefunction Φ_n for the relative coordinates. This is analogous to a bound collection of massive particles: If the particles are in a bound internal state (an unexcited atom), the collection is completely described by the center-of-mass position.

Quantum particles, in addition to obeying uncertainty relations, can show interference effects. A two-slit interference experiment is possible with electrons or

120 J.M. Fini, P.L. Hagelstein, and H.A. Haus, "A Configuration Space Model for Soliton Propagation Including Loss and Gain," submitted to *Phys. Rev. A*.

121 P.L. Hagelstein, *Phys. Rev. A* 54: 2426 (1996); P.L. Hagelstein, unpublished.

with atoms which contain electrons. Clearly, in an atom interference experiment, we think of the atom as a single particle with a simplified internal state representation. The effect is fundamentally unlike interference of individual electrons of the atom.

This raises a question: can one observe interference of a bound photonic particle *as a whole*, not only as single-photon interference? The presence of a soliton position wavefunction, $\psi(X)$ suggests that this is possible, at least in principle. Interference of multiphoton particles has been discussed somewhat by Hagelstein,[122] but no realistic proposal for observing "fringes" in a soliton wavefunction have yet been made. We here report our preliminary study of some issues involved. In particular, we are developing a theory to assess the effects of loss on potential interference measurements.

1.22.1 Binding Energy and Adiabatic Movement

A collection of particles with no attractive forces is not bound: one can easily make a light pulse where the photons are essentially not interacting. Such a pulse will exhibit single-photon interference, but no *collective* interference of entire pulse.

The concept of binding energy further tells us quantitatively how hard we can push around a particle before disturbing its internal state. To preserve a ground state soliton, we should stay in the adiabatic limit.[122] Hagelstein has described fiber couplers which switch a pulse one way or the other without fractionating it. Classically, we can think of this as a bifurcation: the pulse holds together as long as forces are not too great. Quantum mechanically, the final state generated is (we hope) a superposition of solitons in either of the output fibers.

For ideal, lossless fibers and couplers, then, construction of a soliton interferometer would be relatively straightforward. Although real fibers and couplers are not ideal, the possibility of a fundamentally different kind of light interference is compelling.

1.22.2 Single-fiber Interferometer

Many variations on this theme are possible. We anticipate great practical difficulty in experimentally observing an effect, and have begun outlining the advantages of possible schemes. Coupling into physically distinct fibers may lead to separate interactions for different components of the superposition. If these effectively measure which path a pulse takes, such a measurement would destroy the coherence between the two wavefunction components. One could instead separate soliton components not into two fibers, but into two position slots (or frequency bands) along the length of the same fiber. This may convey an advantage, since the components now interact with identical fiber stretches.

An interference experiment may then consist of adiabatically separating or selecting quantum soliton components, and then allowing them to spread. As they overlap again, interference will appear as a modulation in space of the total wavefunction. A significant challenge is that the structure of $\psi(X)$ tends to be on a scale much smaller than a soliton width. If fringes on this size scale are produced, they will be difficult to observe; common light detectors see single photons (or perhaps two or three photons), whose distribution is $\psi(X)$ convolved by the classical soliton sech. This broad sech can smooth out the interference structure.

1.22.3 Loss

Loss in fiber is generally around 0.3 dB/km. In fact, for 1 ps solitons, using reasonable parameters, the average distance between loss events is on the order of 100 microns. The characteristic distance for an adiabatic transition is on the order of the soliton period, perhaps hundreds of meters. It thus seems extremely unlikely that pulses can be manipulated adiabatically in any material without loss of many photons.

In a sense, this high rate of loss is what makes solitons different from atoms or nuclei, which break up into constituent particles only under fairly extreme conditions. Incidentally, the length scale on which ballistic spreading of X becomes comparable with the coherent-state X-spreading is also on the order of the soliton period. This again suggests this length as a minimum propagation distance for manipulating $\psi(X)$.

Loss is potentially very damaging to interference schemes. A simple way to see this is to consider an initial n-photon soliton state consisting of two compo-

122 P.L. Hagelstein, *Phys. Rev. A* 54: 2426 (1996); P.L. Hagelstein, unpublished; P.L. Hagelstein, *RLE Progress Report No. 138* (Cambridge: MIT Research Laboratory of Electronics, 1996), p. 150.

nents $|\Psi_1\rangle$ and $|\Psi_2\rangle$. If $|\Psi_1\rangle$ loses a photon and $|\Psi_2\rangle$ does not, the resulting states are orthogonal, and do not cause interference when superposed. Even if superposed components do overlap, entanglement with the states of absorption sites can lead to measurement effects. We would like to calculate these effects in a systematic way. Using a microscopic model of interaction with a loss or gain site, we have developed a mapping of an input Gaussian wavefunction $\psi(X)$ and a statistical mixture of output Gaussians.[123] This is depicted in Figure 36.

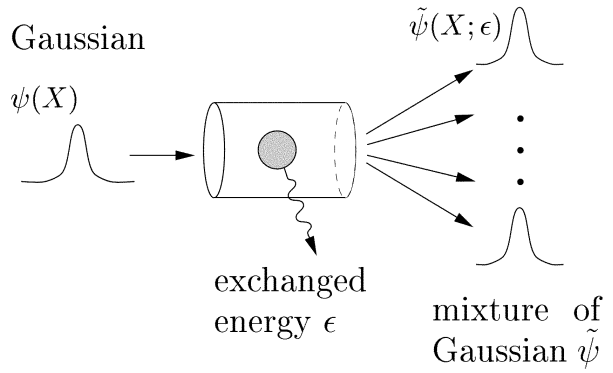

Figure 36. We depict one possible input-output picture of a loss event. A state with an initially Gaussian X-wavefunction is mapped by loss onto a mixture of perturbed Gaussian states. The result is easily extended to multiple loss events. This picture is relevant to the problem of soliton wavefunction manipulation and observation.

We now outline the transformation: An initial state with arbitrary soliton momentum wavefunction and coupled to a continuum state with energy $|E_{Bi}\rangle$ can be written as

$$|\Psi_i\rangle = \int dh_i a(h_i) |E_{Ai} = nh_i, E_{Bi}\rangle . \quad (19)$$

Here $a(h_i)$ is actually an energy-per-photon wavefunction. This relates to momentum P through $h \approx v_g P/n$, where v_g is the group velocity. During the interaction, the soliton and the continuum exchange a photon with probability S. The perturbed component of the coupled system is

$$\sqrt{S}|\Psi_1(t_f)\rangle = \int dh_i a(h_i) \int d\varepsilon T(\varepsilon;h_i) |nh_i - \varepsilon, E_{Bi} + \varepsilon\rangle \quad (20)$$

The momentum of the soliton is thus entangled with the energy of the continuum. After the pulse passes the interaction site, the continuum state is neither measured nor coupled to the field again, and so we can regard this entanglement as a statistical mixture. Under reasonable approximations, the final state is given by

$$\sqrt{S}\,|\Psi_1(t_f)\rangle = \underbrace{\int d\varepsilon T(\varepsilon;\bar{h})\,|E_{Bi} + \varepsilon\rangle}_{\text{statistical spread}} \otimes \underbrace{\int dh_i \tilde{a}_\varepsilon(h_i)\,|nh_i - \varepsilon\rangle s}_{\text{perturbed wavefunction}} \quad (21)$$

where $\tilde{a}$ is a transformed energy-domain wavefunction, and $\bar{h}$ is an average value of h_i. Specifically, the perturbed wavefunction component indexed by ε is a Gaussian with slightly displaced momentum and slightly broadened position.

The transformation of a Gaussian to a mixture of Gaussians is easily cascadable. Interaction with multiple loss or gain sites will give a perturbed state,

$$\int d\varepsilon_1 |\varepsilon_1\rangle \otimes \ldots \otimes \int d\varepsilon_k |\varepsilon_k\rangle \otimes \int dh_i \tilde{a}(h_i;\varepsilon_1 \ldots \varepsilon_k) |nh_i - \sum \varepsilon_j\rangle \quad (22)$$

where $\tilde{a}$ now has the combined effects of many displacements and dilations. This expression can be applied to the loss of coherence of a soliton state during propagation along a fiber. While we have not reached a bottom line on this issue, we make these observations: First, statistical mixing induced by loss is a sensible result which will lead, under some circumstances, to the "washing out" of interference fringes. Analogies in the interference of single photons or matter can readily be made. Second, each pure state component has a wavefunction which is only disturbed slightly by each exchanged photon. This leaves a possibility that a regime exists where many photons are lost but the position wavefunction is more or less intact. We put off a more quantitative application of the model, which will require details of the proposed physical device.

1.22.4 Conclusions

The possibility of a fundamentally new kind of light interference is very intriguing. The practical difficulties of arranging collective interference of large numbers of photons bound as a single quantum object are substantial and not yet well understood. We have made some progress developing quantum models for loss and gain which might address these issues.

123 J.M. Fini, P.L. Hagelstein, and H.A. Haus, "A Configuration Space Model for Soliton Propagation Including Loss and Gain," submitted to *Phys. Rev. A*.

A mapping of input Gaussian soliton position wavefunctions to output statistical mixture of Gaussians has been developed. It shows promise as a tool for analyzing loss effect, as it is both simple and derived from fundamental models of the interaction with matter.

1.23 Nearly Isotropic Photonic Bandgap Materials

Sponsors

National Science Foundation
Contract ECS 94-23737
U.S. Navy - Office of Naval Research
Contract N00014-95-1-0715

Project Staff

Professor Peter L. Hagelstein, Douglas R. Denison, John M. Fini

The possibility of developing a photonic bandgap material was proposed about 10 years ago by Yablonovich.[124] It was noted that radiative decay would be suppressed in the absence of available photonic modes at the decay frequency. Since that time, there has been much interest focusing on the design, the analysis and the construction of photonic bandgap structures at a variety of wavelengths from the microwave regime to the optical. In addition, numerous applications for photonic bandgap structures have been proposed.

Here we would like to report on a new approach to the design of photonic bandgap structures.[125] Previous work has largely been limited to working with what might be considered simple structures that are either closely related to well known crystal structures or else correspond to structures that are perhaps easy to construct. In either case, the available scattering power of the optical dielectric materials involved produces bands that are centered at different frequencies for different propagation directions. A bandgap for all directions opens up only when a sufficiently strong dielectric modulation is present, such that the individual bandgaps in different directions are everywhere wide enough so that there exists a small range of frequencies at which they all overlap.

1.23.1 Dielectric Modulation for Nearly Isotropic Band Gaps

Perhaps superior photonic bandgap structures could be developed if it could be arranged that the individual bandgaps in all of the different directions were designed to occur at nearly the same frequency. If so, then perhaps more efficient use could be made of the dielectric modulation strength available. In order to study this, we considered the photon band structure of materials in which the dielectric modulation occurs for different directions at the same frequency. In order to do this, we chose to study proposed optical materials whose dielectrics were distributed according to

$$\frac{1}{[\mu_0^2\varepsilon(\mathbf{r})]^2} = c_0^2\left[1+\sum_j A_j e^{i2\mathbf{k}_j\cdot\mathbf{r}}\right] \qquad (23)$$

Nearly isotropic dielectric modulation can be imposed using a collection of reflection vectors $\mathbf{k}_j$ that uniformly span the range of available angles for either 2-D or 3-D cases. The strength of the modulation is determined by the amplitudes A_j, which can be taken to be of equal strength for an isotropic distribution of reflection vectors. It is possible to select a set of reflection vectors that are nearly isotropic but consistent with an underlying crystal structure. An example that uses eight reflection vectors in 2-D that are equi-spaced in angle, but vary slightly in magnitude, produces the dielectric distribution indicated in Figure 37. This structure is designed to repeat periodically in space in both directions. The specification of a set of reflection vectors that are equi-spaced in angle and have the same magnitude produces a non-periodic spatial pattern. Such dielectrics have not been studied previously for this application.

124 E. Yablonovitch, *Phys. Rev. Lett.* 58: 2059 (1987).

125 P.L. Hagelstein and D.R. Denison, "Nearly Isotropic Photonic Band Gap Structures in 2D," *Opt. Lett.,* forthcoming.

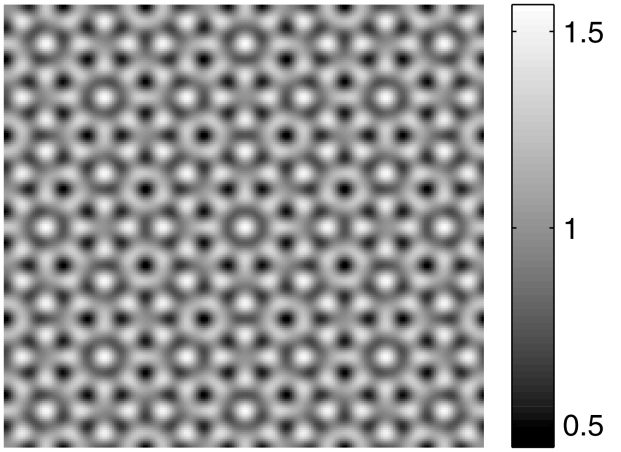

Figure 37. Inverse dielectric constant within a unit cell for N=8 using $\frac{k_j}{k_0} = (\pm 1,0),(\pm\frac{12}{17},\pm\frac{12}{17}),(0,\pm 1)$.
In this figure, $\varepsilon_{max}/\varepsilon_{min}$ = 3.5.

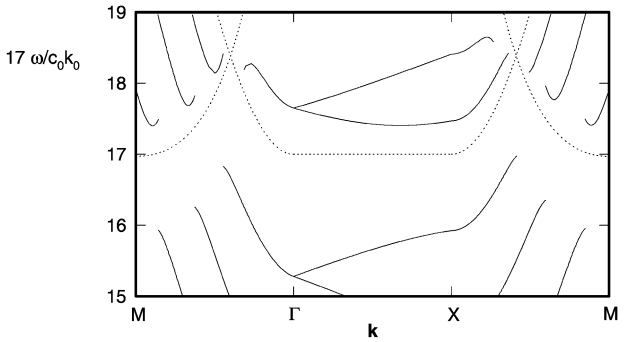

Figure 38. Dispersion relation for eight reflection vector periodic material for a scalar model as discussed in the text. Dotted lines are locations of the Bragg scattering planes; solid lines are the dispersion curves. The Γ point is [0 0], the X point is [1 0], and the M point is [1 1]. The reflection vectors chosen correspond to a line at $\omega = c_0 k_0$ between Γ and X, and at $\omega = 12\sqrt{2}/17 c_0 k_0$ at K. We have taken the coefficient for each reflection vector to be A = 0.0841 in this computation.

1.23.2 The Bandgap for Nearly Isotropic Photonic Bandgap Structures in 2-D

The photonic band structure in the vicinity of the bandgap in the case of eight reflection vectors considered above is illustrated in Figure 38. One sees that that bandgap occurs in this case at very high overtones of the fundamental lattice cell, corresponding to the situation in which a big lattice cell in space has a large amount of substructure. One observes that the Bragg planes roughly span the different angles close to the design frequency of the bandgap structure, and that the resulting bandgap is in all directions and is a relatively small fraction of the center frequency.

Using a larger number of reflection vectors leads to a more precise angular coverage, as indicated in Figure 39. The size of the bandgap can be estimated in this limit as a function of the dielectric contrast ratio; we obtain

$$\frac{\Delta\omega}{c_0 k_0} = \frac{1+\sqrt{2}}{2N}\left(\frac{\varepsilon_{max}-\varepsilon_{min}}{\varepsilon_{max}+\varepsilon_{min}}\right) - \frac{1}{2}\left(\frac{\pi}{N}\right)^2. \qquad (24)$$

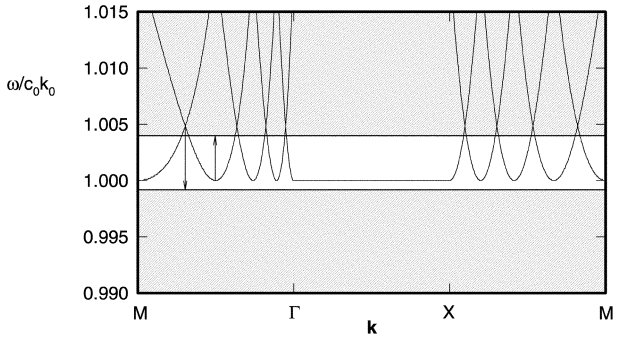

Figure 39. Schematic of band gap in the case of N = 32 and A = 0.006 (which corresponds to a much weaker dielectric modulation than in Figure 38).

1.23.3 Nearly Isotropic Photonic Bandgap Structures in 3-D

The same approach works in 3-D with some modification. The use of a sinusoidal modulation as specified above leads to a band structure that produces no bandgap in the large N limit unless dielectric constants are allowed that produce a negative value for c^2 at some locations. This is because a very large number of direction vectors are required, and the resulting superposition of equation 23 produces large amplitude swings at a small number of locations. We can fix this problem by clipping the extrema of the dielectric constant, which produces new reflections at various harmonics of the reflection vectors. This appears not to be a big price to pay to adapt the method to 3-D. For example, we might use

$$\frac{1}{\left[\mu_0^2 \varepsilon(\mathbf{r})\right]^2} = c_0^2 \left\{1 + \xi \tanh\left[\xi^{-1} \sum_j A_j e^{i2k_j \cdot r}\right]\right\}. \qquad (25)$$

Analysis of the optical properties of the resulting materials is in progress.

1.24 Understanding the Spectrum from Sonoluminescence

Sponsor

Defense Advanced Research Projects Agency
Contract N66001-96-C-8634

Project Staff

Professor Peter L. Hagelstein

When strong acoustic modulation is imposed on bubbles in a liquid, optical light emission can be observed. There has been much recent interest in the study of this process in the case of bubbles in water that contain a small amount of a noble gas. Hydrodynamic simulation of the collapse of these bubbles indicates that the peak temperature produced is perhaps high enough to produce a plasma. Spectral observations of the emission from bubbles that contain chromium carbonyl indicate that strong emission from atomic chromium occurs on several lines that are identified. From the relative emission strengths, it is possible to deduce the temperature, which in these experiments is close to 5000 K.

Bubble implosions in the case of N_2 bubbles in water that contain small additions of rare gases are known from observations to have the largest compression ratio. In such experiments, the maximum bubble size before implosion can be on the order of 50 microns, while the minimum observed radius during peak compression is on the order of 0.5 microns. While the volume change of the bubble in this case is six orders of magnitude, the corresponding density increase is far less since most of the nitrogen can pass through the bubble boundary. The rare gas admixture penetrates the boundary much less, and it is thought that the implosion of the residual rare gas component produces a plasma. Hydrodynamic simulations indicate that temperatures on the order of a few electron volts can be expected over a plasma size on the order of 100 Å, for a duration of about 50 ps. Experimental observations of the plasma emission are generally consistent with these computations.

There has been some confusion in the literature as to how the spectrum comes about. The emission is generally featureless (no spectral lines appear) and strongly weighted toward the blue. Such emission could be generated by a blackbody at several volts, although it has been unclear how a 100 Å sized plasma region could generate a blackbody spectrum over the entire observable optical spectral range.

To understand the spectrum, we have computed synthetic spectra that might be expected from a hot plasma including both Bremsstrahlung emission and skin depth effects. The approach that we have used is to compute the plasma absorption coefficient using

$$\frac{\kappa}{\omega} = \mathrm{Im}\left\{\sqrt{\left(\varepsilon - \frac{\sigma}{i\omega}\right)}\right\} \tag{26}$$

where σ is the plasma conductivity. The maximum optical depth of the plasma assuming a spherical shape is

$$\Delta\tau_{max} = 2\kappa R \tag{27}$$

which we find is always much less than unity. The differential power emitted by the plasma can then be estimated readily; we find

$$dP = \int dA \Delta\tau I_{BB}(\nu) d\nu \tag{28}$$

where we integrate over the area of the plasma and where $I_{BB}(\nu)$ is the blackbody intensity. The result can be expressed as

$$dP(\nu) = V\kappa(\nu)\frac{8\pi h\nu}{\lambda^2} n^2(\nu)\frac{1}{e^{h\nu/kT}-1} d\nu \tag{29}$$

where V is the plasma volume and where n is the index of refraction. Spectral predictions using this model can provide a good match to the experimental spectra, with the plasma volume V, the temperature T and the plasma density (which impacts κ) as parameters. Fitting the model to the spectrum then provides 2 constraints for the 3 variables. The plasma temperature is nearly fixed by the slope of the spectrum at the shortest observable wavelength (near 2000 Å). The product of the plasma volume and the square root of the density is fixed by the magnitude of the emission.

This result allows the experimental spectrum to be interpreted directly in terms of plasma parameters. Most importantly, it is possible to extract peak temperature estimates directly from the spectrum.

1.25 Off-Resonant Superradiant Coupling between Atoms and a Cavity

Sponsor

Defense Advanced Research Projects Agency
Contract N66001-96-C-8634

Project Staff

Professor Peter L. Hagelstein

The basic interaction between atoms and electromagnetic fields has been of interest to physicists since the dawn of quantum mechanics. One would imagine that this area has been studied for sufficiently long that no new physical effects would be expected. During the past year we have identified a new and interesting regime which appears to provide a wealth of unexpected new and interesting physics. This regime is perhaps best defined by what might be termed strong coupling physics. In this article, we would like to review the notion of strong coupling, and then examine some possible applications.

1.25.1 The Strong Coupling Regime

Almost all research in the area of electron-atom interactions has focused on weak coupling physics. Whether the coupling is weak or strong depends on how strong the interaction is relative to the energy splittings involved. For example, the interaction between a two-level representation of an atom and the electromagnetic field of a single cavity mode can be modeled in terms of the Hamiltonian

$$\hat{H} = \frac{1}{2}\Delta E\hat{\sigma}_z + V_0(\hat{\sigma}_+ + \hat{\sigma}_-)(\hat{a} + \hat{a}^\dagger) + \hbar\omega_0\hat{a}^\dagger\hat{a} \qquad (30)$$

The two-level system here is modeled using a pseudospin representation, and the interaction is presumed to be due to dipole coupling. We could transform this Hamiltonian into a representation based on the photon quantum number n and the pseudospin quantum number m. In this case the Hamiltonian normalized to the two-level energy becomes approximately

$$\hat{h} = M + \frac{n}{\eta} + g(\hat{\delta}_+^m + \hat{\delta}_-^m)(\hat{\delta}_+^n + \hat{\delta}_-^n) \qquad (31)$$

Here m is taken to be ±1/2 depending on whether the atom is excited or not, η is the ratio of the oscillator energy to the atom transition energy, and g is the coupling constant. This Hamiltonian is approximate in the sense that we have assumed that n is very large. The coupling constant g is essentially the ratio of the interaction energy $V\sqrt{n}$ and the transition energy ΔE. In typical atom-field interactions, the coupling constant is much less than unity, in which case perturbative methods can be used. When the electromagnetic field strength is very large, as in high intensity laser-induced multiphoton ionization, then it is possible for the associated coupling strength g to be of order unity.

We are interested here in a more subtle approach to the problem of arranging for strong coupling. If we place a large number of atoms in a cavity, and if the wavelength of the electromagnetic field is very great, then it is possible for the atoms to interact cooperatively with the electromagnetic field. The basic Hamiltonian in this case is

$$\hat{H} = \frac{1}{2}\Delta E\hat{\Sigma}_z + V_0(\hat{\Sigma}_+ + \hat{\Sigma}_-)(\hat{a} + \hat{a}^\dagger) + \hbar\omega_0\hat{a}^\dagger\hat{a} \qquad (32)$$

where the $\hat{\Sigma}$ operators are many-particle pseudospin operators. Expressing this Hamiltonian in terms of quantum numbers n and M (which assumes that we have Dicke states) leads now to

$$\hat{h} = M + \frac{n}{\eta} + g(\hat{\delta}_+^M + \hat{\delta}_-^M)(\hat{\delta}_+^n + \hat{\delta}_-^n) \qquad (33)$$

We have assumed here that both n and M are large. Here the coupling strength g is approximately

$$g \approx \frac{2V_0\sqrt{n}\sqrt{S^2 - M^2}}{\Delta E} \qquad (34)$$

This coupling is greater by a Dicke factor, which can be on the order of the number of atoms in the system. The associated physical statement is that many atoms interact cooperatively with the field of the cavity. It is possible to design such systems so that the coupling strength is much greater than 10^6. With such systems the strong coupling limit of atom-cavity interactions can be readily accessed. This interesting regime appears not to have received much attention previously.

1.25.2 Fluctuations in the Coupled System

If the coupling is strong, we might inquire as to what new physics shows up that was absent in the weak coupling model. The most obvious new physics concerns the entanglement of the atomic states with the photonic states. In the case that the atomic frequency is mismatched with the cavity, the states of

the coupled system are very nearly pure. For example, a state initially specified with a given M and n couples weakly with the nearest states with M ± 1 and n ± 1, and this coupling can be accurately deduced on the basis of perturbation theory. In the strong coupling limit, the system evolves to much more complicated states that include a wide range of different photon number n and atomic number M. Consequently, the fluctuations in M and in n can be enormous. For the simplified version of the model described above, it is possible to obtain exact analytic results for the fluctuations. We have found that

$$\left\langle (M - M_0)^2 \right\rangle = 2(g_+^2 + g_-^2) \tag{35}$$

$$\left\langle (n - n_0)^2 \right\rangle = 2(g_+^2 + g_-^2) \tag{36}$$

$$\left\langle (M - M_0)(n - n_0) \right\rangle = 2(g_+^2 - g_-^2) \tag{37}$$

$$\text{where} \quad g_\pm = \frac{g}{1 \pm \frac{1}{\eta}} \tag{38}$$

That strong coupling effects can induce large fluctuations in M and n might have been expected, and probably does not constitute an exciting new result. But within this result in fact lies a potentially explosive new effect, which is perhaps unexpected and may be of considerable interest. If there exists a large spread in both the photon number and in the atomic number, then the distribution of states may include some states which are nearly degenerate with the initial state. For example, suppose that $\eta = 3$ (so that the cavity is tuned just so that 3 photons make up the energy needed for one atomic transition). In this case, the state $|M,n\rangle$ is coupled indirectly with the degenerate states $|M+1,n-3\rangle$ and $|M-1,n+3\rangle$. This raises the possibility that linear coupling, enhanced by a strong coupling effect, would lead to consequences that would be only expected in a nonlinear system. One would never expect to see a high order conversion effect in a linear system.

Nevertheless, such a conversion can be shown to occur.[126] We illustrate in Figure 40 an eigenfunction in the case of $\eta = 3 - 1.2 \times 10^{-7}$. In this case, the probability amplitude is localized, corresponding to the fluctuation estimates given above. In Figure 41, we show an eigenfunction corresponding to the case of $\eta = 3 + 1.2 \times 10^{-7}$, which shows considerable exchange between photons and atoms. What happens in this case is that a small offset in η produces a tuning of the system, as photons of the coupled system are exchanged for atomic excitation of the coupled system. The coupling produces a small self-energy shift which must be included in the resonance condition. When all of the localized states are thereby made degenerate, a weak coupling is present between them when produces a large level of fluctuations.

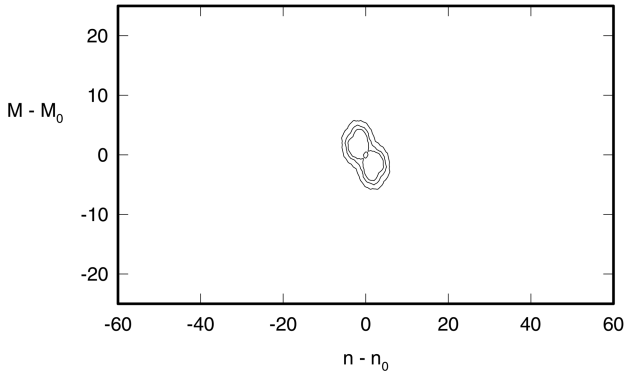

Figure 40. Localized eigenfunction corresponding to $n_0 = 10^{20}$, $S_0 = 10^4$, $M_0 = 10^3$ and $\eta = 3 - 1.2 \times 10^{-7}$. This state is very nearly the same as the analytic solution which corresponds to the large M and large n limit of the theory mentioned in the text.

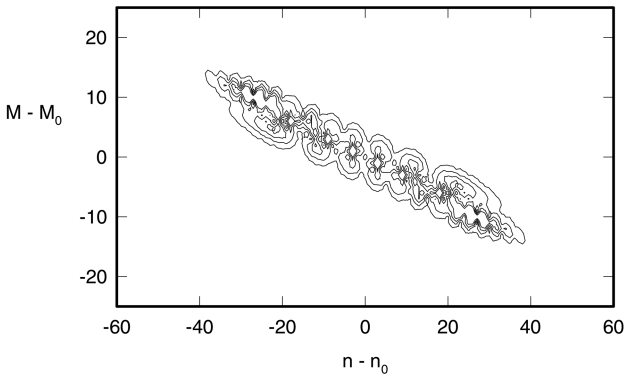

Figure 41. Delocalized eigenfunction corresponding to $n_0 = 10^{20}$, $S_0 = 10^4$, $M_0 = 10^3$ and $\eta = 3 + 1.2 \times 10^{-7}$. This state shows significant energy exchange between the two-level systems and the oscillator. Three oscillator quanta of the coupled system are exchanged for each two-level excitation.

126 P.L. Hagelstein, "Anomalous Energy Exchange Between Two-level Systems and an Oscillator," submitted to *Phys. Rev. Lett.*

1.26 Publications

1.26.1 Journal Articles

Fini, J.M., P.L. Hagelstein, and H.A. Haus. "Agreement of Stochastic Soliton Formalism with Second-quantized and Configuration-space Models." *Phys. Rev. A* 57: 4842 (1998).

Fini, J.M., P.L. Hagelstein, and H.A. Haus. "A Configuration Space Model for Soliton Propagation Including Loss and Gain." Submitted to *Phys. Rev. A.*

Fini, J.M., P.L. Hagelstein, and H.A. Haus. "Nonperturbative Calculation of Soliton Variables." Submitted to *Phys. Rev. A* (1998).

Hagelstein, P.L. "Anomalous Energy Exchange Between Two-level Systems and an Oscillator." Submitted to *Phys. Rev. Lett.*

Hagelstein, P.L. "Atom-atom Correlation in the Presence of Strong Terahertz Phonon Excitation." *Phil. Mag. B* 79:149 (1998).

Hagelstein, P.L. "Optical Excitation by Microwaves." Submitted to *Phys. Rev. A*.

Hagelstein, P.L. "Possibility of Measuring Isotope Shifts by Microwave-induced Transfer of Optical Excitation." Submitted to *Z. Phys. D.*

Hagelstein, P.L., D.R. Denison. "Nearly Isotropic Photonic Band Gap Structures in 2D." *Opt. Lett.* Forthcoming.

1.26.2 Meeting Papers

Hagelstein, P.L. "Anomalous Energy Transfer." Paper published in the *Proceedings of the International Cold Fusion Forum (ICCF-7)*, Vancouver, Canada, March 1998.

Hagelstein, P.L. "Possibility of Off-Resonant Superradiant Effects." Paper presented at the International Conference on X-ray Lasers and Applications, Kyoto, Japan, September 1998.